Improving the Seismic Performance of Steel Moment Resisting Frames through Advanced Approaches

by

Christian Anthony Flores Carreras

A dissertation submitted in partial fulfillment
of the requirements for the degree of
Doctor of Philosophy
(Civil Engineering)
in the University of Michigan
2023

Doctoral Committee:

Professor Jason P. McCormick, Chair
Professor Sherif El-Tawil
Assistant Professor Evgueni Filipov
Professor Jwo Pan

Christian A. Flores Carreras

florcarr@umich.edu

ORCID iD: 0000-0002-3730-306X

DEDICATION

To my parents, Grace and Victor, my sister, Stephanie, my grandparents, Margarita, Antonio, and Sara, my friends, and everyone else that supported me and helped me to get to this point… Thank You.

ACKNOWLEDGEMENTS

First I would like to express my sincere gratitude to my advisor, Dr. Jason McCormick. His expert guidance, invaluable support and sympathetic understanding through the years truly encapsulates what it means to be an adviser. I have grown immensely as a professional through my doctoral studies and I owe much of that to him. I would also like to thank Professor El-Tawil, Professor Filipov and Professor Pan for agreeing to serve on my dissertation committee. I have had the opportunity of taking classes that they have taught, all of which greatly increased my understanding of engineering and aided my research.

I would also like to thank the excellent lab technicians I had the pleasure to work with, without which the research presented in this dissertation would have not been completed. Justin Roelofs, Steve Donajkowski, Bob Spence, Ethan Kennedy, and Jan Pantolin: thank you for all your help and support with designing and running my experimental tests.

Finally, I would like to thank everyone that supported me through this entire endeavor. Andrea Ventola, Carlos Enrique Soler Ayoroa, Cassi Champagne, Malcolm Ammons, Manisha Patel, and many other friends and family members: thanks to all of your love and tireless support, even in the toughest of times, I was always able to continue moving forward. I have learned much from all of you, and it is a privilege to have you in my life.

TABLE OF CONTENTS

LIST OF TABLES

LIST OF FIGURES

ABSTRACT

After the 1994 Northridge earthquake in the US caused significant structural damage to steel moment resisting frames, revised seismic provisions were developed to address the vulnerabilities observed in the affected structures. These new design requirements led engineers in the US to favor the use of deep, slender wide flange columns over stockier wide flange sections. However, these deeper and more slender wide flange sections have been shown to be more prone to local and global instabilities due to their larger local slenderness ratios and smaller radius of gyration about the weak axis. Recent investigations into the behavior of deep, slender wide flange column sections have shown that some column sections exhibit significantly less ductility than is expected due to a previously unrecognized interaction between the local and global instabilities, making them more prone to collapse.

While more research is needed to better understand this phenomenon, it is also worth exploring alternatives to improving the seismic performance of moment resisting frames outside of utilizing wide flange sections. A potential alternative is to take advantage of the beneficial properties of hollow structural sections (HSS). These sections offer excellent torsion resistance, good bending strength, and the option to fill their voids with different materials to enhance their performance. Despite these benefits, HSS members are not commonly used in seismic steel moment frames due to stringent local slenderness requirements and a lack of a non-proprietary prequalified seismic moment connection. With these ideas and shortcomings in mind, this research seeks to improve the seismic performance of steel moment resisting frames through the assessment of deep, slender wide flange columns and advanced alternatives utilizing HSS.

To this end, a finite element and experimental investigation of deep, slender wide flange column subassemblies is undertaken to study the behavior of these sections under combined axial and lateral load while in the presence of framing elements such as beams and connections. The results from these tests show how the local and global instabilities can interact with each other to accelerate the capacity degradation in a column section and cause it to not meet the expected ductility requirements. These findings highlight the need to consider the interaction between local and global failure modes in the design process as they are currently checked separately and show similar behavior between previous member level studies and the subassembly specimens.

Following this study, an experimental and complimentary computational investigation on empty and foam-filled HSS beams is undertaken to explore the benefits of utilizing a polyurethane foam as a fill material. The polyurethane foam-fill provides additional energy dissipation capacity while improving the stability of the HSS walls, mitigating the effects of local buckling, and increasing the cyclic performance of HSS beam members. The findings of this study show that incorporating a polyurethane foam as fill material can alleviate the stringent local slenderness requirements and allow more HSS sizes to meet the moderate and high ductility performance criteria.

Finally, a computational investigation of an innovative tube-based collar connection is undertaken to enhance the feasibility of such a connection through economy and efficiency improvements. While the collar connection has previously been experimentally shown to provide adequate ductility, the findings of this study indicate further optimizations can be made to significantly reduce the amount of field welding that is necessary, saving on cost and construction time.

CHAPTER I

Introduction

Background and Motivation

The 1994 Northridge earthquake in the US caused significant structural damage to steel moment resisting frames, revealing flaws in their design and construction. During the Northridge earthquake many buildings with commonly used welded flange-bolted web beam-to-column moment connections exhibited brittle fracture, typically initiating near the weld connecting the bottom beam flange to the column flange (FEMA 2000). At the time, these connections utilized a complete joint penetration (CJP) groove weld to make this connection, while the beam web was connected to the column flange using a bolted shear plate. The occurrence of brittle fracture was unexpected and led to the formation of the SAC Steel Project, which aimed to address concerns of structural integrity and performance in these structural systems (SAC 2000). The investigations that followed identified multiple reasons why brittle fracture occurred. Key factors included: a flawed design assumption that all shear force was transferred through the bolted web connection, failing to recognize that a significant amount of shear was also transferred through the beam flanges (an issue that was only made worse due to a weak panel zone design approach); not recognizing the effect of the actual steel yield and tensile strength, which was higher than the nominal values due to changes in steel production in the 1980s, on the cyclic performance of connections; and overlooking the importance of weld details, processes, quality, and inspection (Uang and Bruneau 2018).

Following the SAC Steel Project, revised seismic provisions emerged that included more stringent drift limits, strong column-weak beam requirements, and a balanced panel zone design approach. The research also led to the creation of the first edition of the Seismic Supplement by the American Welding Society (AWS) and a new grade of steel (ASTM A992) for wide flange sections that established an upper bound for the yield-to-tensile strength ratio of 0.85 (Uang and Bruneau 2018). While these revisions addressed many of the issues that had been uncovered, they also made it more difficult to satisfy the new seismic design requirements. As a result, these changes pushed engineers in the US towards using deeper and more slender wide flange column sections to achieve more economic designs. While these sections benefit from having a larger moment of inertia than stockier sections (providing higher stiffness, and therefore lower drifts than a stockier section with comparable surface area), their local slenderness ratios are larger and their radius of gyration about the weak axis is smaller, making the section more susceptible to local buckling failure modes and out-of-plane global buckling failure modes under compression.

After the 1994 Northridge earthquake the cyclic behavior of wide flange beams was intensely studied due to concerns associated with beam-to-column moment connections and the pervasive use of these sections in moment frame systems. Meanwhile, column behavior did not receive a similar amount of attention, even as the use of deep columns rose in popularity. Chi and Uang (2002) first raised concerns about the cyclic performance of deep columns. They tested three reduced beam section (RBS) connection subassemblies and observed that all of them exhibited twisting and out-of-plane bending of the column, even with no axial load being applied (Chi and Uang 2002). This behavior was due to buckling of the beam which introduced torsion and out-of-plane bending into the column, while the torsional properties of the deep, slender wide flange column also resulted in large warping stresses. More recent member-level investigations, both

experimental and computational, into the performance of deep, slender wide flange columns have continued to suggest that some deep columns do not deliver the expected plastic rotation capacity while subjected to high axial loads and bending moments, possibly due to a previously unrecognized interaction between local and global failure modes (Zargar et al. 2014, Uang et al. 2015, Elkady and Lignos 2015, Fogarty and El-Tawil 2016, Elkady and Lignos 2016). Computational investigations at the system-level also have obtained similar results. A study by Wu et al. (2018a) shows that the current highly ductile limits established in the AISC Seismic Provisions (2016a) are unable to guarantee deep columns can reach the expected 4% drift without significant loss in strength or failure. A second study by Wu et al. (2018b) confirms the importance of local and global slenderness ratios on the cyclic performance of deep columns and shows these parameters can also affect the collapse behavior of special moment frames (SMFs).

While these results raise some concerns, further studies are needed to better understand this phenomenon. Specifically, experimental testing is needed at the subassembly-level to see how the deep, slender column failure modes interact and are influenced by other building elements such as beams and connections. Beyond conducting these necessary investigations, there is also interest in searching for solutions to the aforementioned issues outside of conventional building practices. One opportunity is to more frequently incorporate hollow structural sections (HSS) as major structural components of steel moment frames, both as beams and columns, to take advantage of their beneficial properties such as their excellent torsional resistance, good bending and compression strength, low strength-to-weight ratio, and pleasing aesthetics. While HSS, both empty and concrete-filled, have been commonly used as column and beam-column members in seismic frame systems (Hajjar 2000), they are typically paired with wide flange beam members. One reason for the lack of an HSS-based seismic moment frame is the absence of non-

proprietary, pre-qualified seismic moment connections between HSS columns and HSS beam members (AISC 2016b). This lack of pre-qualified HSS-to-HSS seismic moment connections pushes structural engineers away from using HSS beams in their designs as they would need to design their own connection and conduct rigorous testing to ensure it meets current seismic design requirements (AISC 2016a).

In an effort to address this shortcoming, Fadden et al. (2015) tested through plate and external diaphragm plate reinforced HSS-to-HSS moment connections, both of which exhibited stable hysteretic behavior up to 7% story drift. Although the performance of these connections is more than adequate, both connections require large amounts of field welding which increases costs and makes it more difficult to ensure construction quality. Other investigations into an innovative collar connection design have shown promise with regards to ease of construction and limiting the amount of field welding, while still providing a stable hysteretic behavior up to 6% drift (Wei 2017). An additional barrier to the use of HSS members is the fact that it was not until recently (2012) that HSS beams were shown to perform adequately in seismic scenarios. Fadden and McCormick (2012, 2014a) conducted full-scale experimental and computational studies and demonstrated HSS beams are viable for cyclic bending applications, provided that the section's local slenderness ratios are adequately selected to limit local buckling at small drift levels. These studies suggest conservative b/t and h/t limits of 12.1 and 28.4, respectively, for an HSS beam to maintain 80% of its maximum moment capacity at 4% drift. However, stringent local slenderness requirements can limit the number of available sections that meet seismic design criteria, further hindering the use of HSS in seismic moment frames.

A potential solution to this issue comes in the form of incorporating fill material in the void of HSS to improve the performance of HSS beams. This fill material has traditionally been

concrete or cementitious grout. Previous research by Prion and Boehme (1994) showed that concrete-filled circular HSS under pure bending fail in a very ductile manner and exhibit significant amounts of energy dissipation. Further investigations by Lu and Kennedy (1994) found that the ultimate flexural strength of the HSS can increase by 10 to 30% when filled with concrete. While these studies suggest that concrete-fill can improve the performance of HSS beams, the use of concrete as fill material has some potential drawbacks, including an increase in flexural strength and stiffness that needs to be considered during design to ensure connecting elements can withstand the higher loads. Additionally, the concrete-fill will increase the seismic mass of the structure, resulting in an overall increase in the expected loads that the structure experiences during a seismic event. However, materials from other industries provide potential fill alternatives that can improve the performance of these sections with decreased drawbacks. For example, in the automotive industry Zhou et al. (2016) investigated the influence of a lightweight polyurethane foam-fill in AZ31B magnesium beams and DC04 steel beams. The results suggest that the foam-fill stabilizes the deformation of the tube walls, which in turn improves the beam's energy absorption capacity significantly. This stabilization of the tube walls prevents or delays the onset of local buckling, mitigating its negative effects, and allowing the beam to retain more of its strength.

Motivated by the issues detailed in this section, the main goal of this dissertation is to improve the seismic performance of steel moment frames through the assessment of deep, slender wide flange columns and their alternatives, focusing on the potential benefits of HSS members and non-traditional materials. To achieve this goal, the cyclic behavior of deep, slender wide flange columns and the influence of other structural components is evaluated under reversed cyclic loading conditions similar to those experienced during an earthquake. Similar

tests for a subassembly that features an HSS column are conducted using a finite element (FE) model to determine if this type of section experiences similar performance issues as deep, slender wide flange sections. Furthermore, the potential performance improvements of incorporating a polyurethane foam-fill in HSS beam members will be assessed through member-level studies to determine if less stringent local slenderness requirements are feasible. Finally, computational methods will be employed to further study and optimize the collar connection concept to work toward a non-proprietary prequalified HSS-to-HSS seismic moment connection.

Objectives and Scope

To achieve the goals of this dissertation, the following objectives with their corresponding tasks are established:

1) Assess the seismic performance of deep, slender wide flange column subassemblies under high axial and lateral loads
    a. Conduct experimental testing of half-scale cruciform subassemblies (Fig. I.1) that feature a wide flange column subjected to large axial loads and different lateral loading scenarios (symmetric cyclic and cyclic ratcheting). Seismic performance will be assessed through metrics such as maximum moment capacity, moment capacity degradation, collapse drift level, energy dissipation capacity, column axial shortening, and ability to meet current seismic ductility requirements.
    b. Understand the influence of other structural components (beams and connections) on the cyclic behavior of deep, slender wide flange columns. Along with the experimental test results, FE models will be used to further develop design recommendations with regards to slenderness limits for deep column sections in seismic applications.

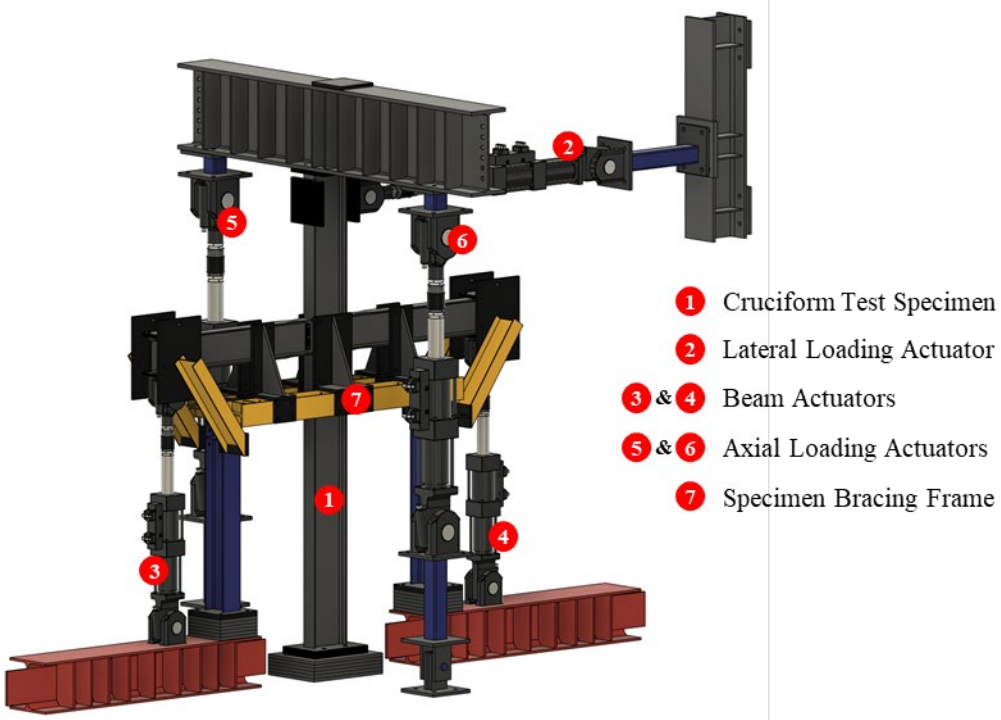

Figure I.1. Test setup for cruciform column specimen.

2) Explore viable alternatives to wide flange sections in steel moment resisting frames

   a. Conduct a computational study of a cruciform subassembly that features a comparable HSS column to investigate if the HSS section undergoes similar combined local and global buckling interactions as seen in deep, slender wide flange sections. Similar performance metrics to the wide flange column subassembly study are used to allow for comparison with the wide flange subassembly tests. Results from these tests will show whether HSS columns have inherent performance or safety benefits over deep, slender wide flange sections in seismic applications.

   b. Conduct full-scale experimental tests on pairs of empty and polyurethane foam filled HSS beams subjected to cyclic bending loads (Fig. I.2a). Performance improvements will be assessed through metrics such as maximum moment capacity, moment

capacity degradation, energy dissipation capacity, and ability to meet IMF and SMF ductility criteria.

c. Develop an FE model of the empty and foam filled beams informed by data from the experimental testing (Fig. I.2b). This model will be used to conduct a large-scale parametric study to look at the influence of the foam fill across a wide variety of local slenderness ratios and section sizes.

d. Develop local slenderness requirements for polyurethane foam-filled HSS beam sections to help facilitate and promote their use in building design.

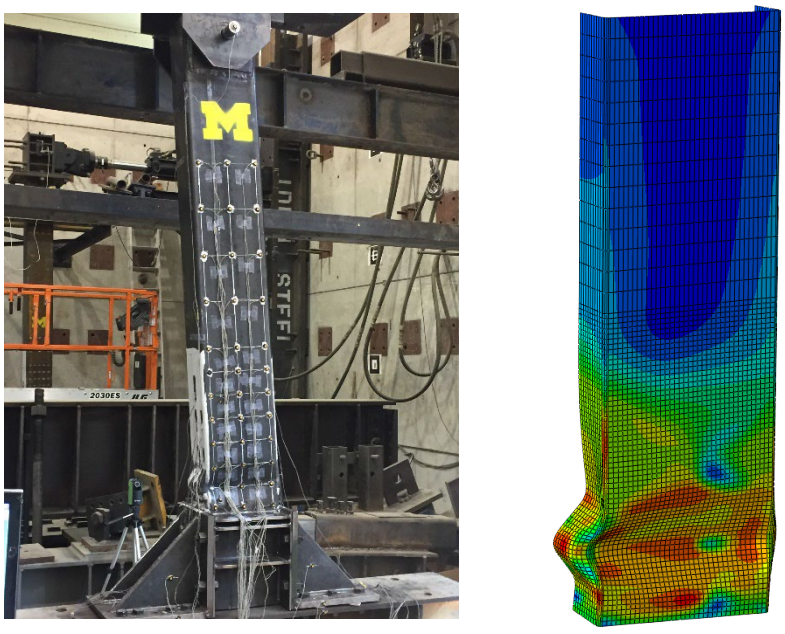

(a) (b)

Figure I.2. (a) Experimental test setup for empty and foam-filled HSS beams. (b) FE model developed with data obtained from experimental results.

3) Address the lack of a non-proprietary, pre-qualified HSS-to-HSS seismic moment connections

a. Optimize a collar connection prototype to propose as an HSS column-to-HSS beam seismic moment connection (Fig. I.3). An FE model of the connection is used to

perform a parametric study that varies metrics such as beam endplate thickness, collar thickness, and weld placement and length. The goal is to achieve a balanced and efficient connection design where select components contribute adequately to the overall plastic rotation of the system.

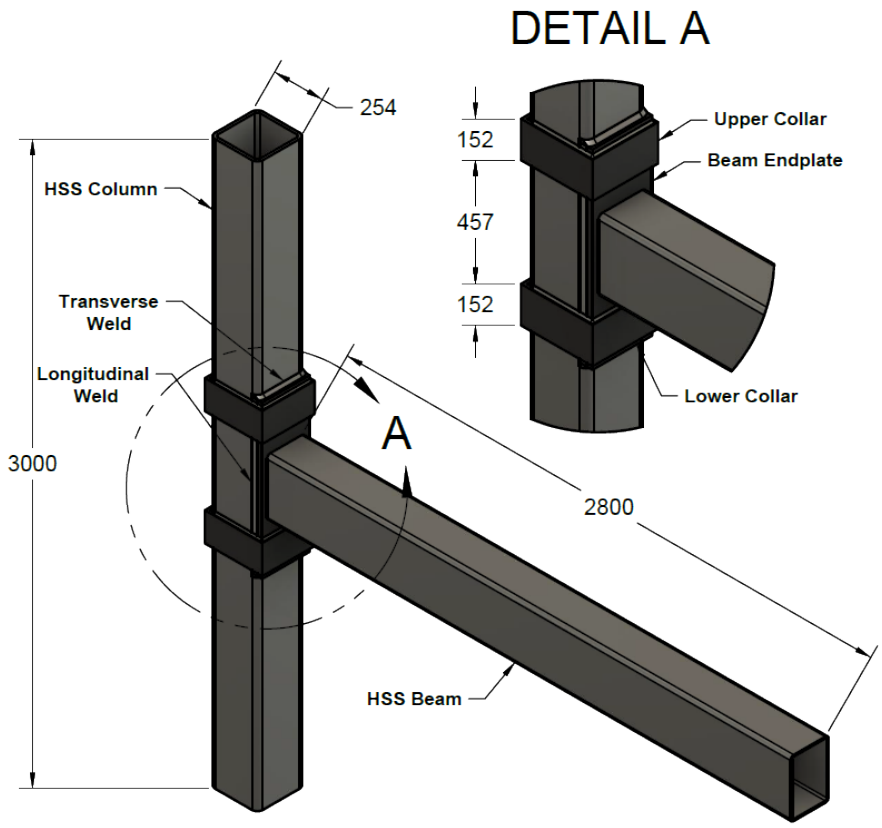

Figure I.3. Tube-based collar connection concept. (Units: mm)

Dissertation Chapters

Chapter 1: Introduction – General introduction presenting the overall motivation and problem that is addressed in this research. The main goal of the dissertation is established, and the path taken to achieve this goal is outlined with relevant research objectives.

Chapter 2: Investigation of Deep, Slender Wide Flange Column Subassemblies – This chapter investigates the seismic behavior of deep, slender columns at a subassembly level. A

preliminary FE analysis of full-scale subassemblies is conducted to explore the performance differences between deep, slender wide flange column sections and a comparable HSS column section. The results from this study were published in Flores Carreras et al. (2020). This computational study also served to inform the development of the experimental test setup. The experimental program includes three half-scale wide flange cruciform specimens that are tested under two lateral loading protocols. The test results are analyzed to determine whether the presence of other structural components is beneficial or detrimental to the cyclic behavior of the column.

Chapter 3: Improving the Cyclic Performance of HSS Beams by Incorporating a Lightweight Foam-Fill – This chapter explores the performance benefits of incorporating a polyurethane foam fill in HSS beams. Seven pairs of empty and foam filled beam specimens are experimentally tested under fully symmetric cyclic loading to compare their behavior. The selected sections span a variety of local slenderness ratios and ductility ratings. The foam's capability to mitigate the effects of local buckling is examined with regards to changes in the beam's moment capacity degradation with continued cycling, rotation level at fracture, ability to meet the current IMF and SMF requirements and energy dissipation capacity. Partial results from some of the tests were published in Flores Carreras et al. (2018).

Chapter 4: A Parametric Study of Urethane Foam-Filled HSS Beams – This chapter expands on the work completed in Chapter 3 by using the experimental results to inform the development of an FE model of the empty and polyurethane foam-filled HSS beams. This model is used to conduct a much larger study across fifty pairs of HSS beams, allowing for a more complete understanding of the effects of the foam-fill across a wide range of local slenderness ratios and

section sizes. The data gathered in this chapter is used to determine local slenderness limits (*b/t* and *h/t*) for both empty and urethane foam-filled HSS beams.

Chapter 5: Finite Element Analysis of HSS-Based Seismic Collar Connections under Cyclic Loads – This chapter complements previous experimental work on a collar connection concept through FE simulations. Results from the experimental testing are used to develop an FE model of the connection which is used in an optimization-focused parametric study to better understand and improve the behavior of the connection.

Chapter 6: Summary and Conclusions – This concluding chapter of the dissertation summarizes the research and highlights the key contributions and findings. It also outlines relevant areas where more research is needed to fill gaps of knowledge necessary to be able to implement the findings in practice.

CHAPTER II

Investigation of Deep, Slender Wide Flange Column Subassemblies

Introduction

The 1994 Northridge earthquake exposed vulnerabilities in the design and construction of steel moment resisting frames. Specifically, many steel buildings suffered damage due to improperly detailed welded flange-bolted web beam-to-column moment connections that led to fracture near the complete joint penetration welds between the bottom beam flange and the column flange (FEMA 2000). As a direct response to uncovering these issues, the SAC Steel Project was created to investigate and address the performance concerns of steel moment resisting frames (SAC 2000). The seismic provision changes that originated from this investigation (more stringent drift limits, strong column-weak beam criteria, balanced panel zone design) addressed a lot of the issues that were discovered, but also made satisfying the design requirements more difficult, pushing engineers towards the use of deeper, more slender wide flange column sections. Deep, slender wide flange sections typically have depth greater than 610 mm (24 in.) as compared to the previously used more stocky wide flange sections that had depth around 356 mm (14 in.) with the flanges and web having similar lengths. Although these deep, slender wide flange sections have the benefit of a larger moment of inertia than stockier sections, they are more prone to local buckling and out-of-plane global buckling failure modes due to larger local slenderness ratios and a smaller radius of gyration about their weak axis.

Recent member-level studies of deep, slender wide flange columns have revealed unexpected interactions between local and global instabilities that result in some deep, slender wide flange columns failing to deliver adequate plastic rotation capacity when subjected to large axial loads and bending moments (Zargar et al. 2014, Uang et al. 2015, Elkady and Lignos 2015, Fogarty and El-Tawil 2016, Elkady and Lignos 2016). Other computational investigations at a system-level have shown similar results. Wu et al. (2018a) showed that the current high ductility limits specified by the AISC Seismic Provisions (2016a) are unconservative and do not guarantee that deep, slender wide flange columns in special moment frames (SMFs) can reach the expected 4% drift without a significant loss in strength or failure. Further, Wu et al. (2018b) confirmed the importance of considering both the local and global slenderness ratios of deep, slender wide flange columns as both can affect the collapse capacity of SMFs. While the results pertaining to the performance of deep, slender wide flange columns raise concerns, further investigations by Elkady and Lignos (2018) and El Jisr et al. (2020) have highlighted the importance of realistic boundary conditions and framing action on the performance of these column sections, as neglecting these parameters can result in unrealistically high strength demands.

In an effort to investigate alternatives to the use of deep, slender wide flange columns, Sediek et al. (2020) also conducted a computational study on the behavior of HSS columns as opposed to using wide flange sections. This member-level study suggests that HSS columns can be a more efficient alternative to wide flange columns in low to midrise SMFs due to their higher axial strength when considering column weights of 150 kg/m (100 lb./ft.) or less.

These previous studies show the need for further investigation into the behavior of deep, slender wide flange column sections in the presence of other framing elements such as beams and connections. To this end, an experimental investigation is conducted using three half-scale

cruciform subassemblies that feature an interior deep, slender wide flange column connected to two beams through a reduced beam section beam-to-column seismic moment connection. Preliminary finite element (FE) simulations also are conducted on four full-scale cruciform subassemblies, one of which features an HSS column. The subassemblies are tested with varying axial load ratios and two lateral loading protocols. The performance metrics used to assess the behavior of the cruciform subassemblies include moment capacity degradation with continued cycling, column axial shortening, local and global instabilities, and ability to meet SMF ductility requirements.

Preliminary Finite Element Study

Subassembly selection methodology

FE simulations of the subassemblies were conducted prior to the experimental testing to inform the development of the experimental test setup and explore behavioral differences between subassemblies that feature either a wide flange column or an HSS column. The simulation results provide insight into expected behavior, loads, and deformation levels which were all considered for the design of the experimental setup. The model SMFs were obtained from a National Institute of Standards and Technology (NIST) report by Kircher et al. (2010). All of the steel moment resisting frames in this report were designed following the AISC Seismic Provisions (2005) and the ASCE-7 seismic design requirements (2005). While updates have since been made to these design provisions, the design standards that pertain to this study have not changed since the NIST report was published.

The building plan of the SMF prototypes used to develop the modeled subassemblies considered in this study is presented in Fig. II.1b (Kircher et al. 2010). The full-scale FE model of the subassembly represents an interior column connected to two wide flange beam members to

form a cruciform (Fig. II.1a). The FE model is one and a half stories tall and half a bay width wide to each side of the column. Three different subassembly configurations are selected to represent a variety of wide flange column sizes ranging from stocky to deep, slender sections. General information on the selected subassemblies is presented in Table II.1. An additional subassembly is included for comparison that incorporates an HSS column that is comparable to the W610×153 (W24×103) column in subassembly SA3. The selection of this HSS column was determined through an iterative process that considered a similar building frame to that from which subassembly SA3, which is the subassembly that is later used for the experimental tests, was extracted.

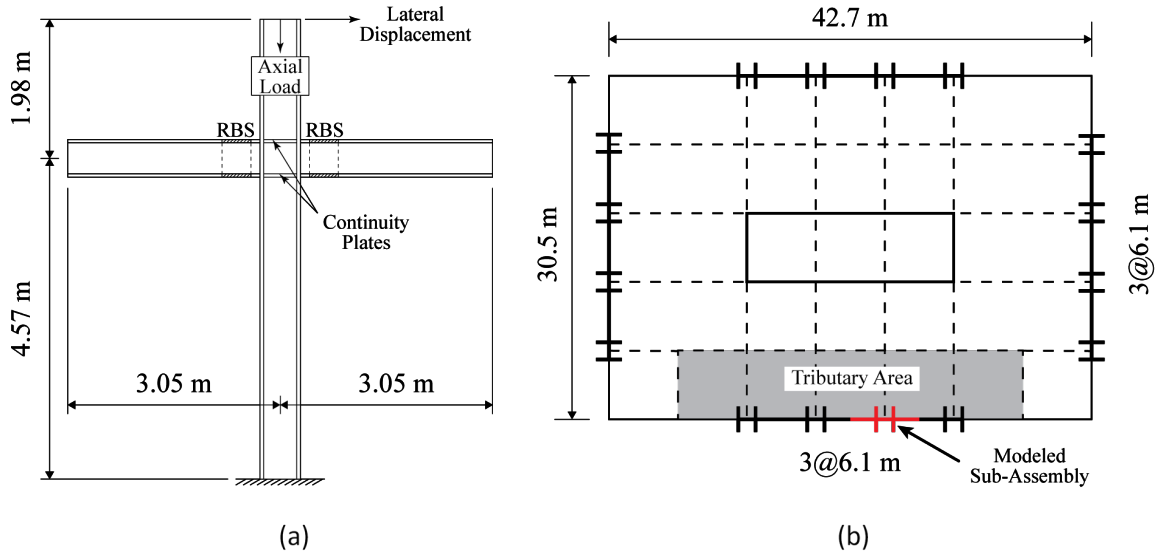

Figure II.1. (a) Schematic of the wide flange column subassembly and (b) typical building plan of the steel moment resisting frames.

Table II.1. List of subassemblies included in the FE simulations.

Subassembly ID	Column Section (mm, mm×kg/m)	Beam Section (mm×kg/m)	Axial Load Range	Building Stories
SA1	HSS508×203.2×15.9 [HSS 20×8×5/8]*	W530×85 [W21×57]*	(0.2 - 0.4) P_y	4
SA2	W360×110 [W14×74]*	W410×85 [W16×57]*		4
SA3	W610×153 [W24×103]*	W530×109 [W21×73]*		4
SA4	W920×449 [W36×302]*	W760×161 [W30×108]*		20

* Section in US Customary Units (in×lb/ft)

Development of the FE model

The finite element model represents a full-scale cruciform subassembly of a column with a beam connected to each flange (Fig. II.2). The dimensions of the subassembly are selected so that the ends of the beams and column are at their respective inflection points during the lateral movement of the entire building frame. The boundary conditions on the model include a fixed column base, appropriate lateral bracing along the beam flanges and beam-to-column connection, and a roller support at the beam ends that allows in-plane movement and rotation, but prevents the same in the out-of-plane direction. Additionally, the vertical displacement at the beam ends is tied with an equation constraint to the vertical displacement at the top of the column. This constraint ensures that the beam ends displace downward with the same magnitude as the column when column shortening occurs due to local buckling at the column base. By applying this additional constraint, the finite element model is accounting for the fact that axial shortening, which has been observed in previous member level tests of columns under large axial loads and bending moments (Elkady and Lignos 2018, Uang et al. 2015), will occur in all of the columns of a given story.

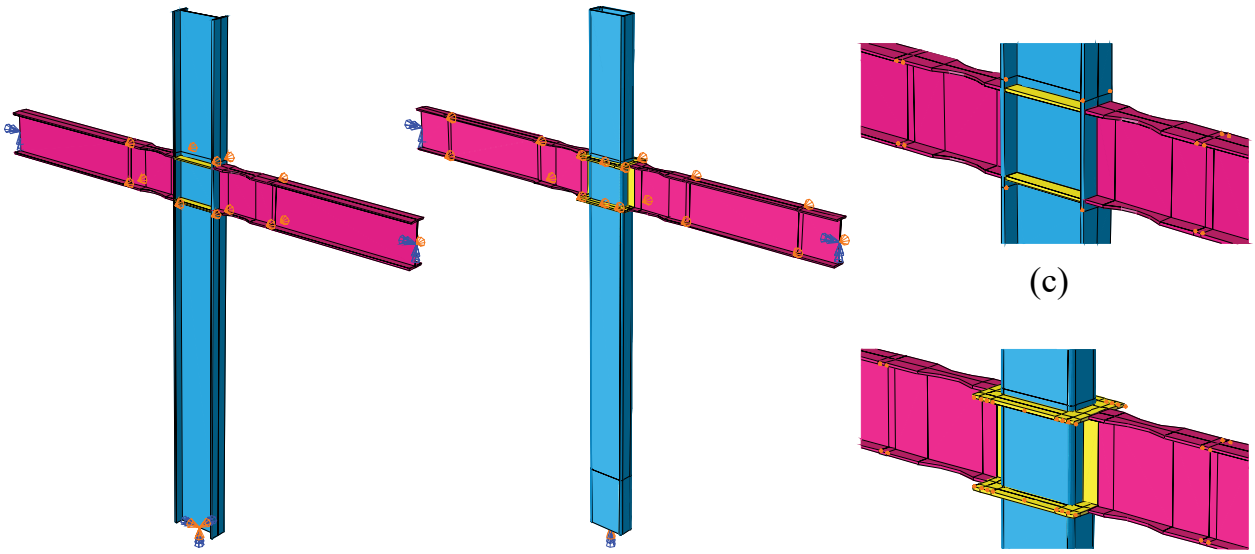

Figure II.2. Finite element models of the (a and c) wide flange column and (b and d) HSS column subassemblies.

The wide flange subassemblies feature a prequalified reduced beam section (RBS) seismic moment connection that is commonly used in SMFs (AISC 2016b). With regards to the HSS column subassembly, there are currently no non-proprietary prequalified seismic moment connections available for use. For this reason, the HSS column subassembly is designed using the connection presented in Vulcu et al. (2017a). A schematic of the RBS diaphragm moment connection is presented in Fig. II.3. The connection was originally developed for concrete-filled HSS columns connected to wide flange beams and was experimentally shown to perform adequately under cyclic lateral loading, exhibiting a rotation capacity of over 4% drift. The connection uses external diaphragm plates and vertical column stiffeners to connect the beams to the column thereby transferring the loads directly to the stiffer sidewalls of the HSS column and bypassing the flexible HSS face. While these experiments were conducted with a concrete-filled HSS column, a subsequent computational study showed the RBS diaphragm connection performed similarly in the absence of the concrete-fill (Vulcu et al. 2017b).

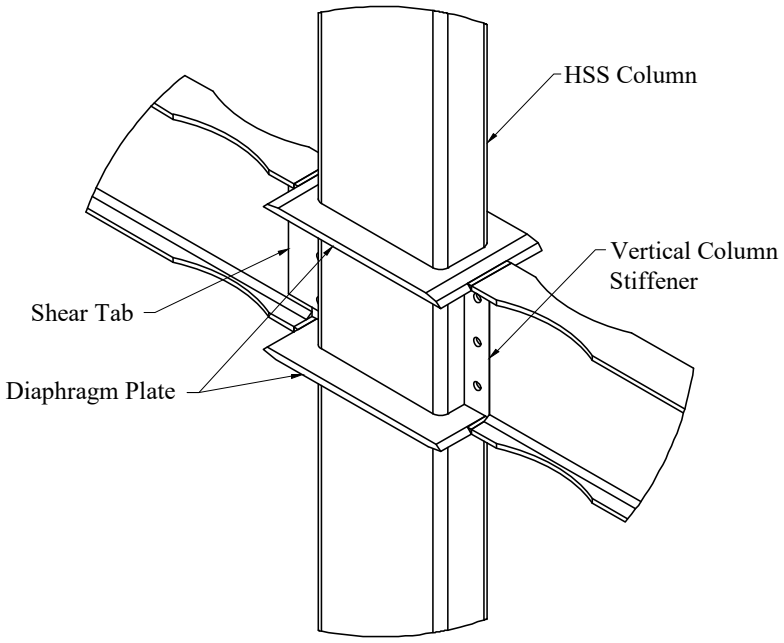

Figure II.3. Schematic of the HSS column-to-wide flange beam RBS diaphragm moment connection.

Details of the finite element model

The different steel grades that are used in the subassemblies are ASTM A992 (F_y = 345 MPa (50 ksi)), ASTM A500 Gr. B (F_y = 317 MPa (46 ksi)), and ASTM A572 Gr. 50 (F_y = 345 MPa (50 ksi)) for the wide flange members, HSS column, and steel plates making up the RBS diaphragm moment connection, respectively. The ASTM A992 material model is a nonlinear kinematic hardening model that includes two back stress terms. The calibration of this model is accomplished by developing a true stress-true strain curve and comparing it to the material model proposed by Arasaratnam et al. (2011). More details on the calibration and validation of this material model are presented in Wu et al. (2018a). The ASTM A500 material model utilizes a combined kinematic and isotropic hardening law. Different hardening parameters for this material are also specified for the flats and corners of the HSS to take into account the effects of cold working. Cold working results in the corners of the HSS having a higher yield strength, but

lower ductility when compared to the flats. A more in-depth discussion of this topic is presented in Fadden and McCormick (2014a). The kinematic and isotropic material parameters are calibrated against experimental data from tensile coupon specimens and the moment-rotation curves from cantilever HSS beam members undergoing cyclic rotations. A more detailed explanation of the calibration process is presented in Chapter IV. Finally, the material model for ASTM A572 Gr. 50 steel is an isotropic hardening model based on experimental tension coupon test data.

The subassemblies are constructed in Abaqus (Simulia 2017) using S4R elements (4-node doubly curved shell, reduced integration, hourglass control) with an element size of 19.1 mm (0.75 in.) along the column, connection, and RBS regions of the beam. An element size of 38.1 mm (1.5 in.) is used everywhere else. Initial deformations are applied to the finite element model of the column in the column base region in order to accurately capture local buckling during the simulation. The shape of the initial deformations is obtained through a column buckling analysis. For the case of the HSS column, the magnitude of the imperfection is scaled to half of the maximum allowable imperfection prescribed by the ASTM standard for cold-formed tubular shapes (ASTM 2018). For the case of the wide flange column, the magnitude is scaled to the smaller value between $b_f/250$ and $h_w/250$. Following the SMF requirements in the AISC Seismic Provisions (2016a), lateral bracing of the subassembly is provided by constraining the out-of-plane displacement at the beam-to-column connection region, near the RBS protected zone, and at appropriate locations along the beams. A self-contact interaction is applied at the column base region of the subassemblies to take into account possible squashing at large column rotations. Fracture is not considered in the finite element model.

Loading protocol

Various levels of constant column axial load are used to study the effect of the axial load on the overall strength and seismic performance of the columns in the subassemblies. The axial load range considered is from 20% to 40% of P_y in increments of 5%, where P_y is the column axial yield load calculated using the nominal section area and the yield strength obtained from coupon tests of either the ASTM A992 (wide flange columns) or ASTM A500 Gr. B steel (HSS column). The two lateral loading protocols used in this study are shown in Fig. II.4. The symmetric cyclic (SC) loading protocol is the one prescribed by the AISC Seismic Provisions (2016a) for prequalifying seismic moment connections and consists of a sequence of fully reversed, continually increasing drift levels that increase from 0.00375 rad. to 0.08 rad. The cyclic ratcheting (CR) protocol was developed by Wu et al. (2018a) and represents a collapse-consistent progression of drift levels that incorporate ratcheting behavior up to a maximum rotation of 0.04 rad. Only an axial load ratio of 30% of P_y was used with the CR protocol.

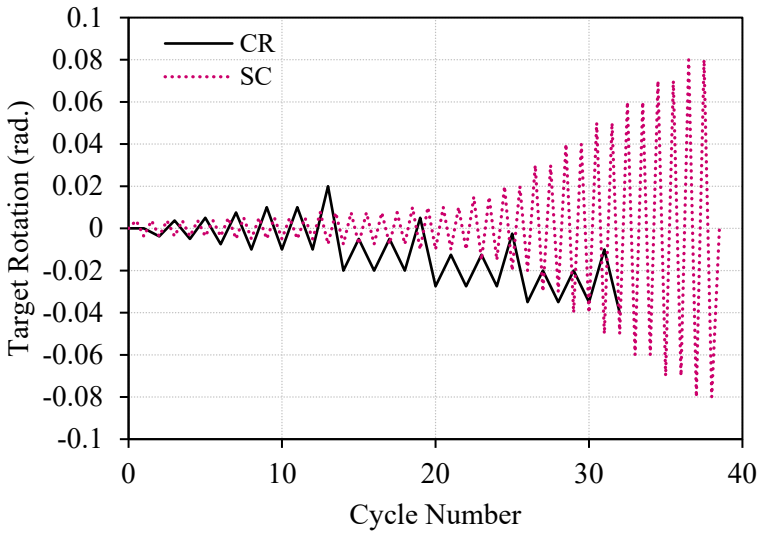

Figure II.4. Lateral loading protocols used for the subassembly finite element analyses and experimental tests.

Finite Element Analysis Results

General behavior

The moment-rotation behavior of each subassembly under the SC and CR loading protocols is presented in Figs. II.5 and II.6, respectively. From Fig. II.5 it is clear that changing the axial load ratio has a significant effect on the overall performance and stability of the subassemblies with every increase in axial load resulting in more capacity degradation over time and an analysis that aborts earlier due to the excessive deformations in the column.

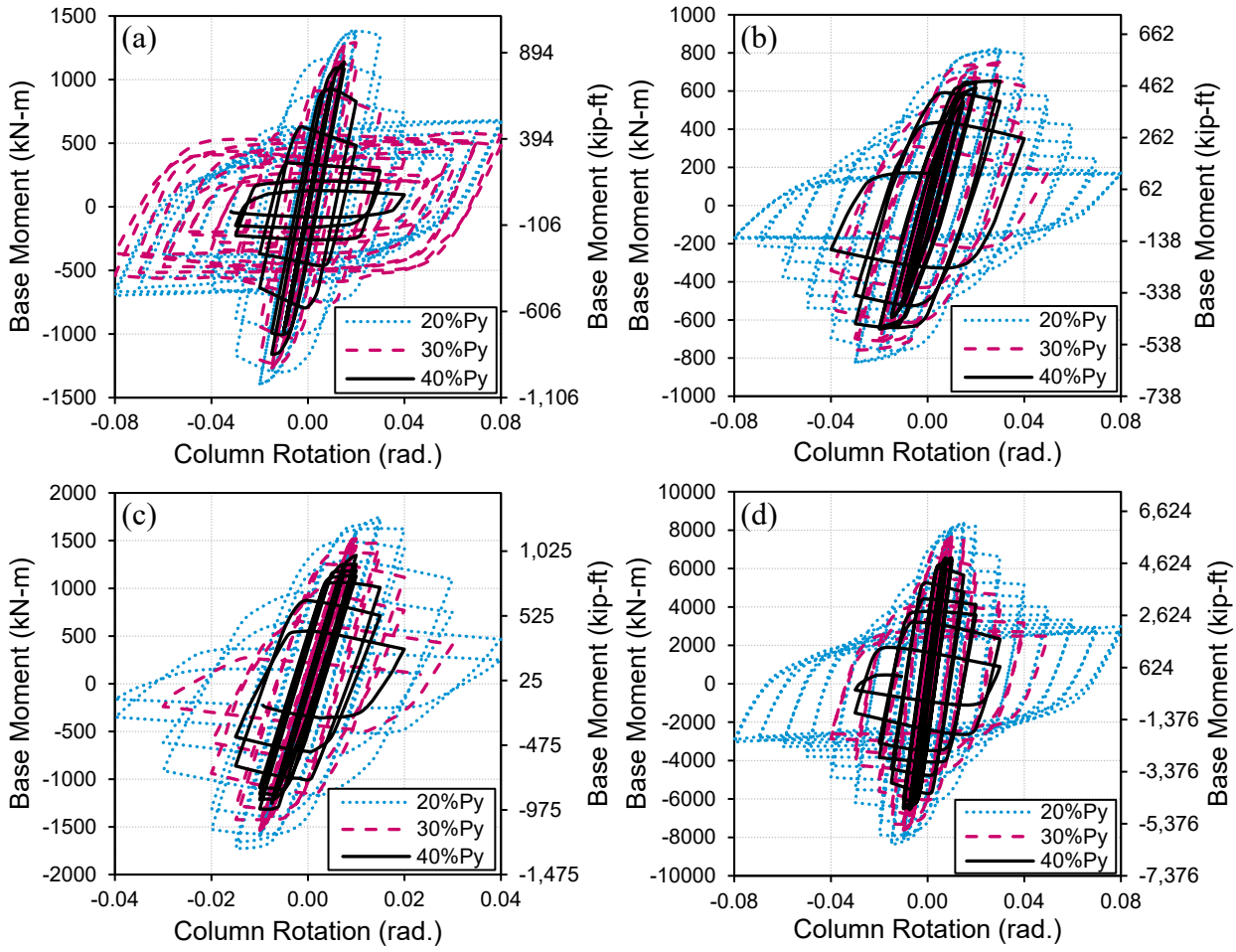

Figure II.5. Moment-rotation behavior of (a) SA1, (b) SA2, (c) SA3, and (d) SA4 under the SC loading protocol at various axial load ratios.

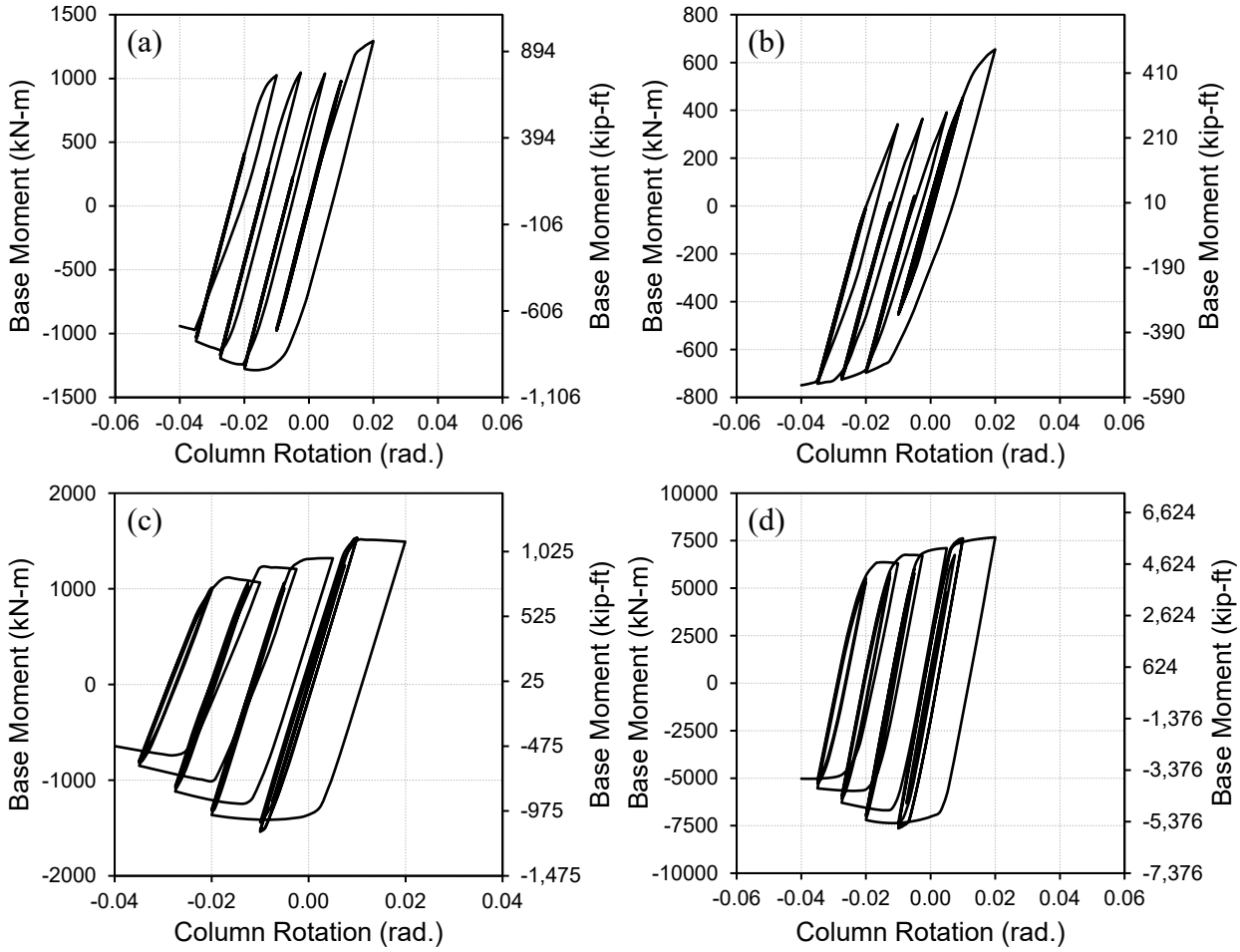

Figure II.6. Moment-rotation behavior of (a) SA1, (b) SA2, (c) SA3, and (d) SA4 under the CR loading protocol at an axial load ratio of 30% of P_y.

Comparing the general behavior of the subassemblies under both loading protocols shows that less capacity degradation is observed when the subassemblies are subjected to the CR loading protocol (Fig. II.6). In the case of SA2, no signs of moment capacity degradation were observed throughout the CR protocol. Further, all of the CR analyses were able to run to completion given that the columns remained more stable as these subassemblies experienced significantly less deformation due to buckling than when subjected to the SC protocol.

Effects of the axial load ratio

Varying the axial load on the column has a significant effect on the cyclic performance of each subassembly in terms of maximum moment capacity, moment capacity degradation with continued cycling, and overall stability. In terms of the column's maximum moment capacity, all of the wide flange column subassemblies experience a similar rate of decrease in moment capacity as the axial load ratio increases (Fig. II.7a). However, the subassembly with the HSS column (SA1) exhibits the least amount of decrease in its overall moment capacity as the axial load increases to 40% of P_y. Figs. II.7b and II.7c show the column's moment capacity degradation at the 2% and 4% drift levels. At 2% drift, subassembly SA2, which represents the stockier pre-Northridge wide flange column, exhibits no moment capacity degradation for all axial load ratios and subassembly SA1 only shows degradation at the 35% and 40% axial load ratios. Conversely, the subassemblies with deep wide flange columns, SA3 and SA4, experience moment capacity degradation at the 2% drift level for every axial load ratio with SA3 having degraded 50% and 73% at 35% and 40% of P_y, respectively. The magnitude of this degradation is considerably large for an SMF at this drift level.

Considering the performance of the subassemblies at the 4% drift level, some of the simulations become too unstable and abort prior to reaching the first cycle to 4% drift. This behavior is typically associated with a column whose moment capacity is approaching zero. Therefore, it is reasonable to assume the structure is nearing collapse due to loss of axial and lateral load carrying capacity. Specifically, subassemblies SA3 and SA4, which represent the subassemblies with deep, slender wide flange column sections, do not reach 4% inter-story drift when the axial load ratio is 30% and 40% of P_y, respectively, and show significantly higher

moment capacity degradation at lower axial load ratios compared to the other subassemblies (Fig. II.7c).

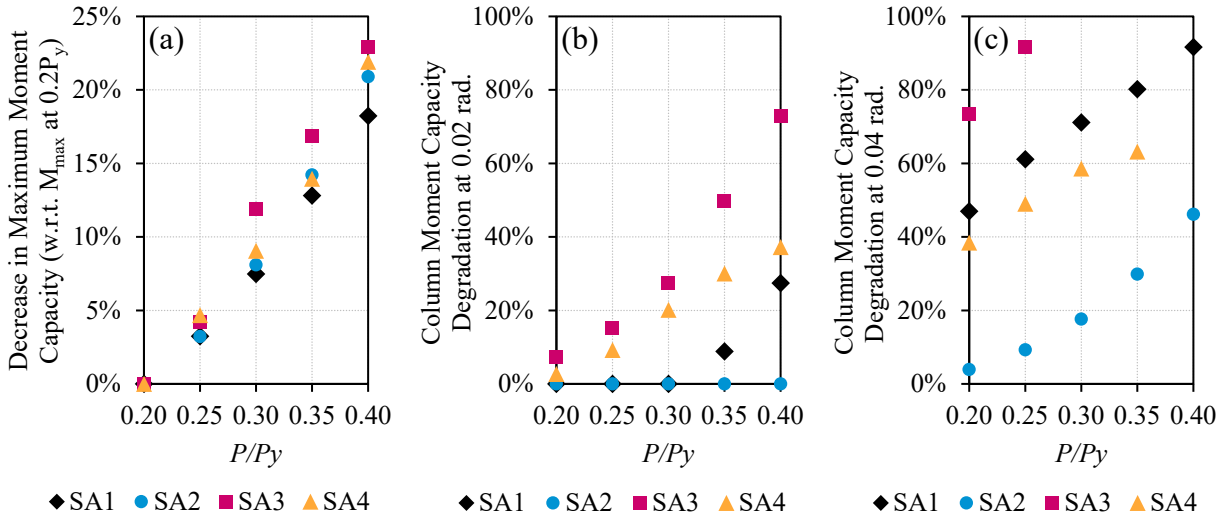

Figure II.7. (a) Decrease in column maximum moment capacity, and (b and c) column moment capacity degradation at 2% and 4% drift, respectively. SC loading protocol.

Although the section sizes in SA1 (HSS column) are selected to be comparable in strength to SA3, SA1 exhibits a different behavior due to the presence of the HSS column. At 4% drift, SA1 exhibits lower moment capacity degradation compared to SA3 at all axial load levels (Fig. II.7c). As shown in Figs. II.8b and II.8d, this difference in performance can be attributed to the wide flange column undergoing more deformation due to local buckling than the HSS column at the same drift level. In the case of SA1, after significant local buckling occurs at the base of the column, the column starts to undergo shortening. As a result, a self-contact interaction is observed which affects the overall behavior of the subassembly (Fig. II.8a). Because fracture is not considered in the models, it is likely that this behavior is not accurate at higher rotation levels (more than 0.06 rad.) where fracture initiation has been observed in the corners of HSS members during previous experimental tests (Fadden and McCormick 2012).

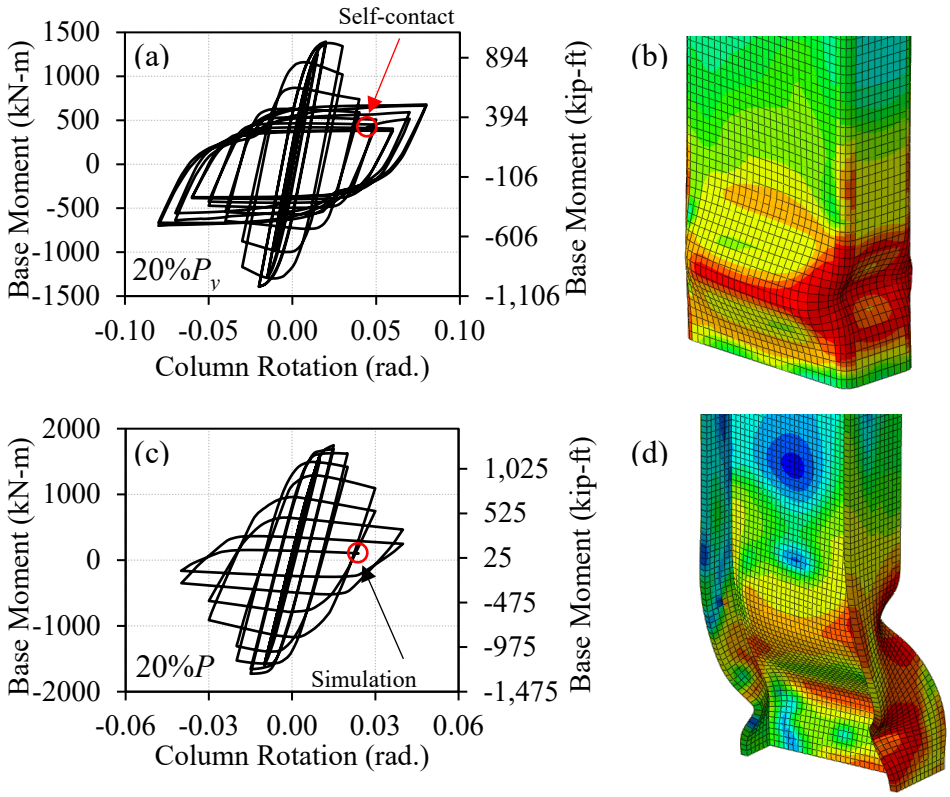

Figure II.8. (a and c) Moment-rotation behavior of SA1 and SA3, respectively, under the SC loading protocol and (b and d) local buckling at the column base during the first 4% inter-story drift cycle for SA1 and SA3, respectively.

Effect of the loading protocol

As shown in Fig. II.9, there are significant differences in performance when comparing the SC and CR loading protocols. In general, the SC protocol places larger demands on the subassembly and does not account for the ratcheting effect often seen in sidesway collapse scenarios. SA3 does not reach the first 0.04 rad. cycle when subject to an axial load ratio of 30% of P_y under the SC protocol. However, under the CR protocol it is able to undergo the whole protocol at the 30% of P_y axial load level. The main reason for the difference in performance is the amount of observed local buckling as seen in Figs. II.9b and II.9d. Because the SC protocol consists of fully reversed cycles, the local buckling of both flanges of the column at the column base is much more significant, while in the CR protocol a majority of the local buckling is

concentrated in one of the flanges due to the cyclic ratcheting not allowing the column to undergo a full reversed cycle in the opposite direction. As a result, the columns in the subassemblies that underwent the SC protocol experience considerably larger deformations and subsequent loss in moment capacity and axial load carrying capacity resulting in poorer cyclic performance when compared to its counterpart that underwent the CR protocol. Similar results are observed across all four subassemblies. These results suggest that it is important to consider multiple loading scenarios as some cases may be overly demanding and result in an exaggerated poor behavior.

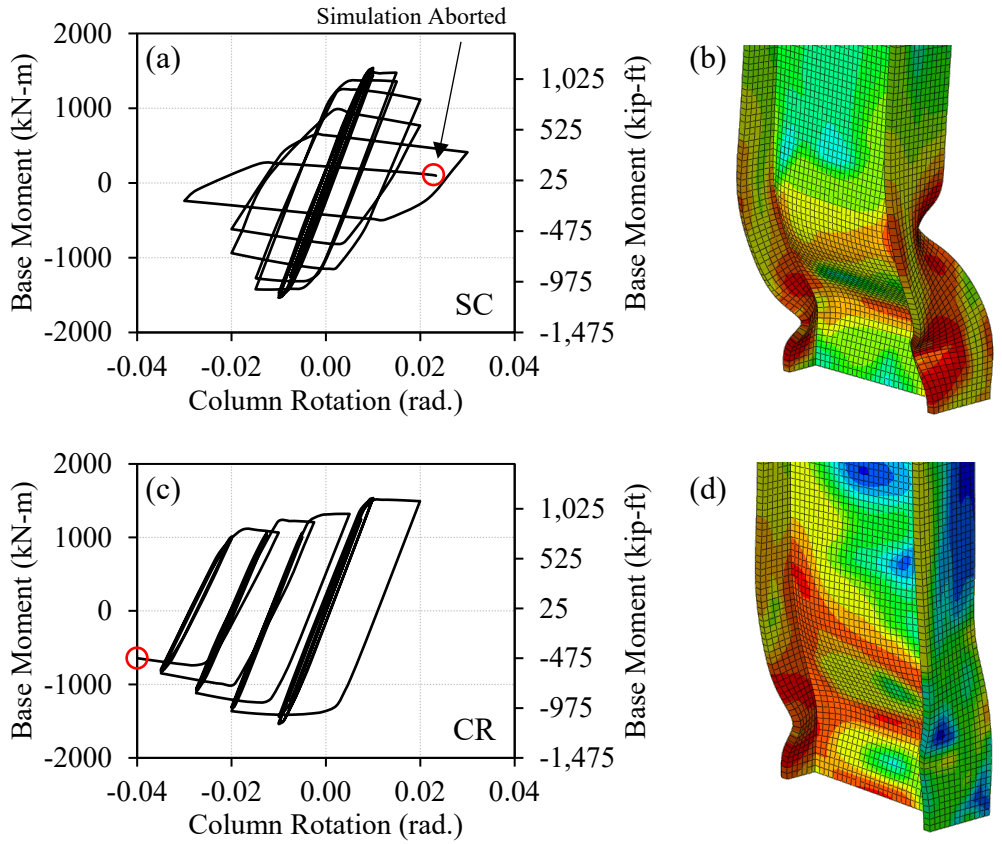

Figure II.9. (a) SA3 column base moment versus column rotation under the SC protocol with 0.3P_y axial load and (b) an image of the column base deformation at the 2nd 3% drift cycle. (c) SA3 column base moment versus column rotation under the CR protocol with 0.3P_y axial load and (d) an image of the column base deformation at the 4% drift level.

Key findings of the finite element study

The axial load ratio and the applied lateral loading protocol were found to have a significant influence on the cyclic performance of the subassemblies. Changing the axial load ratio was shown to affect the behavior of the subassemblies with regards to their maximum moment capacity, moment capacity degradation, and overall stability. With regards to the lateral loading, the SC protocol was shown to be a significantly more demanding protocol than the CR protocol due to incorporating fully reversed cyclic drifts that result in local buckling on both flanges of the column. Under the SC protocol, only the pre-Northridge column in SA2, while subjected to an axial load ratio of 30% of P_y or lower, managed to meet the high ductility performance criteria of maintaining 80% of its maximum moment capacity by 4% drift. These results show that when subjected to the SC protocol, some deep wide flange columns, such as the ones in SA3 and SA4, are not able to achieve their expected ductility. By contrast, when a column is subjected to the CR loading protocol the majority of the local buckling is concentrated towards the compression flange which allows the tension flange to retain more of its strength. As an example, the column in SA3 was not able to reach the first 0.04 rad. cycle in the SC protocol while subjected to an axial load of 30% of P_y. However, this same subassembly was able to undergo the complete CR loading protocol up to 0.04 rad at the same axial load. These results highlight the importance of considering different loading protocols as some may impose unrealistic demands on the specimen.

Experimental Testing of Wide Flange Subassemblies

An experimental program follows the finite element study to further explore the cyclic behavior of the cruciform specimens and examine the potential interactions between the local and global instabilities of deep, slender wide flange columns. The experimentally tested subassembly is a half-scale version of SA3 in Table II.1.

Test setup and methodology

The beam and column sections used for the experimental specimen are a W250×28.4 (W10×19) and a non-standard W310×44.5 (W12×30), respectively. The flange width of the column section is reduced from 165.1 mm (6.5 in.) to 117.5 mm (4.63 in.) to ensure that the section's geometric properties are appropriately scaled. After considering the reduction in flange width, the half-scale local slenderness ratios are $b_f/2t_f$ = 5.26 and h/t_w = 41.8. These values are 14.6% larger for $b_f/2t_f$ and 6.6% larger for h/t_w when compared to the full-scale column (Table II.2). The radius of gyration around the strong (r_x) and weak (r_y) axes are reduced to 50.0% and 51.3% of the values of the full-scale specimen, respectively (Table II.2). The flange width modification reduces the column section's cross-sectional area (A_g) and plastic section modulus around the strong axis (Z_x) by 20.1% and 24.6%, respectively, when compared to its nominal values.

A schematic of the cruciform specimen is presented in Fig. II.10. Plates are added to the subassembly at the beam and column ends to facilitate connection of the hydraulic actuators to the specimen. A plate also is added at the top of the column to attach a loading beam that is used to apply the column axial load. The beam-to-column connection is a prequalified RBS moment connection and includes 9.53 mm (0.375 in.) thick continuity plates in the panel zone. The base plate is 57.2 mm (2.25 in.) thick and was designed following the procedure in Fisher and Kloiber

(2006) to ensure that the subassembly behaves in a ductile manner and most of the rotation occurs in the column.

Table II.2. Comparison of geometric properties between the full-scale and half-scale column sections.

Specimen	Column Section [mm×kg/m]	d [mm | in.]	$b_f/2t_f$	h/t_w	r_x [mm | in.]	r_y [mm | in.]
Full-Scale	W610×153 [W24×103]*	622 | 24.5	4.59	39.2	254 | 10	50.5 |1.99
Half-Scale[a]	W310×44.5 [W12×30]*	312 | 12.3	5.26	41.8	127 | 5	25.9 | 1.02
Ratio		0.50	1.15	1.07	0.50	0.51

[a] Initial section size shown prior to reducing the flange width

* Section in US Customary Units (in×lb/ft)

The experimental test setup is shown in Fig. II.11. Five hydraulic actuators are used to apply the lateral load, axial load and appropriate boundary conditions at the beam ends. A 670 kN (150 kip) actuator (2 in Fig II.11) is connected to the top of the column and used to apply the lateral displacements associated with the lateral rotations prescribed by the lateral loading protocol in displacement control. Two 445 kN (100 kip) actuators (5 and 6 in Fig. II.11) are connected to the loading beam attached to the top of the cruciform specimen. These two actuators are run in force control and pull down simultaneously on the loading beam to apply the prescribed constant axial load on the column. The axial loading actuators are pinned on each end allowing them to rotate in-plane with the specimen as the lateral displacements are being applied. The loading beam is designed to remain elastic throughout testing. Two 222 kN (50 kip) actuators (3 and 4 in Fig. II.11) are connected at the beam ends and are used to enforce a realistic boundary condition at the beam ends. These beam actuators are set up in displacement control with their prescribed displacement dependent on the axial shortening of the column. The input displacement for the beam actuators is based on feedback from a string potentiometer spanning from the beam-to-

column moment connection to the base plate of the column. As column shortening occurs, the beam actuators respond accordingly with the same displacement so as to keep the inflection point of the beams (i.e. subassembly beam ends) at the same height as the beam-to-column moment connection, which would be expected in the actual structure. The beam actuators are pinned at the connection point to allow the beams to move and rotate freely in-plane. In a similar manner to the FE model, this configuration is meant to take into account the column axial shortening that would occur across all of the columns at the first story of the seismic moment frame from which the subassembly is extracted. Out-of-plane bracing is provided at the beam-to-column moment connection, at appropriate points along the beam flanges, and at the ends of the beams (yellow and blue frame in Fig. II.11).

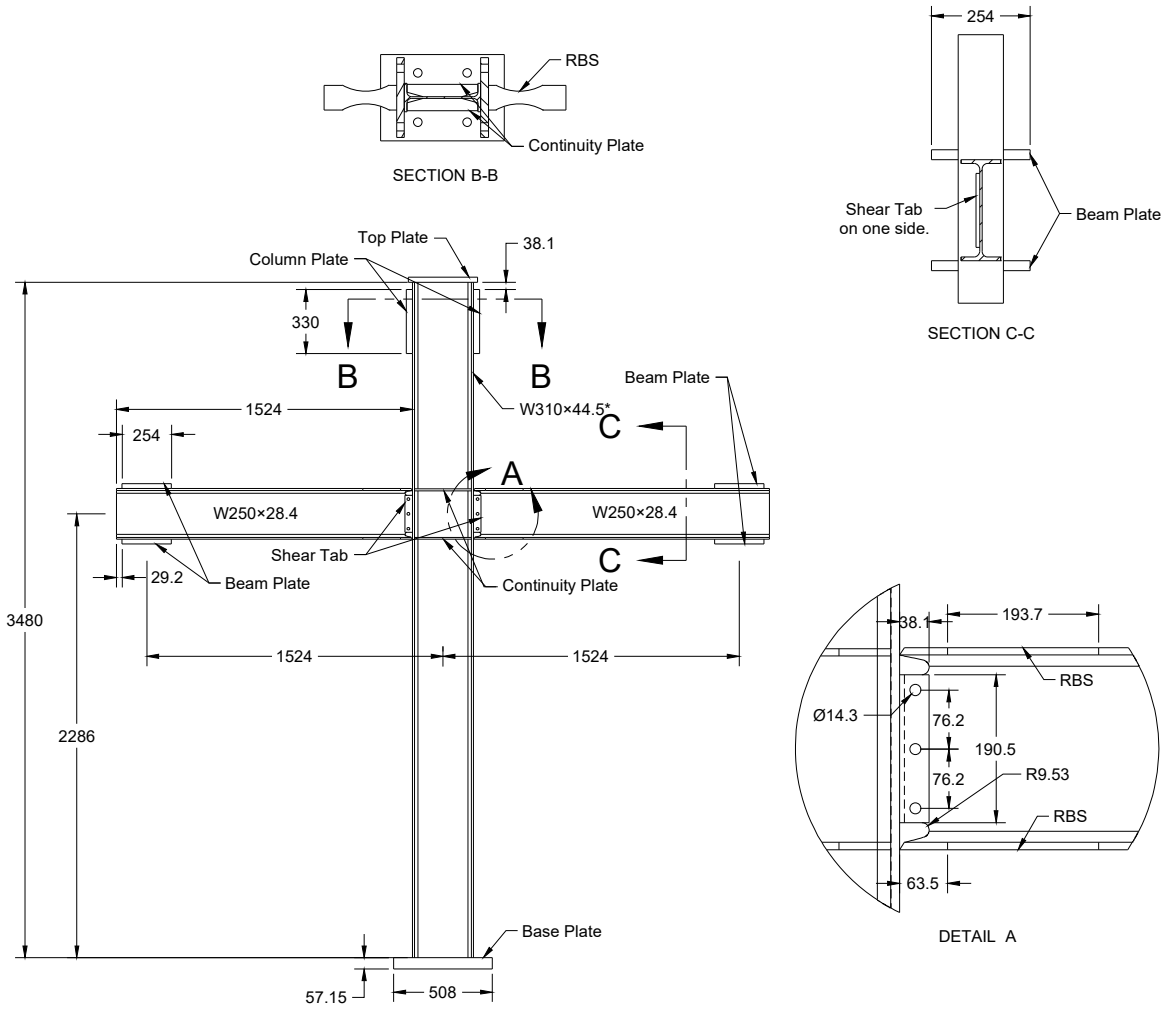

Figure II.10. Schematic of the cruciform specimen. Units: mm

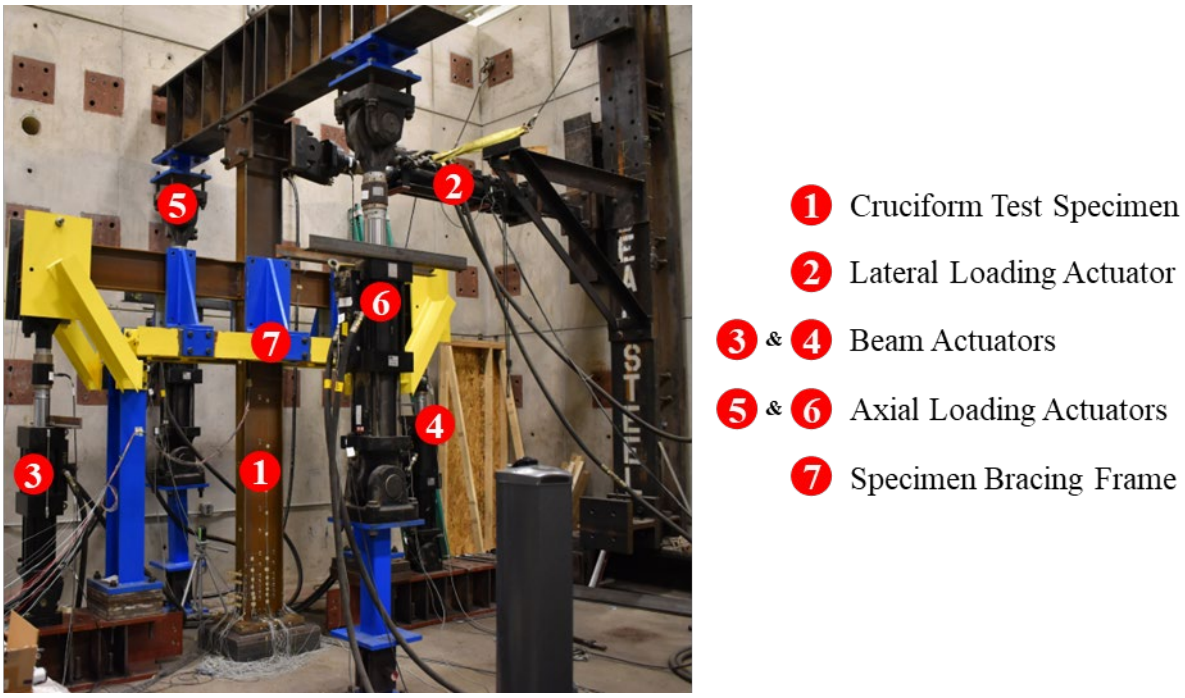

Figure II.11. Photograph of the experimental test setup of the cruciform subassembly.

Data acquisition

The cruciform subassembly is instrumented with a variety of measurement devices and sensors to obtain relevant information regarding the cyclic performance of the specimen. Measurements regarding the lateral displacement of the subassembly and the forces associated with these displacements are obtained directly from the load cells and displacement measurement devices attached to the actuators. As previously mentioned, the column axial shortening is measured by attaching a string potentiometer between the column based and the lower continuity plate in the beam-to-column moment connection. Multiple strain gages are placed along the column flanges near the column base to study the strain distribution that occurs as a consequence of the local and global buckling. Additional strain gages are placed along the top flange of the beams near the RBS to check whether the RBS region is yielding and forming a plastic hinge. Three-direction strain gage rosettes are placed in the column panel zone to measure the shear

strain. A diagram of the placement of the strain gages is presented in Fig. II.12. Lastly, a grid of infrared markers is placed near the column base on the flanges and on the web. These markers are tracked in 3D space to measure the amount of rigid body rotation that occurs and also provide data regarding the buckled shape of the column at the column base. The global buckling shape was measured by tracking the out-of-plane displacement of the column web centerline markers with regards to their starting positions. The local buckling shape was measured by tracking the relative in-plane displacement of the multiple rows of markers placed in the column flanges.

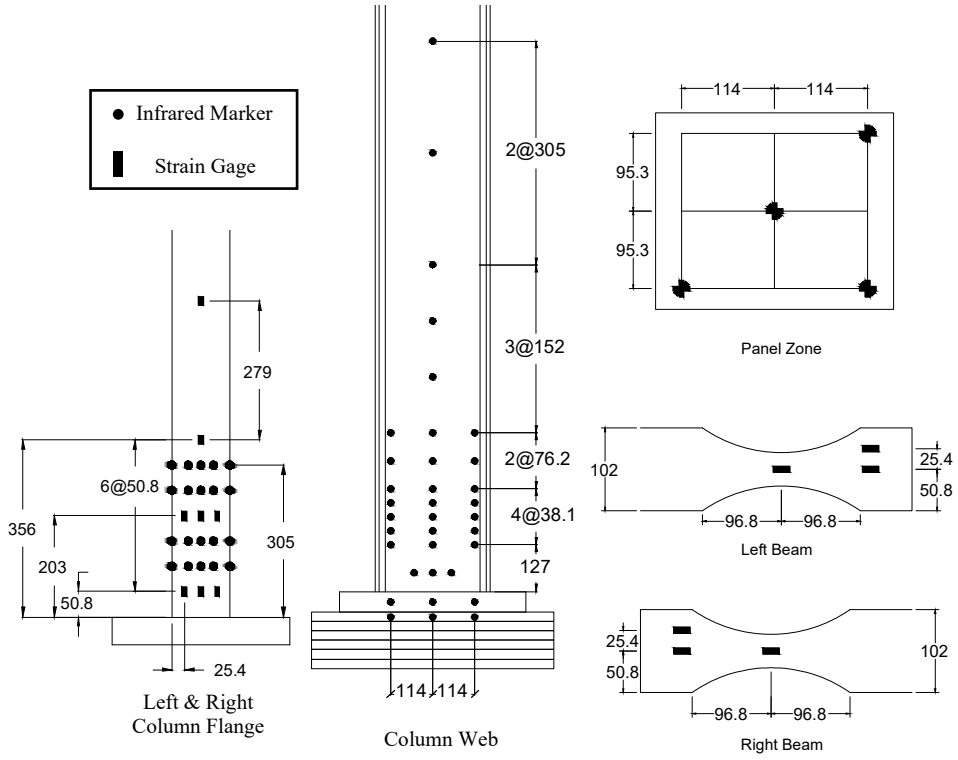

Figure II.12. Placement of infrared markers and strain gages on the test specimen. Units: mm

Test matrix

Three identical wide flange cruciform specimens are experimentally studied under large bending moments and axial load. The experimental test matrix is presented in Table II.3. All three tests were conducted using an axial load ratio of 20% of P_y, which is calculated as

$$P_y = R_y F_y A_g \quad \text{(Eq. II.1)}$$

where R_y is the ratio of the expected yield strength to the nominal yield strength, F_y is the nominal yield strength, and A_g is the cross-section area considering the reduction in flange width. Using Eq. II.1 with an R_y value of 1.1 for ASTM A992 steel, a nominal F_y value of 345 MPa (50 ksi), and a reduced area of 4,529 mm^2 (7.02 in^2), the applied axial load during the tests is 343 kN (77.2 kip). The column section is classified as highly ductile based on its local slenderness ratios ($b_f/2t_f$ = 5.26 | h/t_w = 41.8) and applied axial load. The highly ductile limits for $b_f/2t_f$ and h/t_w are 7.35 and 49.7 with an axial load ratio of 20% of P_y, respectively. The first two tests (W1 and W2) are conducted using the SC loading protocol in Fig. II.4, and the last test (W3) uses the CR loading protocol to investigate whether the differences in cyclic performance due to the different protocols are as significant as were observed in the preliminary finite element study.

Table II.3. Experimental test matrix.

Subassembly ID	Column Section (mm×kg/m)	Beam Section (mm×kg/m)	Axial Load	Lateral Loading Protocol
W1	W310×44.5[a]	W250×28.4 [W10×19][*]	20% of P_y (343 kN) (77.2 kips)	SC
W2	[W12×30][a,*]			SC
W3	(b_f of 117.5 mm)			CR

[a] Initial section size shown prior to reducing the flange width
[*] Section in US Customary Units (in×lb/ft)

Results of the Experimental Subassembly Tests

After conducting the first test (W1) some changes were made to the test setup and the instrumentation plan for the remaining tests. The description of the test setup presented in the previous sections refers to the final version of the test setup that was used for test specimens W2 and W3. The changes to the test setup were made to address issues that were noticed during the test of subassembly W1, which included lateral torsional buckling of the beam members at the beam ends during the 3% drift cycles and inaccurate measurement of the column shortening. The lateral torsional buckling in the beam was fixed by providing additional lateral bracing at the beam ends that can be seen as the yellow extension in Fig. II.11. To address the measurement of the column axial shortening, the linear variable differential transformer (LVDT) was replaced by a string potentiometer that extended from the beam-to-column connection to the column base. This adjustment in the instrumentation allowed the measurement device to rotate freely and follow the lateral displacement of the column, resulting in only the column shortening being measured. Further changes to the instrumentation plan were implemented due to more capable data acquisition system being available after the first test was conducted, allowing for additional strain gages to be used simultaneously. The strain gage instrumentation plan for specimen W1 followed the one presented in Fig. II.12 with the exception that no strain gages were placed in on the right beam or right column flange. Additionally, the grid of infrared markers placed along the column flanges was also added for testing specimens W2 and W3 to more accurately capture the buckled shape of the column flange in these later tests given the role that local buckling plays in the overall performance of the column.

Although testing of specimen W1 was ended prematurely due to the lateral torsional buckling of the beam member, the data obtained from the test is presented since the cycles prior to lateral

torsional buckling of the beam provide information in regards to the initial behavior of the deep, slender wide flange columns under large axial load and bending moments when tested in a subassembly configuration. However, it is worth noting how some of the problems may have affected the results. Since the input displacement of the actuators at the beam ends is a function of the column axial shortening measurement and this measurement was found to be inaccurate (essentially showing no axial shortening throughout the duration of the test), the beam actuators, acting as adjustable links at the ends of the beams, did not change length. This behavior resulted in the beams applying a higher moment at the beam-to-column connection and a higher shear force on the column panel zone. Comparing the magnitude of this moment couple at the beam-to-column connection in test W1 at the first 3% target drift cycle with that of test W2 shows that the beam actuators in test W1 were applying a moment that is 21.7% higher than it would have been had the column axial shortening been correctly measured. Combined with the fact that test specimen W1 did not have lateral bracing at the beam ends, significant lateral torsional buckling of the beam was observed during testing. Due to these issues the test for W1 was only conducted up to the 3% target drift cycle.

The column base moment is calculated from a free body diagram that considers the measured column axial shortening and the forces and displacements of the multiple actuators used to conduct the test. The actual rotation of the column is calculated by removing the rigid body rotation at the base of the test setup following a similar procedure described in Wei (2017) through the use of the infrared displacement measurements. Due to the presence of the rigid body rotation, the actual column rotations were smaller than the target rotations. Every column rotation specified in the following text is accompanied by its target rotation to clarify during which target rotation cycle an event is observed (e.g., 1.6% drift was achieved during the 3%

target cycle). Also, every plot that incorporates rotation values is constructed using the actual column rotation, not the target rotation.

Specimen W1

Specimen W1 was subjected to the symmetric cyclic loading protocol. The hysteretic behavior of the column is presented in Fig. II.13. The largest column rotations that were reached during testing were 0.016 rad. (target: +3%) and -0.014 rad. (target: -3%) for the positive and negative cycles, respectively. The maximum base moments recorded in the positive and negative cycles, respectively, are 209 kN-m (154 kip-ft) and -230 kN-m (-170 kip-ft). These moment values are 3.3% and 13.8% higher than the expected plastic moment capacity of the column, respectively, which is calculated as

$$M_p = R_y F_y Z_x \quad \text{(Eq. II.2)}$$

where Z_x is the plastic section modulus of the column considering the reduction in flange width. Using Eq. II.2 with an R_y value of 1.1, a nominal F_y value of 345 MPa (50ksi) , and a Z_x value of 533×10^3 mm^3 (32.5 in^3) the expected plastic moment capacity is 202 kN-m (149 kip-ft).

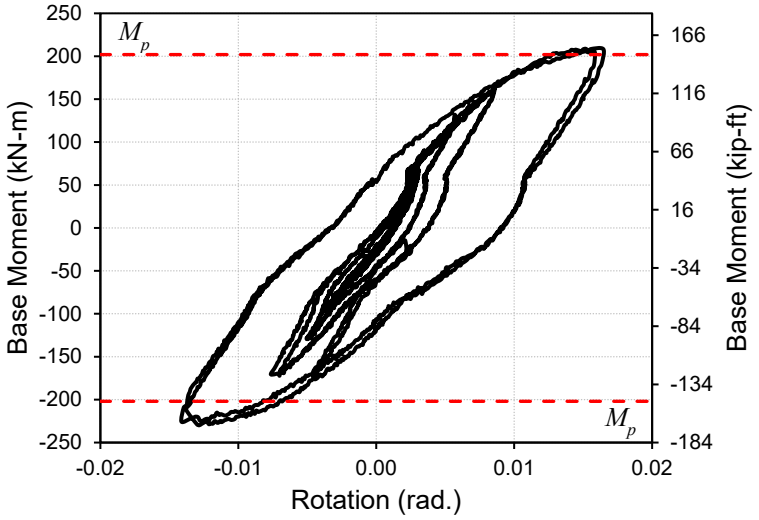

Figure II.13. Column base moment versus rotation behavior for specimen W1.

While the test for specimen W1 was only conducted up to the 3% target drift cycle, the column rotations reached during the test were still large enough to push the column past its yield point, but not large enough for any degree of moment capacity degradation to occur. A visual inspection of the column base after the test was stopped revealed some slight buckling in the column web had begun to develop (Fig. II.14). The strain measurements along the centerline of the left column flange also confirm the column was pushed past its yield point (Fig. II.15a). The value used as the steel's yield strain is 0.190% and is calculated as

$$\varepsilon_y = \frac{R_y F_y}{E} \qquad \text{(Eq. II.3)}$$

where E is the steel's elastic modulus taken as 200 GPa (29,000 ksi).

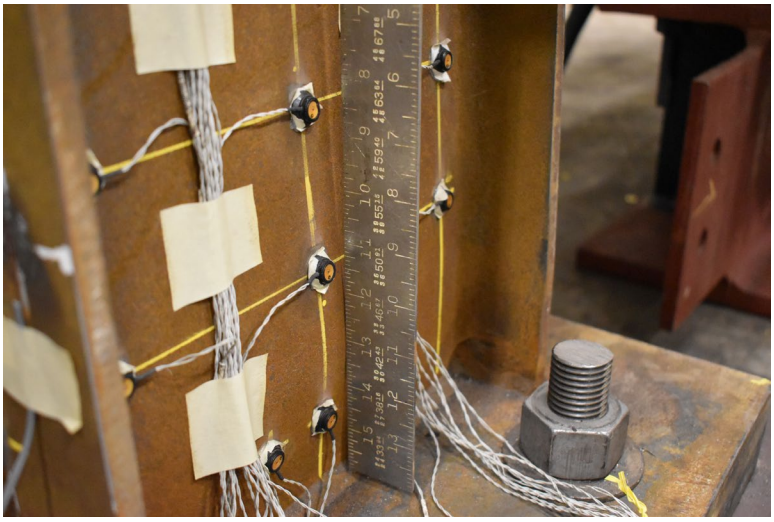

Figure II.14. Magnitude of web local buckling at the column base of specimen W1 after the completion of the test.

The strain gages placed on the top flange of the left beam confirm yielding initiates occurs in the RBS region and near the column flange, but no local buckling is observed in the beam. The strain gage rosettes in the panel zone are used to determine the engineering shear strain which is calculated as

$$\gamma = 2\varepsilon_3 - (\varepsilon_1 + \varepsilon_2) \qquad \text{(Eq. II.4)}$$

where ε_1, ε_2, and ε_3 are the horizontal, vertical, and diagonal strain gage measurements, respectively. The engineering shear strain calculated from the strain gage rosette at the middle of the panel zone is presented in Fig. II.15b. The value assumed as the steel's shear yield strain is 0.284% and is calculated as

$$\gamma_y = \frac{R_y F_y}{\sqrt{3}G} \quad \text{(Eq. II.5)}$$

where G is the steel's shear modulus taken as 77.2 GPa (11,200 ksi). Based on the shear strain data, the panel zone undergoes yielding, experiencing up to 2.6% shear strain at a rotation of 0.016 rad. (target: +3%).

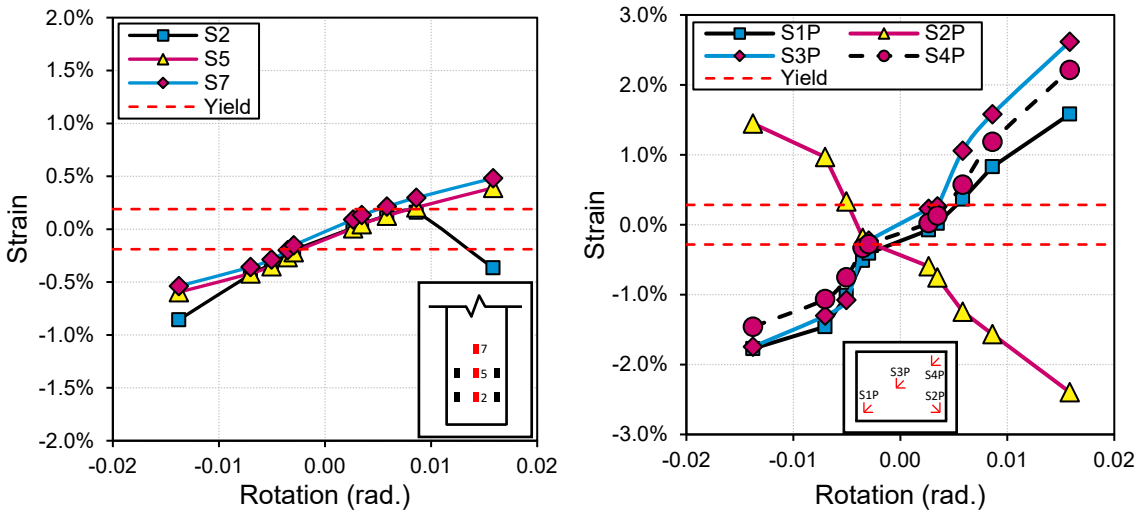

(a) (b)

Figure II.15. (a) Strain measurements along the centerline of the column's left flange and (b) shear strain measurements at the column panel zone. Data points taken at the first cycle to various drift cycle magnitudes of test specimen W1.

A visual inspection of the beam-to-column connection after the test revealed a significant amount of buckling in the panel zone region (Fig. II.16). It should be noted that the buckling of the panel zone was not observed with specimen W2, even though specimen W2 was pushed to significantly higher drift levels. There are three factors that had a role in the panel zone buckling

during the test for W1. The first two factors, as noted earlier, involve the lack of adjustment of the length of the beam end actuators during the test and the significant twisting experienced by the beams near the end of the test due to lateral torsional buckling. The incorrect shortening measurements resulted in the beam actuators applying a higher force on the beam ends which in turn resulted in a higher moment at the connection and higher shear forces in the panel zone. The lateral torsional buckling also imparted an additional out-of-plane moment on the beam-to-column connection. The third factor is related to an unintended large axial load that was initially applied to the column.

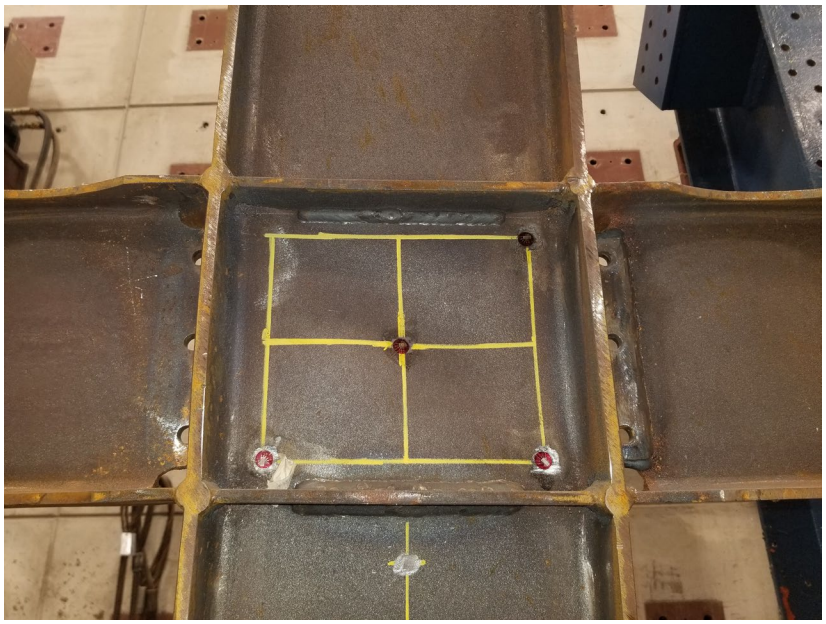

Figure II.16. Buckling observed in the panel zone region of specimen W1 at the end of the test.

Prior to testing, an actuator calibration error resulted in the axial load actuators applying 867 kN (195 kip) of force onto the column member, approximately 0.505P_y. This force was also applied eccentrically as the axial actuators on either side of the loading beam applied force at a different rate, resulting in a permanent out-of-plane global deformation in the column member large enough to be noticed visually. Based on measurements from the strain gages that were

reading at the time of the accidental overload, yielding occurred near the base of the left column flange and at the top-right and bottom-right of the panel zone. It is unknown how much each of these three factors contributed towards the excessive deformations in the panel zone, but given the results from specimen 2 it is clear that the combination of these factors contributed to the buckling that was observed in the panel zone region.

Specimen W2

Given some of the problems that were observed during the testing of specimen W1 and the limited rotation level that was reached with that test, specimen W2 was subjected to the same symmetric cyclic loading protocol and axial load ratio. The changes to the test setup allowed for significantly larger rotations levels to be reached and degradation of the moment capacity to be observed. The hysteretic behavior of the column is presented in Fig. II.17. The largest column rotations that were reached during testing were 0.047 rad. (target: +5%) and -0.032 rad. (target: -4%) for the positive and negative cycles, respectively. The maximum base moments recorded in the positive and negative cycles, respectively, are 248 kN-m (183 kip-ft) and -205 kN-m (-151 kip-ft). These moment values are 23.0 % and 1.6% larger than the expected plastic moment capacity of the column, 202 kN-m (149 kip-ft), respectively.

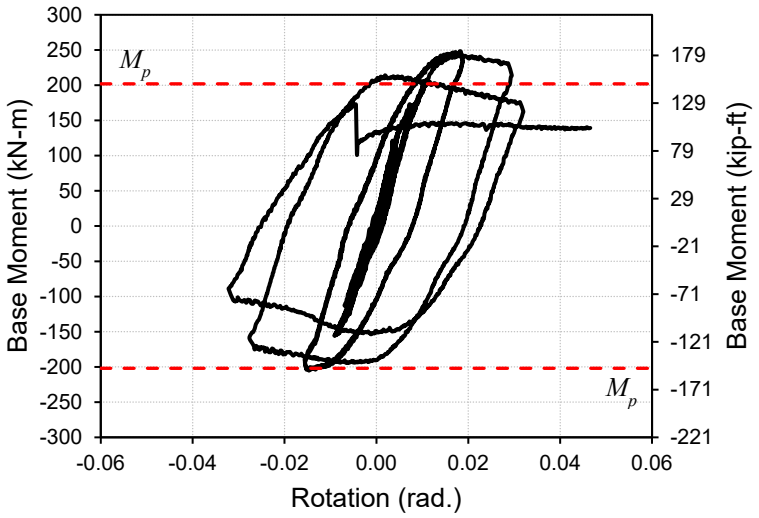

Figure II.17. Column base moment versus rotation behavior for specimen W2.

The deep, slender wide flange column reached its maximum moment capacity at a rotation of 0.018 rad. during the second cycle to 0.019 rad. (target: +3%). This cycle was the same cycle in which out-of-plane bending and web local buckling was first observed in the column. During subsequent cycles significant local buckling develops in the column flanges near the base, resulting in continued degradation of the moment capacity at the base of the column. This degradation reaches 20% of its maximum moment capacity at a rotation of -0.028 rad. (target: -4%), suggesting that the test specimen is not able to maintain 80% of its maximum moment capacity out to 4% drift when subjected to the symmetric cyclic loading protocol, which is the criteria required of beams in SMF connections. This finding brings into question the seismic classification of the column as a highly ductile member that can withstand large rotation levels. By the second cycle to 0.032 rad. (target: +4%) a combination of local buckling and out-of-plane global buckling is observed. During the following cycle to 0.047 rad. (target: +5%) the magnitude of the buckled shape further increases (Fig. II.18), at which point the test was stopped. As shown in Fig. II.19, during this 0.047 rad. (target: +5%) cycle the column

experiences 135 mm (5.3 in.) of out-of-plane displacement at a column height of 889 mm (35 in.). The majority of the local buckling in the column is concentrated within 203 mm (8 in.) of the column base. The development of local and global bucking also results in column shortening with specimen W2 exhibiting 35 mm (1.38 in.) of shortening by the end of the test (Fig. II.20).

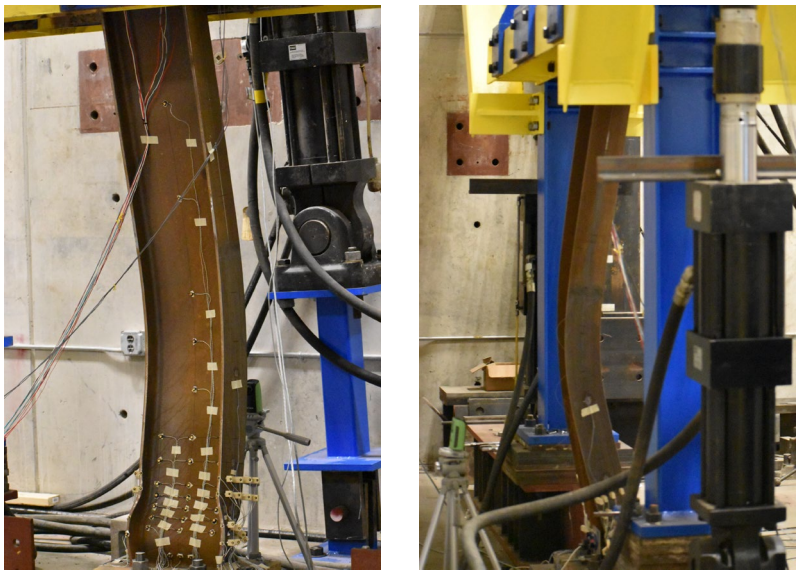

(a) (b)

Figure II.18. (a) Front and (b) side views of the specimen W2 column during the first 0.047 rad. cycle (target: +5%).

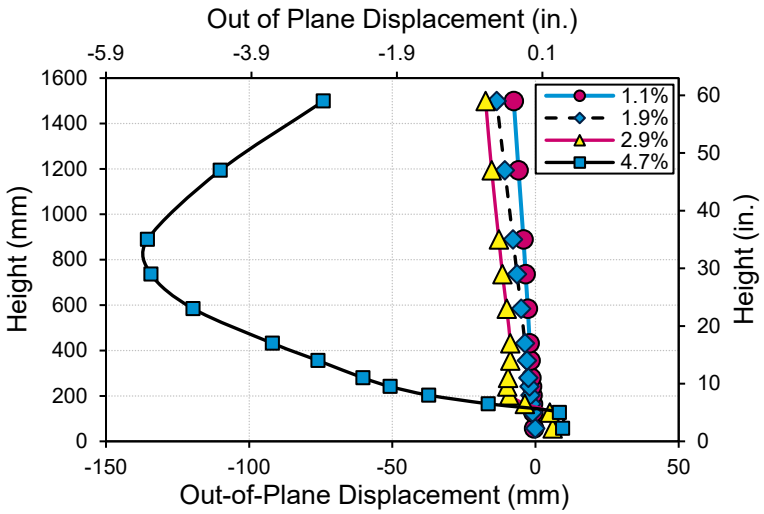

Figure II.19. Out-of-plane displacement of the column web centerline in specimen W2 during the first cycle to various drift magnitudes.

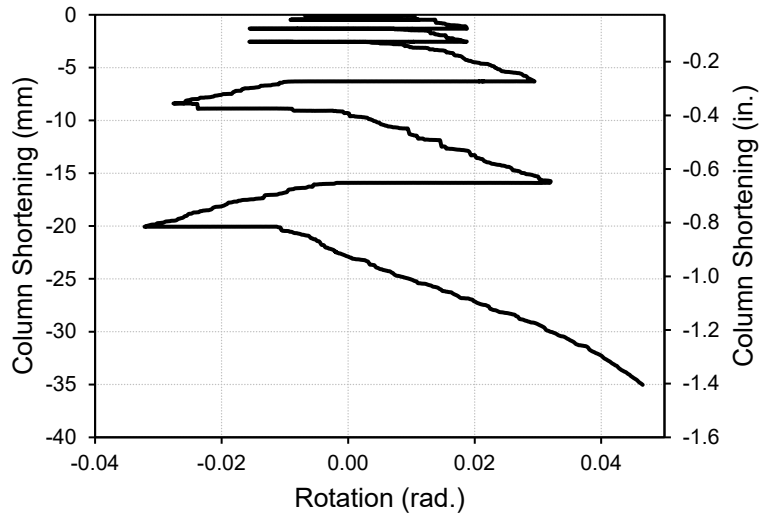

Figure II.20. Column axial shortening of specimen W2 with respect to actual rotation measured at the column base.

Measurements of the extent of local buckling at the column base are presented in Fig. II.21. These measurements are obtained by comparing the in-plane displacement of the infrared markers attached to the column flanges (Fig. II.12). Each horizontal row contains five markers distributed across the column flange. The measurements presented in Fig. II.21 are the difference

in in-plane displacement between the markers at the edges of the flanges and the corresponding marker placed at the centerline of each row. This approach provides an accurate measurement of the degree of local buckling because the web limits out-of-plane deformation at the centerline of the flange resulting in the majority of deformation occurring away from the flange centerline.

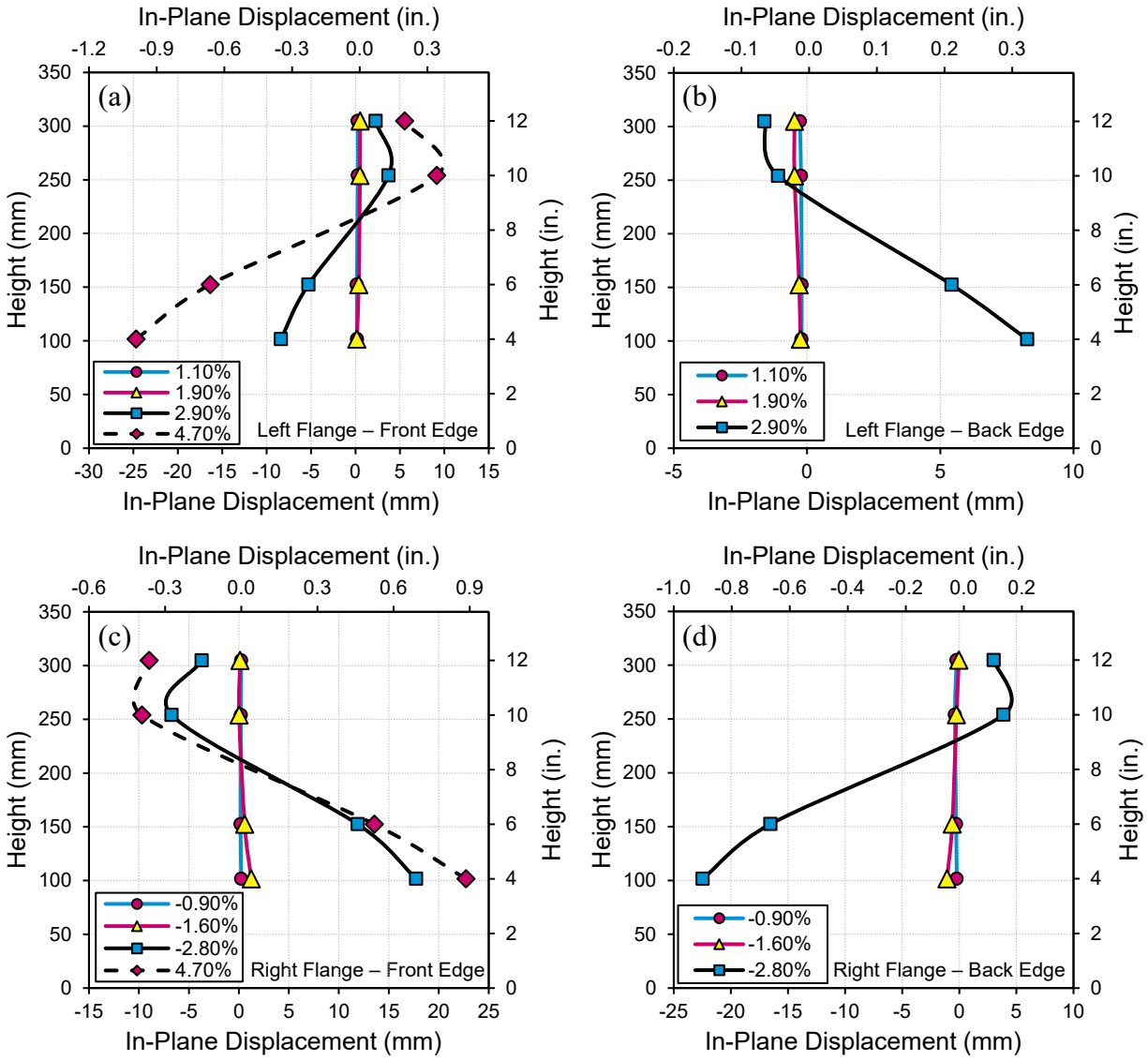

Figure II.21. In-plane displacement of the (a & c) front and (b & d) back edges of the (a & b) left and (c & d) right column flange of specimen W2 during the first cycle to various drift magnitudes.

Little local buckling is observed up to the first cycle to -0.016 rad. (target: -3%). At most, around 1.2 mm (0.05 in.) of deformation is measured at this drift level. During the following cycle to 0.029 rad. (target: +4%) the behavior changes drastically and visible deformation is observed in the flanges of the column near the column base. Around 8.4 mm (0.33 in.) of deformation is measured at the edges of the left column flange at this point in the loading protocol. Repeat cycles at this drift level continue to increase the degree of local buckling as shown in Fig. II.21c & II.21d where 22.5 mm (0.89 in.) of deformation are measured in the right column flange during the first cycle to -0.028 rad. (target: -4%). At 0.047 rad. (target: +5%), the front edges of the left and right flanges experience around 24.7 mm (0.97 in.) and 22.7 mm (0.89 in.) of deformation, respectively (Fig. II.22a). Accurate measurements for the back edge of the column flanges are not available during this cycle because the infrared markers were blocked from view due to excessive deformation. Visually, the back edge of the column flanges experienced significantly more deformation than the front edge (Fig. II.22b) resulting from the interaction between the global and local buckling of the column. During the 0.047 rad. cycle (target: +5%) the column undergoes significant global buckling shaped in a way that puts the back edges of the column flanges near the column base in compression (Fig. II.19). The combined effect of the global and local buckling results in further deformation towards the back of the column flanges.

The strain measurements along the column flanges provide further insight into the stress distribution that results as a consequence of the combined buckling behavior. The strain profile across the column flanges is presented in Fig. II.23. The bottom row of strain gages are those closest to the region that experienced the most deformation due to local buckling (i.e., strain gages S1 through S3 in the left flange and S9 through S11 in the right flange). In this row, the

strain near the back edge of the flanges (S1 & S11) is higher after the onset of buckling than the strain near the front edge (S3 & S9). This behavior is reversed when looking at the strain measurements in the second row of strain gages (S4 through S6 in the left flange and S12 through S14 in the right flange). These measurements coincide with the observed local buckled shape and further highlight the effects of the global-local buckling interactions. Overall, the strain in the left and right flanges peaks at 3.6% (S5) and 5.5% (S10) during the 0.047 rad. cycle (target: +5%), respectively.

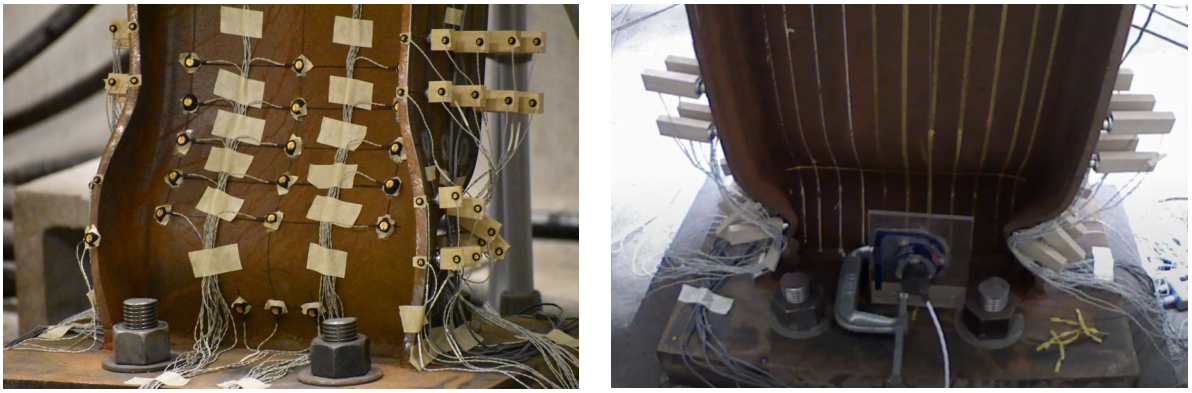

(a) (b)

Figure II.22. Specimen W2 column flange local buckling as seen from the (a) front and the (b) back of the column during the cycle to 4.70% drift (target: +5%).

The beams of specimen W2 experienced yielding based on the strain data, but no buckling was observed. The largest strain measured in the left beam was recorded during the first cycle to -0.028 rad. (target: -4%) at a value of 1.7%. The largest strain on the right beam was recorded during the first cycle to 0.029 rad. (target: +4%) at a value of 1.2%. With regards to the panel zone, shear strain yielding was measured by the strain gage rosettes (Fig. II.24b). Strains up to 4.3% in the top and bottom right corners of the panel zone (S2P & S4P) were observed. However, very little deformation of the panel zone was observed at the end of the test (Fig. II.24a) even though the shear strain values were higher than those measured in specimen W1

(Fig. II.15b). These results confirm that the panel zone design is adequate, and the excessive deformation observed in specimen W1 is due to other factors as explained in the previous section. By the end of the test of specimen W2, slight kinking was observed at the panel zone likely due to the specimen being pushed to 0.047 rad. (target: +5%), beyond what is expected from a SMF.

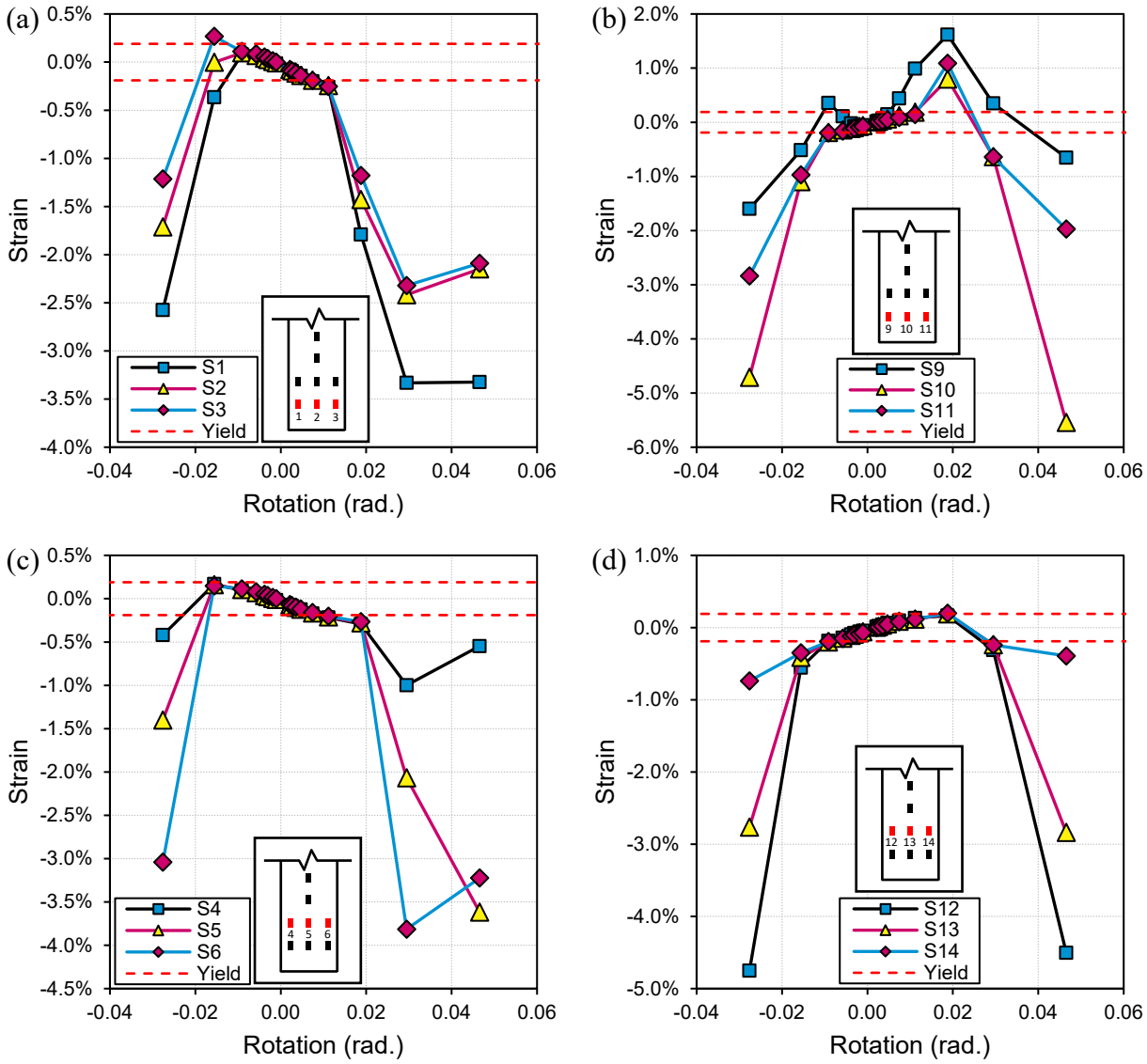

Figure II.23. Strain measurements during the first cycle to various drift magnitudes in the (a & c) left and (b & d) right flanges of specimen W2 along the (a & b) first and (c & d) second row of gages.

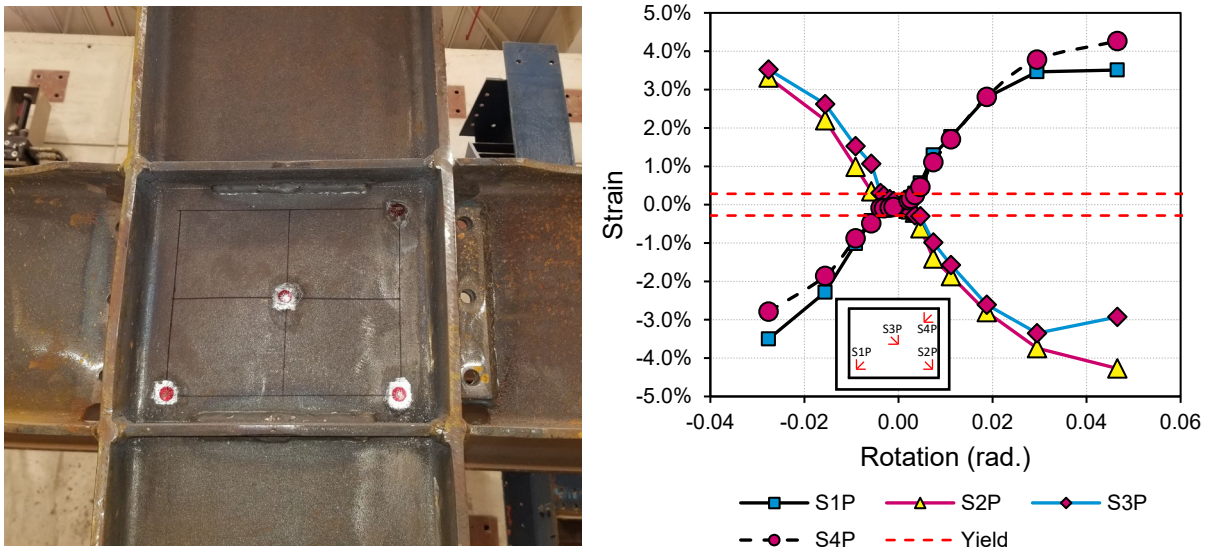

Figure II.24. (a) View of the panel zone of specimen W2 after the test and (b) the shear strain measurements from the attached strain gage rosettes. Data points taken at the first cycle to various drift magnitudes.

Specimen W3

The column in specimen W2 was not able to provide the ductility that is expected from a highly ductile column section under the symmetric cyclic loading protocol. However, it is worth investigating how the same column would fare under a different loading protocol to examine if the symmetric cyclic protocol is placing an unrealistically high demand on the column. To this end, Specimen W3 was subjected to the cyclic ratcheting loading protocol which was extended to a target drift level of 7%. The protocol was such that that the majority of the rotations were in the negative direction. The hysteretic behavior of the column is presented in Fig. II.25. The largest column rotations that were reached during testing were 0.011 rad. (target: +2%) and -0.059 rad. (target: -7%) for the positive and negative cycles, respectively. The maximum base moments recorded in the positive and negative cycles, respectively, are 202 kN-m (149 kip-ft) and -217 kN-m (160 kip-ft). The maximum positive moment matched the expected plastic

moment capacity of the column, 202 kN-m (149 kip-ft), and the maximum negative moment was 7.2% higher.

The column member reached its maximum moment capacity at a rotation of -0.023 rad. during the first cycle to -0.026 rad. (target: -4%). Local buckling in the column began during the first cycle to -0.031 rad. (target: -4.5%) in the right column flange given that a negative rotation value puts this flange in compression. The degree of local buckling is minimal with only an 8.7% degradation in moment capacity from the maximum moment observed. The deformation in the right column flange continues to increase and the column web begins to show signs of local buckling during the first cycle to -0.036 rad. (target: -5%). In the following cycles to -0.041 rad. (target: -5.5%) the moment capacity degradation reaches 15.2%, indicating that the column section is capable of meeting the high ductility performance criteria of maintaining at least 80% of its maximum moment capacity up to 4% drift when subjected to the cyclic ratcheting loading protocol. It is not until the first cycle to -0.053 rad. (target: -6.5%) that the moment capacity degradation surpasses this threshold and reaches 25.2% degradation. By the end of the test the column section had exhibited both global and local buckling (Fig. II.26) and the moment capacity degradation had reached 35.4% compared to its maximum overall moment capacity.

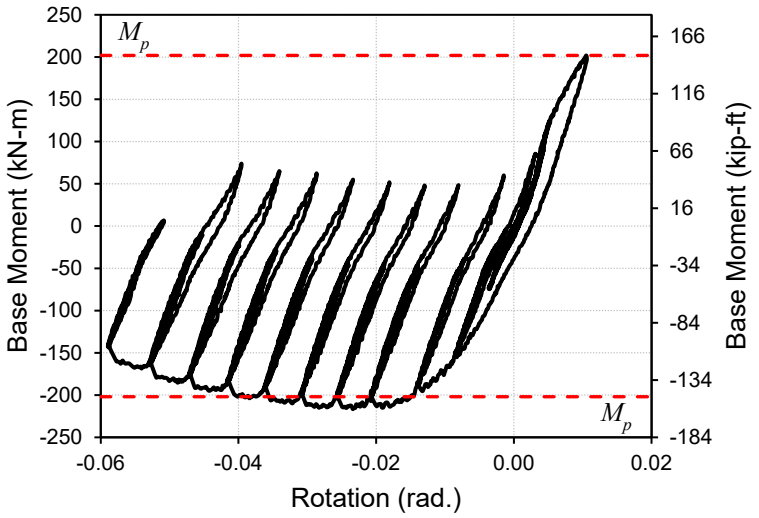

Figure II.25. Column base moment versus rotation behavior for specimen W3.

Measurements of the extent of global and local buckling during the test are shown in Fig. II.27 and Fig. II.28, respectively. The progression of global buckling was gradual as the maximum drift level increased. The amount of out-of-plane deformation by the end of the test peaked at 28 mm (1.1 in.) at a column height of 432 mm (17.0 in.). Near the column base, around 4.8 mm (0.19 in.) of local buckling was measured in the column web. With regards to the column flanges, these exhibited a different behavior compared with the other two specimens due to the cyclic ratcheting loading protocol. The direction in which the drift levels increased continuously kept the left flange in tension and the right flange in compression. The compression flange developed a sinusoidal buckled shape with different magnitudes of deformation between the front and back edges of the flange. The front edge deformation peaked at 5.9 mm (0.23 in.) at the end of the test (Fig. II.26c, measurements from only three of the markers are presented in some cases due to the fourth marker being blocked at higher drift levels). By contrast, the deformation at the back edge of the flange peaked at 17.5 mm (0.69 in.) at the end of the test (Fig. II.26d). In a similar manner to the buckling behavior observed in specimen W2, the buckled

shape and difference between the magnitudes of deformation at the front and back edge of the compression flange can be attributed to the interaction between the global and local buckling modes. The global buckling caused compression at the back edges of the column flanges, resulting in higher deformations in this location as the effects of the global and local buckling combined.

(a) (b)

Figure II.26. (a) Front and (b) side views of the specimen W3 column during the first cycle to -0.059 rad. (target: -7%).

The left flange when looking at the front of the column is always maintained in tension and therefore does not experience local buckling. Instead, the in-plane measurements of the front and back edges of the tension flange indicate signs of column twisting (Fig. II.28a & II.28b). Both the front and back edges experienced displacements in opposite directions relative to the flange centerline. The front edge displaced towards the column approximately 7.3 mm (0.29 in.) by the end of the test, while the back edge displaced approximately 8.0 mm (0.31 in.) away from the column. This behavior can be attributed to the asymmetry in the column's buckled shape that

results from the ratcheting loading protocol moving largely in a single direction. The combination of global and local buckling resulted in 3.6 mm (0.14 in.) of column axial shortening by the end of the test as shown in Fig. II.29.

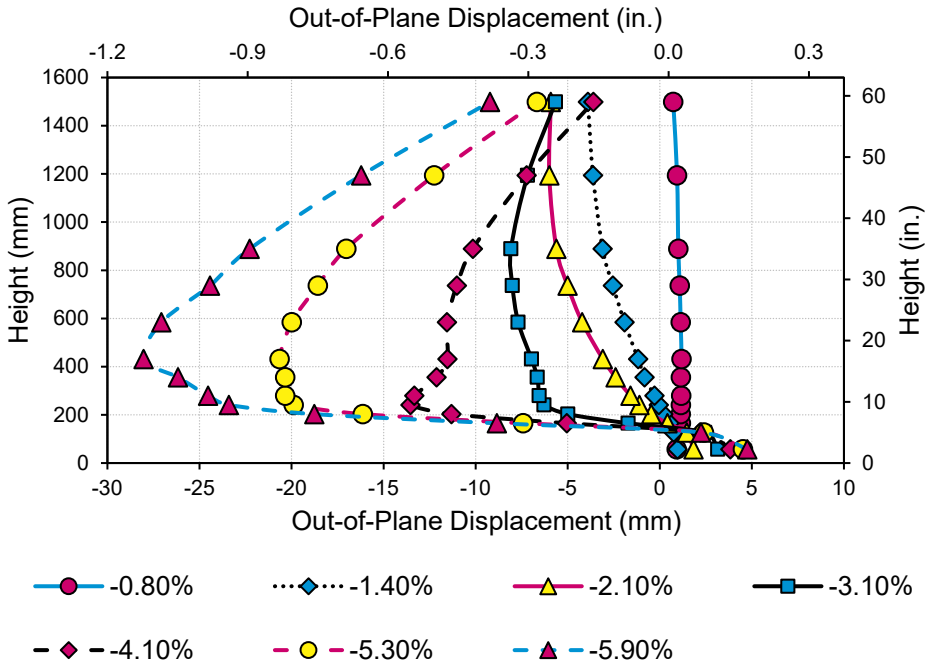

Figure II.27. Out-of-plane displacement of the column web centerline in specimen W3 during the first cycle to various drift magnitudes.

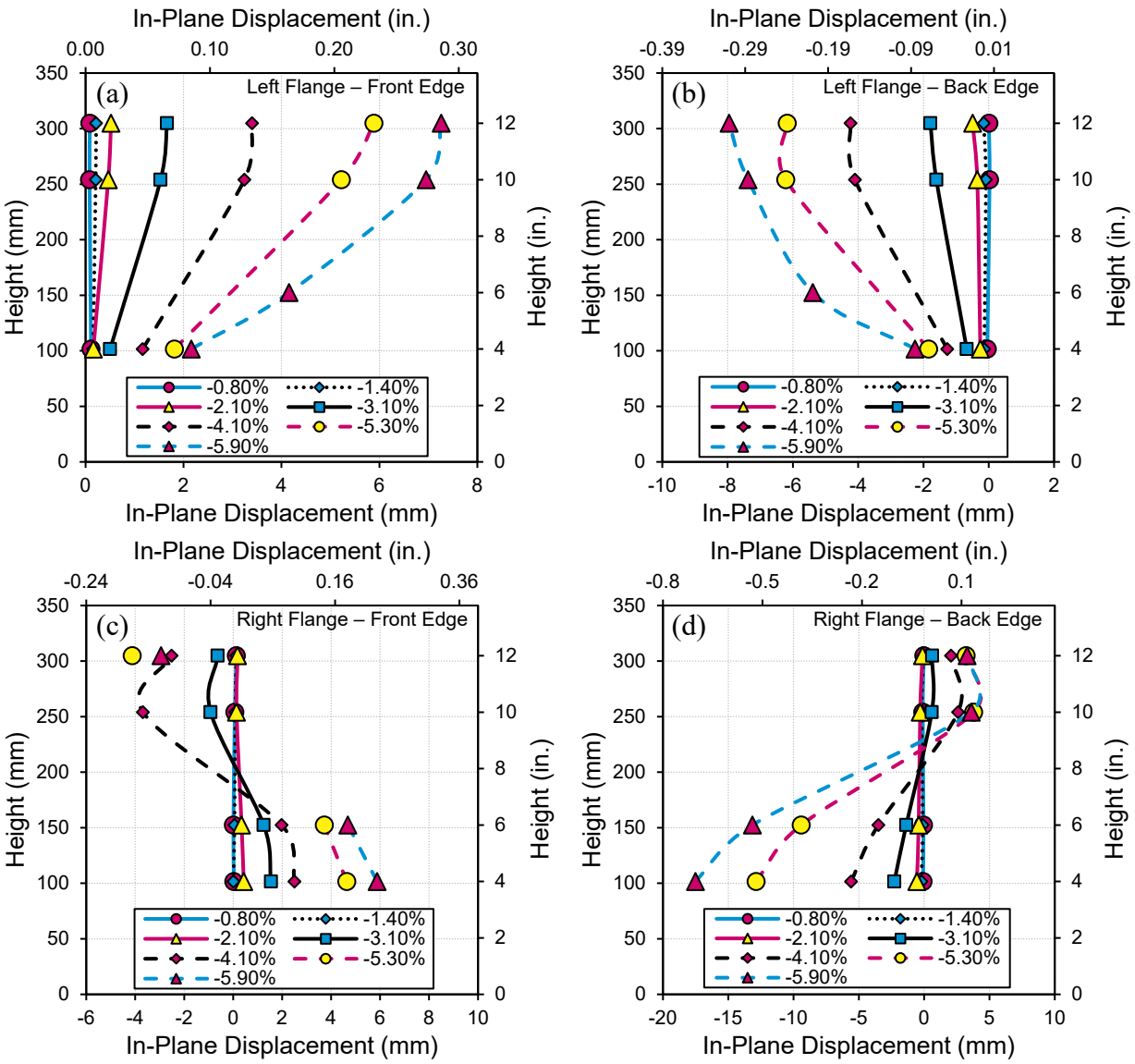

Figure II.28. In-plane displacement of the (a & c) front and (b & d) back edges of the (a & b) tension and (c & d) compression column flange of specimen W3 during the first cycle to various drift magnitudes.

Strain measurements along the column flanges are presented in Fig. II.30. Due to the local buckling associated with specimen W3, the compression column flange experienced significantly higher strains when compared to the tension flange. The strain in the tension flange peaked at 2.3% (S3) during the first cycle to -0.059 rad. (target: -7%) while the strain in the compression flange peaked at -4.7% (S11) during the first cycle to -0.053 rad. (target: -6.5%). Further, all of

the strain gages placed on the compression flange recorded strains above yield, while on the tension flange the two strain gages placed along the centerline farthest from the column base and gage S6, located on the right edge off the second row (Fig. II.30c), did not measure strains higher than yield. These results show that when subjected to a collapse-consistent progression of drifts in the form of the cyclic ratcheting protocol, the column is still placed under significantly less demands even at higher drift levels than the symmetric cyclic loading protocol. With regards to the beam members, the strain gages confirmed yielding occurred in the beams, but there were no signs of local buckling in the plastic hinge region. The strains in the left and right beams peaked at 2.9% and -1.3%, respectively, during the first cycle to -0.059 rad. (target: -7%).

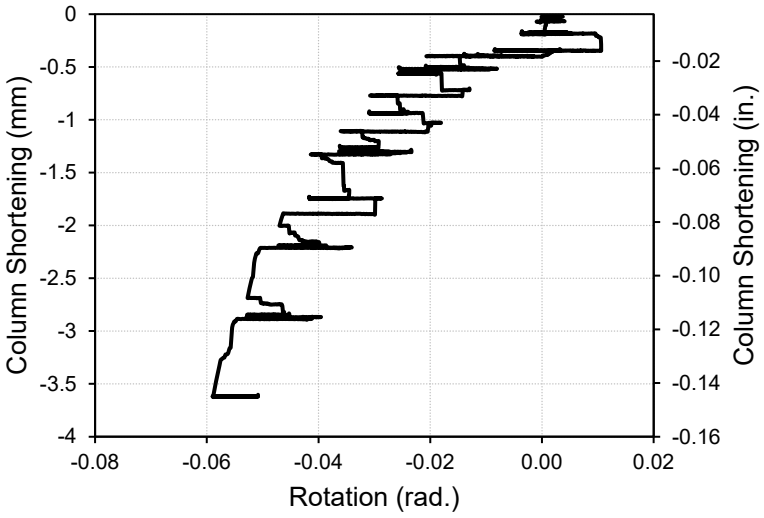

Figure II.29. Column axial shortening with respect to actual rotation measured during the test for specimen W3.

A picture of the beam-to-column connection taken at the end of the test and the shear strain measurements in the panel zone are presented in Fig. II.31. From these measurements, it is observed that the panel zone experienced high shear strains with values up to 7.3% during the first cycle to -0.059 rad. (target: -7%). Although the shear strain was high, there were no signs of buckling in the panel zone at the end of the test (Fig. II.25a). Nonetheless, the high drifts

imposed on the specimen resulted in the formation of a kink in the column just outside of the beam-to-column connection region.

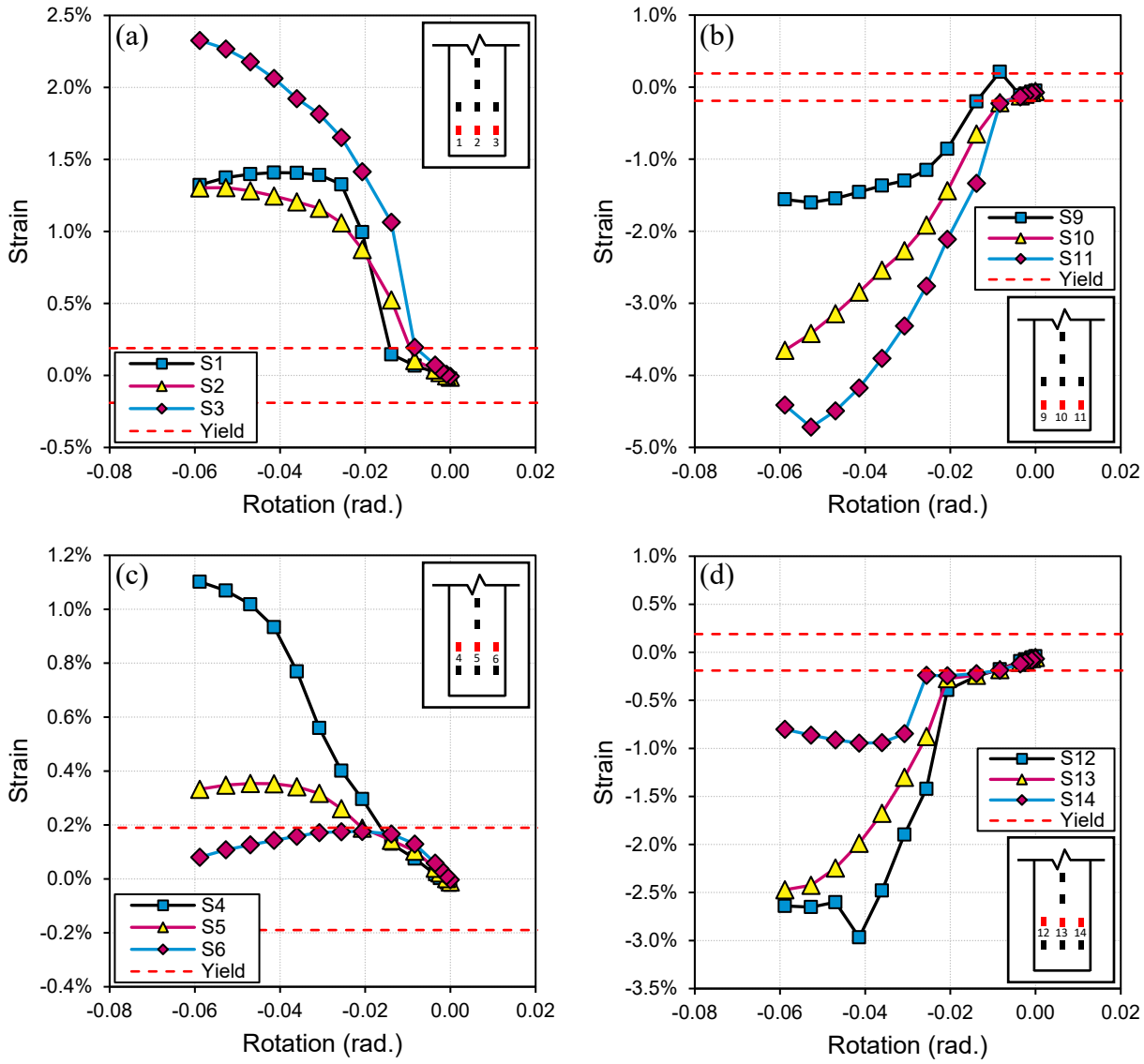

Figure II.30. Strain measurements during the first cycle to various drift magnitudes in the (a & c) left and (b & d) right flanges of specimen W3 along the (a & b) first and (c & d) second row of gages.

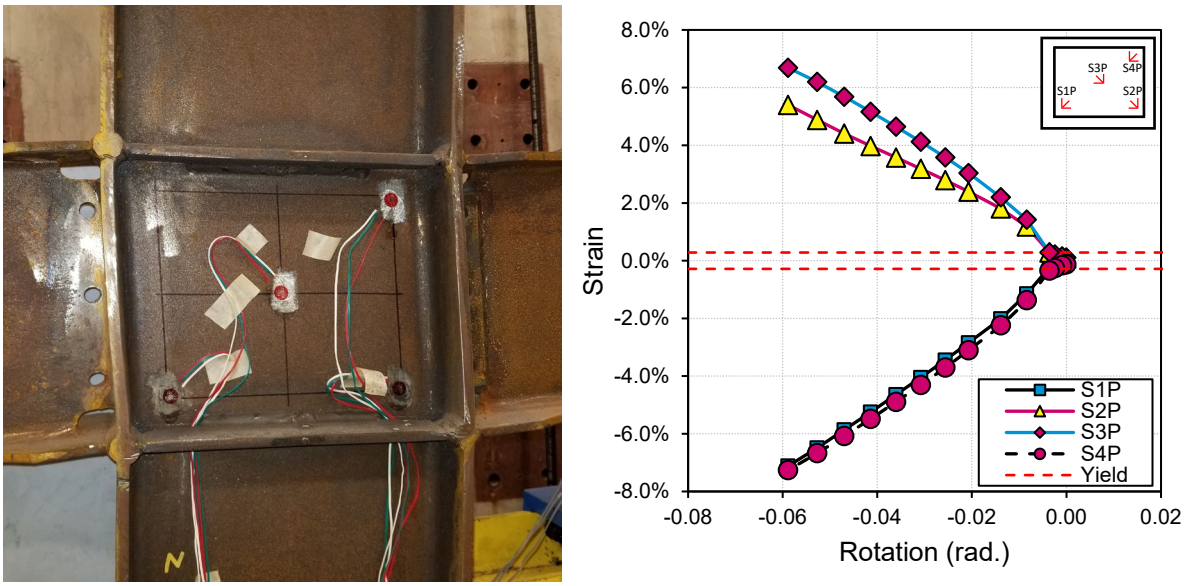

(a) (b)

Figure II.31. (a) View of the panel zone of specimen W3 after the test and (b) the shear strain measurements from the attached strain gage rosettes.

Influence of the Loading Protocols

The only difference between specimen W2 and W3 was the lateral loading protocol that was applied. Specimen W2 underwent the symmetric cyclic loading protocol, while specimen W3 underwent the cyclic ratcheting loading protocol (Fig. II.4). Comparing the results between these two tests provides some insight into the influence of the loading protocols on the cyclic performance of the cruciform specimens and the deep, slender wide flange columns that were a part of them. The largest column rotations that were reached by specimens W2 and W3 were 0.047 rad. (target: +5%) and -0.059 rad. (target: -7%), respectively. Even though specimen W3 was subjected to drifts 25.5% larger than specimen W2, specimen W3 exhibited a better cyclic performance relative to specimen W2. The column in specimen W3 experienced a smaller magnitude of both global and local buckling compared to specimen W2 (Fig. II.18 & II.22 & II.26). This resulted in an influence on the observed moment capacity degradation of each

specimen. While the column section satisfies the local slenderness requirements to be classified as a high ductility section, only specimen W3 meets what is typically considered the high ductility performance criteria of maintaining at least 80% of its maximum moment capacity at 4% drift. The moment capacity of the column in specimen W2 had degraded by 20% at a rotation of -0.028 rad. (target: -4%). By contrast, the moment capacity degradation of the column in specimen W3 had reached only 15.2% by the first cycles to -0.041 rad. (target: -5.5%) and did not surpass 20% (25.2%) until the first cycle to -0.053 rad. (target: -6.5%). It is clear that the cyclic ratcheting loading protocol placed less demand on the column member as it primarily causes compression in only one of the flanges instead of both as is the case with the symmetric cyclic protocol. While employing the symmetric cyclic protocol may be a more conservative approach, it is important to note that the ratcheting protocol represents a realistic drift progression that is consistent with that experienced by a typical column in a collapsing structural system due to a seismic event (Wu et al. 2018a). These results highlight the importance of considering different loading protocols when evaluating the seismic performance of column members as some protocols could be overly demanding leading to overly conservative recommendations.

Conclusions

A computational and experimental investigation was undertaken to evaluate the seismic performance of deep, slender wide flange column subassemblies. All of the members in these subassemblies met the local slenderness criteria for SMF. In the initial finite element study four full-scale cruciform subassemblies were analyzed under a variety of axial loads and lateral loading protocols. Three of these subassemblies featured three different size wide flange columns connected to wide flange beams while the fourth featured an HSS column with a similar

strength to a wide flange column in one of the subassemblies. Two of the wide flange columns represented the design approach of utilizing deep, slender wide flange column sections to meet current seismic design requirements, while the third was a much stockier section that represented a pre-Northridge wide flange column. The constant axial load applied during these analyses varied from 20% to 40% of the column's axial yield strength and both a symmetric cyclic (SC) and cyclic ratcheting (CR) lateral loading protocol were considered. The experimental tests featured a half-scale version of one of the computationally tested wide flange subassemblies. Three identical cruciform specimens were tested under both loading protocols used in the computational study with a constant axial load equivalent to 20% of the column's axial yield strength. The results and observations from these tests are summarized in the following:

1. Different levels of axial load on the column in the computational study had a significant effect on the cyclic performance of each subassembly in terms of its maximum moment capacity, moment capacity degradation, and overall stability. In terms of maximum moment capacity, the HSS subassembly (SA1) was affected the least in comparison to the other three wide flange subassemblies as the axial load increased. Relative to their respective maximum moment capacities with an axial load ratio of 20%, the HSS subassembly (SA1) saw a reduction in maximum moment capacity of 18.2% once the axial load ratio was increased to 40%. By comparison, all of the wide flange subassemblies exhibited a reduction upwards of 20.9%. With regards to moment capacity degradation, when subjected to the SC loading protocol, the pre-Northridge column in subassembly SA2, at an axial load ratio of 30% or lower, was the only specimen that met the high ductility performance criteria of maintaining 80% of its maximum moment capacity by 4% drift. These results showcase how some deep, slender wide flange

columns can fail to meet the high ductility performance criteria while being classified as highly ductile sections due to their geometric properties.

2. The lateral loading protocol can significantly affect the behavior of a column under large axial loads and bending moments. An SC protocol, like the one prescribed by AISC for prequalification of seismic moment connection, that consists of a progression of fully reversed drifts versus a CR protocol that was developed to represent a realistic progression of drifts that a column experiences during a structural collapse results very different demands placed on the column. The CR protocol starts with fully reversed cycles and transitions into a ratcheting behavior in which the column continually drifts further to one side. This progression resulted in significant less demands being placed on the column compared to the SC protocol since the CR protocol only puts one of the column flanges in compression, limiting the amount of local buckling seen in the column cross-section. This difference in behavior was clearly observed when comparing the cyclic performance of the experimentally tested W2 and W3 specimens. Specimen W2 was tested under the SC protocol and was not able to meet the high ductility performance requirements, exhibiting 20% moment capacity degradation at a rotation of 0.028 rad. By contrast, specimen W3 was subjected to the CR protocol and was able to meet the high ductility criteria, only showing 15.2% degradation in moment capacity at a rotation of 0.041 rad. These results suggested that while employing the SC protocol may be a conservative approach, it is important to also consider other loading protocols which may be more realistic.
3. The buckling behavior observed in the experimentally tested specimens W2 and W3 indicated interaction between the global and local buckling modes of the column. In the

case of specimen W2 (SC), the global buckled shape curved towards the back edge of the column flanges. This buckled shape resulted in an increase in the degree of flange local buckling at the back of the column relative to the buckling observed at the front edge of the column flanges. A similar behavior was observed in specimen W3 even though the degree of global and local buckling was smaller. The direction of the CR protocol kept the right column flange of specimen W3 in compression throughout the test while the left flange was always in tension. For this reason, flange local buckling only occurred in the right column flange. The global buckled shape of specimen W3 also curved towards the back edges, which resulted in higher deformation towards the back edge of the right column flange. The asymmetry of the buckling shape due to the loading protocol also led to some observed twisting of the column. With the current design standards, the propensity for global and local instabilities is evaluated separately according to a column's geometry. The results presented herein suggest there is a need to consider how the local and global instabilities interact with each other, particularly when considering deep, slender wide flange columns, as these interactions have the potential to significantly affect the expected seismic performance of a column section. Similar results are typically not seen in more stocky columns which tend to have smaller element slenderness ratios due to their thick flanges and webs.

CHAPTER III

Improving the Cyclic Performance of HSS Beams by Incorporating a Lightweight Foam-Fill

Introduction

Seismic design requirements for steel moment resisting frames (SMRFs) in the U.S. rely on the frame's beams and the base of the first story columns to form plastic hinges as the primary energy dissipating mechanism against seismic input energy. The formation of these plastic hinges in specific locations, such as the column base and beam ends, allows the SMRF to remain stable under large events. To achieve this controlled failure mechanism, it is important for the structural members to maintain a consistent load-carrying capacity at large story drifts. This requirement can be met by preventing or mitigating the effects of local buckling in the plastic hinge regions. Traditionally, this requirement is met by selecting structural members that meet the limiting local slenderness ratios established by the American Institute of Steel Construction (AISC) Seismic Provisions (2016a) for special (SMFs), intermediate (IMFs) and ordinary moment frames (OMFs). In the case of beam members, these limits ensure that at least 80% of the beam's plastic moment capacity is maintained at story drift angles of 0.02 rad. and 0.04 rad. for IMFs and SMFs, respectively.

Although hollow structural sections (HSS) and concrete-filled tubes (CFTs) are commonly used as column and beam-column members in seismic frame structures (Hajjar 2000), they have not seen a similar adoption rate for use as beam members. Only recently has the performance of

HSS beam members been shown to be adequate for use in SMRFs while undergoing seismic loads (Fadden and McCormick 2012, Fadden and McCormick 2014a, Fadden et al. 2015). Despite being shown as viable, the use of HSS beams in SMRF can be further hindered by stringent local slenderness requirements, which limit the number of section sizes available for use in IMFs and SMFs. Addressing these shortcomings will allow structural engineers and architects to further take advantage of the beneficial properties of HSS, such as excellent torsion resistance, good bending strength, and pleasing aesthetics. In a similar way to CFTs used as columns, one way of improving the performance of HSS beams is by filling them to provide support for the inherently flexible walls of the HSS member and potentially further increasing energy dissipation capacity at large rotation levels. Prion and Boehme (1994) conducted pure bending tests on five concrete-filled circular HSS (4 monotonic, 1 cyclic loading) and found that they all failed in a very ductile manner. In the case of the cyclic test, the section exhibited a significant amount of energy dissipation and only slight moment capacity degradation with subsequent loading cycles. Lu and Kennedy (1994) tested four rectangular and square HSS and twelve concrete-filled HSS under pure monotonic bending and found that the ultimate flexural strength of the section increased by 10 to 30% when filled. Elchalakani et al. (2001) conducted an experimental investigation of the flexural behavior of circular CFTs and found the concrete-fill completely prevents local buckling at very large rotations for sections with a depth-to-thickness ratio of $d/t \leq 40$. At higher slenderness ratios ($74 < d/t \leq 110$) multiple ripples are formed in the inelastic range, resulting in increased ductility when compared to an empty section. More recent investigations summarize the basis of the current design equations for CFTs and confirm these equations provide conservative results compared to experimental data (Lai et al. 2014, Lai and Varma 2015).

While past studies suggest that concrete-fill can improve the performance of HSS beams, the use of concrete as fill has some potential drawbacks, including an increase in flexural strength and stiffness that needs to be considered during design to ensure connecting elements can withstand the higher loads. This situation is of particular concern when looking to retrofit an HSS member with fill material. Concrete-fill also will increase the seismic mass of the structure, resulting in an overall increase in the expected loads that the structure experiences during a seismic event. Ideally the fill material is lightweight, while still providing sizable improvements in the performance of the member. Other industries have shown the benefits of considering lightweight, high energy dissipation materials for fill applications. For example, in the automotive industry Zhou et al. (2016) investigated the benefits of a polyurethane foam-fill in AZ31B magnesium beams and DC04 steel beams. The results suggested that the foam-fill stabilizes the deformation of the tube walls, which in turn improves the beam's energy absorption capacity significantly.

To expand the potential use of HSS in seismic moment frame systems, this study quantifies the benefits of using a polyurethane foam fill in conjunction with HSS beams. Seven pairs of empty and polyurethane foam-filled HSS beams are tested under fully reversed cyclic loading to explore the effects of the fill material across a variety of local slenderness ratios. The foam's capability to mitigate the effects of local buckling is examined with regards to changes in the moment capacity degradation with continued cycling, rotation level at fracture, ability to meet the intermediate and special moment frame requirements and energy dissipation capacity.

Study on Polyurethane Foam

Description of foam material

The fill material used in this study is a two-part liquid, expanding rigid urethane closed-cell foam manufactured by US Composites. It is designed to be poured in place, allowing the foam to easily fill the void of an HSS. The procedure to make the foam involves combining equal parts of both liquid components and mixing them together in a uniform manner. The selection of the fill material was informed by three-point and four-point bending tests conducted by Wei (2017). This investigation showed that the 256 kg/m^3 (16 lb/ft^3) density foam – the urethane foam with the largest density available from US Composites – performed better than lower density foams and urethane rubber in terms of mitigating the effects of local buckling on an HSS beam. Visual inspection of the foam once testing concluded revealed that the foam acts primarily in compression as the foam does not form a strong bond to the inner walls of the HSS and separates easily. For this reason, this paper only presents a discussion of the foam's mechanical properties while under compression. For a discussion on the foam's behavior under tensile load, see Ammons et al. (2021).

Mechanical properties

Further testing was conducted on the urethane foam to characterize its mechanical properties and understand its role in improving the cyclic behavior of HSS beams. Multiple 38.1 mm (1.5 in.) foam cubes were tested under monotonic and cyclic compression (Fig. III.1) at loading rates of 0.254, 2.54, and 25.4 mm/s (0.01, 0.1, 1.0 in./s). The foam's general behavior under compression includes an initial elastic region that promptly plateaus as it crushes, followed by a sharp increase in strength due to consolidation. Results from these tests suggest that there is only a relatively minor loading rate effect on the compressive yield strength and consolidation region,

while having no effect on the elastic modulus (for a more in-depth discussion on the effects of the loading rate see Wei et. al. 2016). A more significant difference in mechanical properties is observed when comparing different pours or batches of the foam. As an example, while undergoing cyclic loading (Fig. III.1b) the second set of foam cubes (Group 2) only exhibited 42.5% and 38.8% of the strength of Group 1 during the first cycles to 20% and 40% strain, respectively. These large differences suggest the need for a standardized mixing procedure so that adequate material strength is ensured when the foam is used in structural applications.

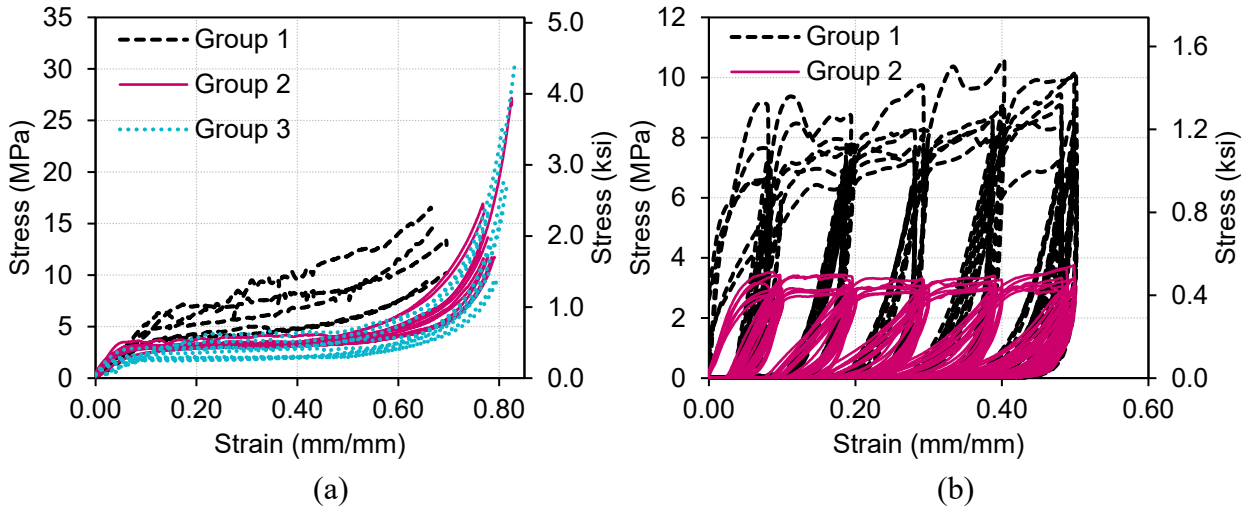

Figure III.1. Compression stress-strain behavior of urethane foam under (a) monotonic and (b) cyclic loading. Groups represent separate batches of foam. Loading rate: 2.54 mm/s (0.1 in./s).

While a lower compressive strength can reduce the effectiveness of the foam fill, its general behavior under cyclic loading indicates it can provide support to an HSS beam even at high levels of deformation. When the foam is initially compressed to a certain point, it crushes, dissipating energy (Fig. III.2a). A repeat cycle at the same strain level results in considerably less energy being dissipated (Fig. III.2b), but if the strain is increased the foam continues to crush and consolidate, further dissipating energy. This result suggests that the foam will have its maximum effect the first time it is deformed to a certain strain, but will continue to provide some support to

the walls of the HSS and add energy dissipation capacity as the beam undergoes larger rotations. As experimental testing shows, this behavior results in the foam managing to delay the onset of local buckling and its presence reduces the severity of, or completely prevents, fracture of the HSS walls.

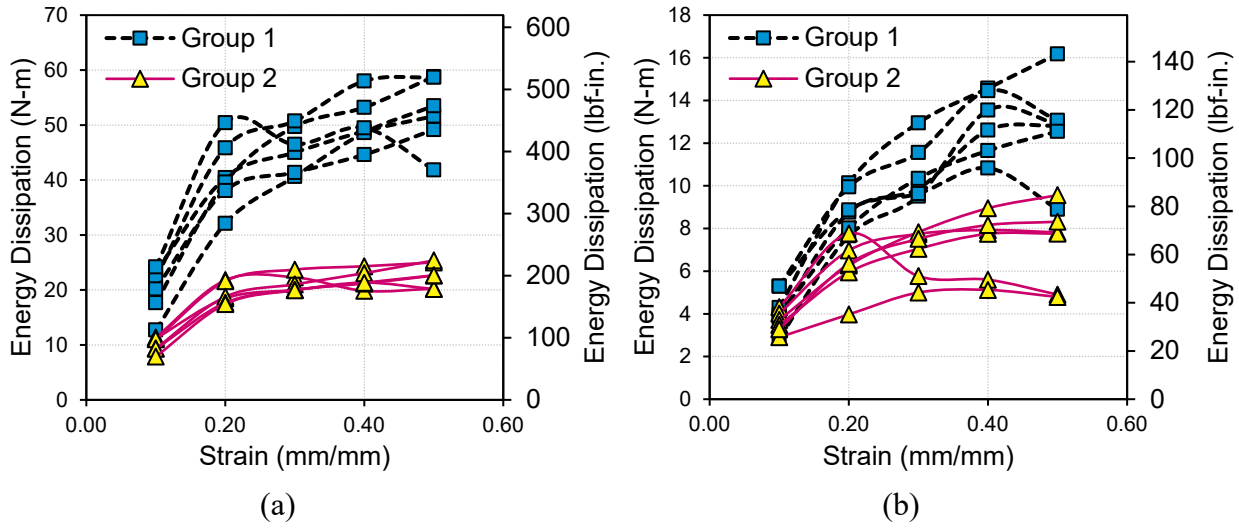

Figure III.2. Energy Dissipation at the (a) first and (b) second cycle of each strain increment. Groups represent separate batches of foam. Loading rate: 2.54 mm/s (0.1 in./s).

Test Setup and Methodology

Description of setup

The test setup for the empty and foam-filled specimens consists of a 1.54 m (59 in.) long cantilever beam member oriented vertically (Fig. III.3a). Cyclic displacements are applied to the free end at the top of the HSS through a slotted hole pin connection using a hydraulic actuator. This type of connection prevents the application of an axial load and moment at the free end of the HSS beam. The applied loading protocol follows the one prescribed by the AISC Seismic Provisions (2016a) for prequalifying beam-to-column moment connections. This protocol incorporates a progression of fully reversed cyclic displacements that correspond to story drift ratios from 0.375% to 8% (Fig. III.3b). Although 8% story drift is larger than what is typically

expected during an earthquake, it is necessary to reach this drift level to assess the effectiveness of the foam-fill in delaying and mitigating fracture, which typically occurs at or above 7% drift. In the case of the foam-filled beam specimens, they are filled with the polyurethane foam up to 1.5 times the beam's theoretical plastic hinge length, which was calculated using Eq. III.1, where S_x is the elastic section modulus around the strong axis, Z_x is the plastic section modulus around the strong axis, and L is the distance between the beam's fixed end and the location of the applied point load. This approach ensures that the foam is present in any region that might experience yielding during testing.

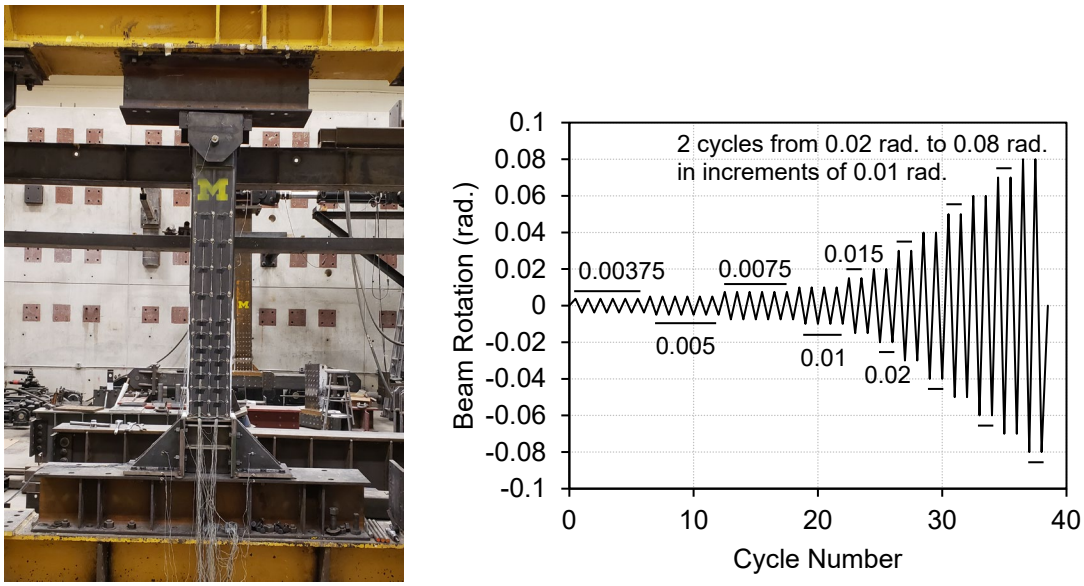

(a) (b)

Figure III.3. (a) Picture of cantilever beam specimen test setup. (b) AISC loading protocol for prequalifying beam-to-column moment connections used for the cantilever tests.

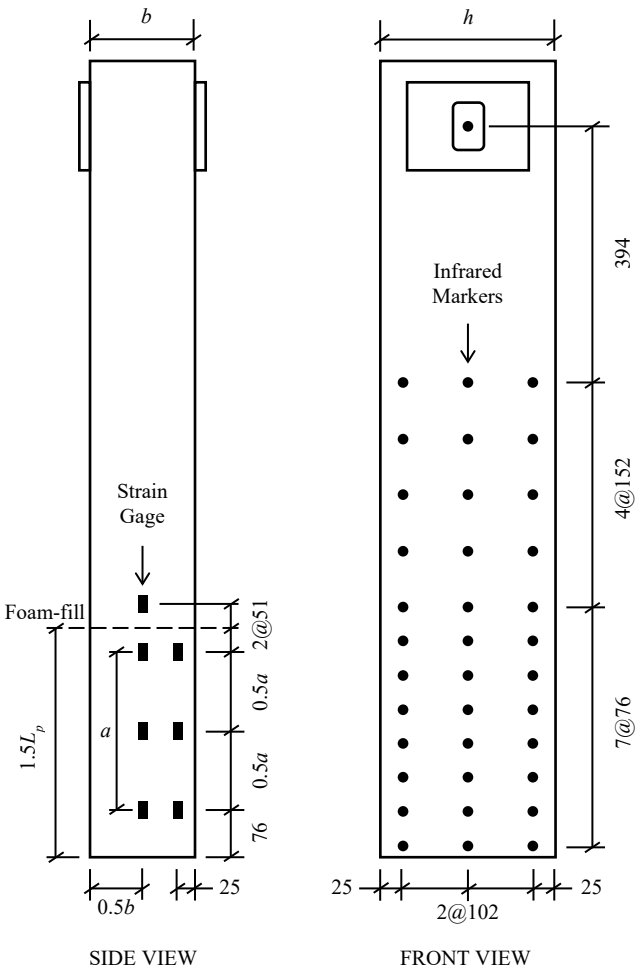

Figure III.4. Instrumentation diagram for the tested beam sections. All units in mm.

Every test specimen is instrumented with strain gages and a grid of infrared markers (Fig. III.4). The strain gages are placed on one of the beam flanges at multiple positions above and below where the foam-fill ends. The grid of infrared markers is placed on one side of the beam web and is used to track the movement of the beam and to measure any rigid body rotation that occurs during testing. The beam rotation data is adjusted using these measurements to obtain the effective/actual rotation of the specimen. A thin layer of whitewash also is applied in the plastic hinge region of the beam flanges and opposite on the web opposite the infrared makers to serve

as a visual indicator of inelastic behavior when the mill scale flakes off due to the progression of yielding.

$$L_p = \left(1 - \frac{S_x}{Z_x}\right) L \qquad \text{(Eq. III.1)}$$

Selected beam sections

Seven pairs of empty and foam-filled HSS beam sections (ASTM A500 Gr. B steel) are selected based on their local slenderness ratios to represent different degrees of seismic performance. The expected cyclic behavior is determined by a member ductility rating in the AISC Seismic Provisions (2016a). The included sections range from comfortably meeting the highly ductile criteria to others that do not meet the moderately ductile criteria. The latter are expected to perform poorly under cyclic loading and are denoted as having a "Low" ductility rating in Table III.1. The ductility criteria for both highly and moderately ductile sections is calculated using Eq. III.2 and III.3, respectively, where E is the elastic section modulus, F_y is the minimum yield stress, and R_y is the ratio of the expected yield stress to the minimum yield stress.

Table III.1. Measured properties of experimentally tested sections (metric).

Section ID	HSS Section	Avg. E [GPa]	Avg. F_y [MPa]	Avg. ε_y [%]	Z_x [$\times 10^3$ mm^3]	b/t	h/t	Ductility
H1	203.2×101.6×6.4	185	379	0.205	216	12.7	30.0	High
H2	203.2×101.6×9.5	184	381	0.207	305	7.0	18.6	High
M1	203.2×152.4×6.4	184	355	0.193	272	21.1	29.2	Moderate
L1	203.2×203.2×6.4	186	370	0.199	331	30.8	29.9	Low
H3	254×101.6×6.4	205	398	0.196	315	13.0	38.5	High
M2	254×152.4×6.4	195	388	0.199	380	21.7	39.2	Moderate
L2	254×203.2×6.4	192	355	0.186	454	29.5	37.7	Low

Table III.1a. Measured properties of experimentally tested sections (US customary units).

Section ID	HSS Section	Avg. E [ksi]	Avg. F_y [ksi]	Avg. ε_y [%]	Z_x [in^3]	b/t	h/t	Ductility
H1	8×4×1/4	26829	55.0	0.205	13.2	12.7	30.0	High
H2	8×4×3/8	26711	55.2	0.207	18.6	7.0	18.6	High
M1	8×6×1/4	26747	51.5	0.193	16.6	21.1	29.2	Moderate
L1	8×8×1/4	26993	53.7	0.199	20.2	30.8	29.9	Low
H3	10×4×1/4	29708	57.8	0.196	19.2	13.0	38.5	High
M2	10×6×1/4	28325	56.3	0.199	23.2	21.7	39.2	Moderate
L2	10×8×1/4	27867	51.5	0.186	27.7	29.5	37.7	Low

Measurements of the material and geometric properties of each section are also provided in Table III.1. The material properties are the average values obtained from testing at least three tensile coupon specimens cut from the flat portion of each HSS section. The plastic section modulus is calculated based on the procedure outlined by Sedlacek et. al (1998). The measured properties exhibit some significant differences that affect the ductility rating of two sections when compared to their nominal or expected values. On average, every section except section H3 has an elastic modulus that is 6.1% lower than the nominal value of 200 GPa (29,000 ksi). In terms of the yield stress, the measured value is compared to the expected yield stress value, R_yF_y, which is 444 MPa (64.4 ksi) for ASTM A500 Gr. B steel. The measured yield stress is used in place of R_yF_y when calculating the ductility criteria for each section. Compared to the expected yield stress, every section exhibits a lower value, on average, by 15.5%. There are similar differences in the geometric properties. The measured plastic section moduli, b/t ratios, and h/t ratios are lower than nominal values on average by 1%, 8%, and 4.7%, respectively.

$$\left(\frac{b}{t}\right)_{hd} = 0.65\sqrt{\frac{E}{R_yF_y}} \quad \text{(Eq. III.2)}$$

$$\left(\frac{b}{t}\right)_{md} = 1.18\sqrt{\frac{E}{R_yF_y}} \quad \text{(Eq. III.3)}$$

These differences in material and geometric properties result in sections H1 and H3 meeting the highly ductile criteria, whereas they would not if nominal values are used in determining their ductility rating. Sections that meet the highly ductile criteria are expected to perform well under cyclic loading and therefore not exhibit many benefits when filled with the polyurethane foam. Although sections H1 and H3 meet the highly ductile criteria, their b/t ratios are still close to the highly ductile limit, while also having higher h/t ratios than section H2. For that reason, these sections are expected to show more performance improvements compared to section H2 when filled with the polyurethane foam. In general, data from sections H1 and H3 provides insight into the benefits of incorporating a polyurethane foam fill in HSS sections whose b/t ratios just meet the highly ductile criteria.

Every pair of empty and foam-filled beams was cut from the same batch of steel except for sections M1 and L1. The properties presented in Table III.1 for these two sections correspond to the foam-filled steel beam. The properties and test results of the empty section were obtained from a previous study conducted by Fadden and McCormick (2012) and Fadden (2013). Comparing the material properties of these two different batches of steel shows that the empty HSS sections had a yield stress 3.9% and 18.5% higher than their foam-filled version for sections M1 and L1, respectively. This difference affects the maximum moment capacity of these sections and is an important detail in understanding the role of the foam as a fill material.

Test Results

Effect on maximum moment capacity

The foam-fill plays a supportive role to the beam, providing stability to the HSS walls and additional energy dissipation capacity that can mitigate the effects of local buckling. For that reason, the beam can exhibit improved cyclic behavior that is no longer hindered to the same

degree by local instabilities. These improvements have an upper limit determined by the behavior of the HSS if local buckling did not occur, which would allow a plastic hinge to form without degradation in capacity. The foam-fill does not significantly improve behavior beyond this point as its material strength is comparatively too low to make a compelling difference in the beam's maximum moment capacity. Table III.2 helps illustrate this point. "Nominal" refers to the moment capacity calculated with the expected strength, R_yF_y, and nominal plastic section modulus, Z_x. "Measured" is calculated with the values in Table III.1. "Test" is the maximum moment capacity obtained from the experimental test. The upper limit that is discussed can be best observed in section H2. This section is well under the highly ductile limit and never shows signs of buckling or degradation throughout the test, in both the empty and foam-filled beams. In the case of section H2, there are no benefits to incorporating the foam-fill. Sections M1 and L1 show a decrease in maximum moment capacity (1.8% and 10.3%, respectively), but this is due to the differences in yield strength between the empty and filled HSS beams, as discussed previously. Section L2 is the only section to exhibit a significant increase (10.1%) in moment capacity when filled with the foam. The reason for this being that the polyurethane foam fill was able to delay the onset of local buckling by an entire cycle magnitude. Buckling starts when the drift first reaches 2.4% and 3.1% for the empty and filled beam, respectively. While the foam fill can help a section reach a higher moment capacity by delaying local buckling, its benefits are more readily apparent after the maximum moment capacity is reached.

Table III.2. M_p values for beam sections obtained from nominal properties, measured properties, and the test results.

Section ID	Empty [kN-m | kip-ft]			Foam-Filled [kN-m | kip-ft]	
	Nominal	Measured	Test	Test	Test Difference
H1	96.8 | 71.4	82.0 | 60.5	98.2 | 72.4	99.7 | 73.5	+1.5%
H2	137 | 101	116 | 85.6	139 | 103	140 | 103	+0.3%
M1	123 | 90.7	96.6 | 71.2	115 | 84.8	113 | 83.3	-1.8%
L1	149 | 110	123 | 90.7	143 | 106	129 | 95.1	-10.3%
H3	138 | 102	125 | 92.2	145 | 107	148 | 109	+2.1%
M2	172 | 127	148 | 109	170 | 125	174 | 128	+2.5%
L2	204 | 151	161 | 119	174 | 128	192 | 142	+10.1%

Improvements to beam behavior

Incorporating a foam-fill does not significantly affect the elastic behavior of the beam sections. It is not until the walls of the HSS begin to buckle that the foam-fill starts to influence the overall behavior of the section. While the degree of effectiveness of the foam-fill varies depending on the local slenderness ratios of each section, every section except H2 exhibits benefits from incorporating the foam-fill. Generally, the foam-fill helps mitigate the moment capacity degradation that occurs as a consequence of local buckling (Fig. III.5), and in some cases manages to delay its onset. This behavior results in a lower degree of deformation of the HSS walls when compared to an empty section, which in turn leads to a less severe fracture (Fig. III.6), and in some cases outright prevents it. Various points of interest during testing are shown in Table III.3 for every section. These include the rotation cycle at which buckling and striation start to occur, as well as the capacity degradation the first time 4% drift is reached. Moment capacity degradation is calculated after the maximum moment capacity is reached by comparing it to the moment capacity at another point in time. The degradation difference column shows the change in moment capacity degradation at 4% drift when incorporating the foam-fill. This metric is important because it determines whether a beam section can be used in an SMF or IMF. For

SMFs, the Seismic Provisions (2016a) require the beam to be able to accommodate a story drift angle of at least 0.04 rad. while maintaining 80% of its plastic moment capacity. For IMFs, a similar requirement applies, but at 0.02 rad. instead.

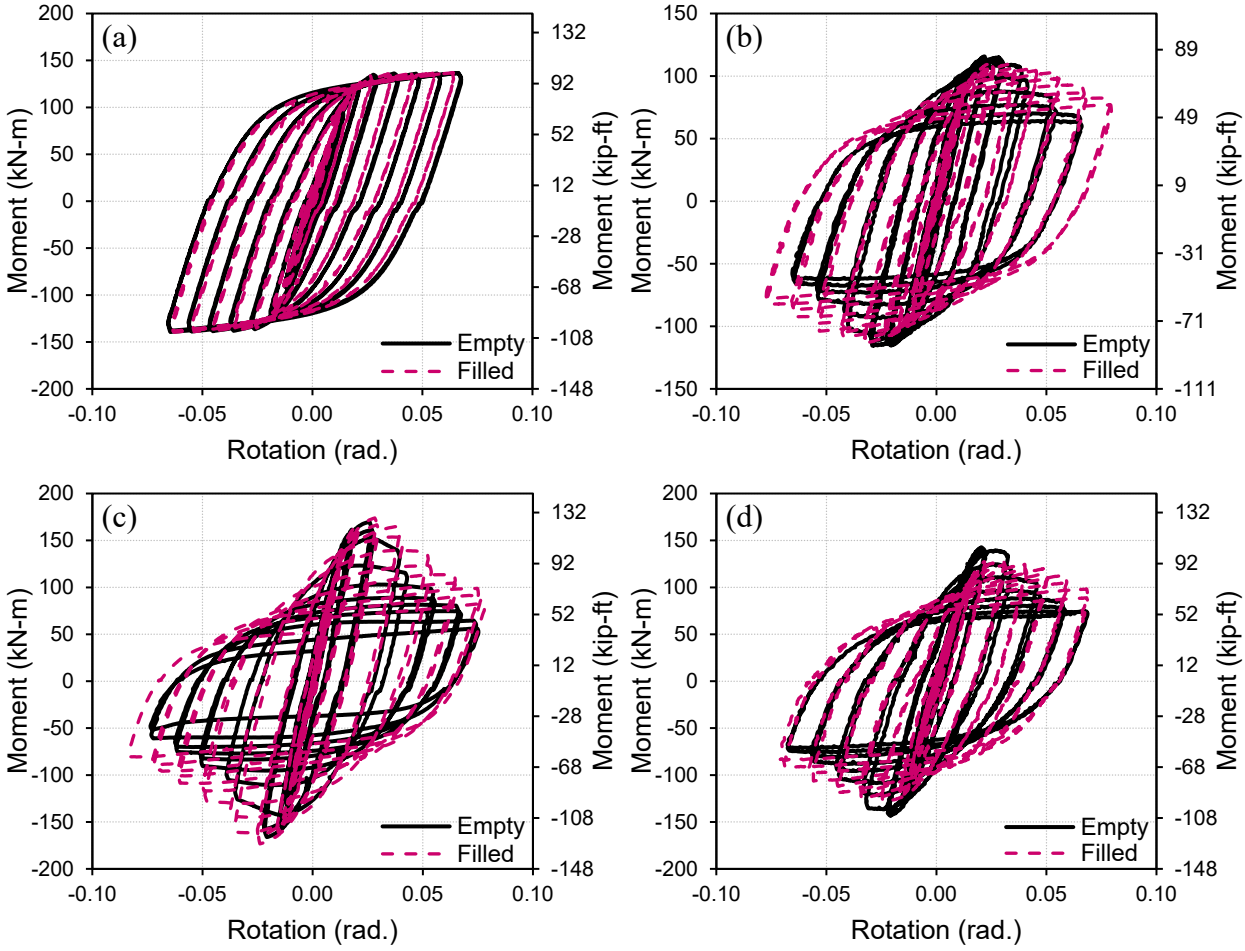

Figure III.5. Moment-rotation comparison for empty and filled HSS sections (a) H2, (b) M1, (c) M2, and (d) L1.

From Table III.3, the addition of the foam-fill results in a delay in the onset of local buckling in all cases except for section L1. In this case, as previously discussed, the foam-filled section has a significantly lower yield strength that leads to a lower maximum moment capacity and earlier onset of buckling. Regardless, after L1 buckles the foam-filled section still outperforms its empty counterpart by exhibiting a higher moment capacity with continued cycling (Fig.

III.5d). In terms of fracture, similar results are obtained. The onset of fracture or striation is delayed except for in section L2, although only by 0.002 rad. (3.2% earlier). In every test where fracture occurs, including L2, the size of the crack is reduced significantly (example shown in Fig. III.6c & Fig. III.6d). In the case of sections H1 and L1, the addition of the foam-fill results in preventing corner fracture completely.

With regards to moment capacity degradation, improvements are seen across all of the tested sections. The available data suggests the effectiveness of incorporating a foam-fill varies significantly based on the local slenderness ratios of each section. Highly ductile sections with small local slenderness ratios such as section H2 do not benefit from incorporating a foam-fill. Other sections with b/t ratios closer to the highly ductile limit, such as sections H1 and H3, can potentially experience performance improvements. While the low ductility sections experience noticeably less moment capacity degradation at 4% drift, section L2, which has the highest combined local slenderness ratios of the test specimens, started to fracture around the same rotation level as its empty version. Moderately ductile sections also exhibit noticeable improvements to capacity degradation at 4% drift and always experience a delayed fracture initiation due to the foam-fill. These results suggest there is a limit to how poor the cyclic performance of the HSS can be after which the foam-fill is not a strong enough material to be able to mitigate the effects of local buckling at high drifts. Ultimately, the fact that the foam-fill can significantly delay the moment capacity degradation of these sections suggests incorporating a foam-fill is a feasible approach for increasing the number of HSS that meet highly and moderately ductile criteria.

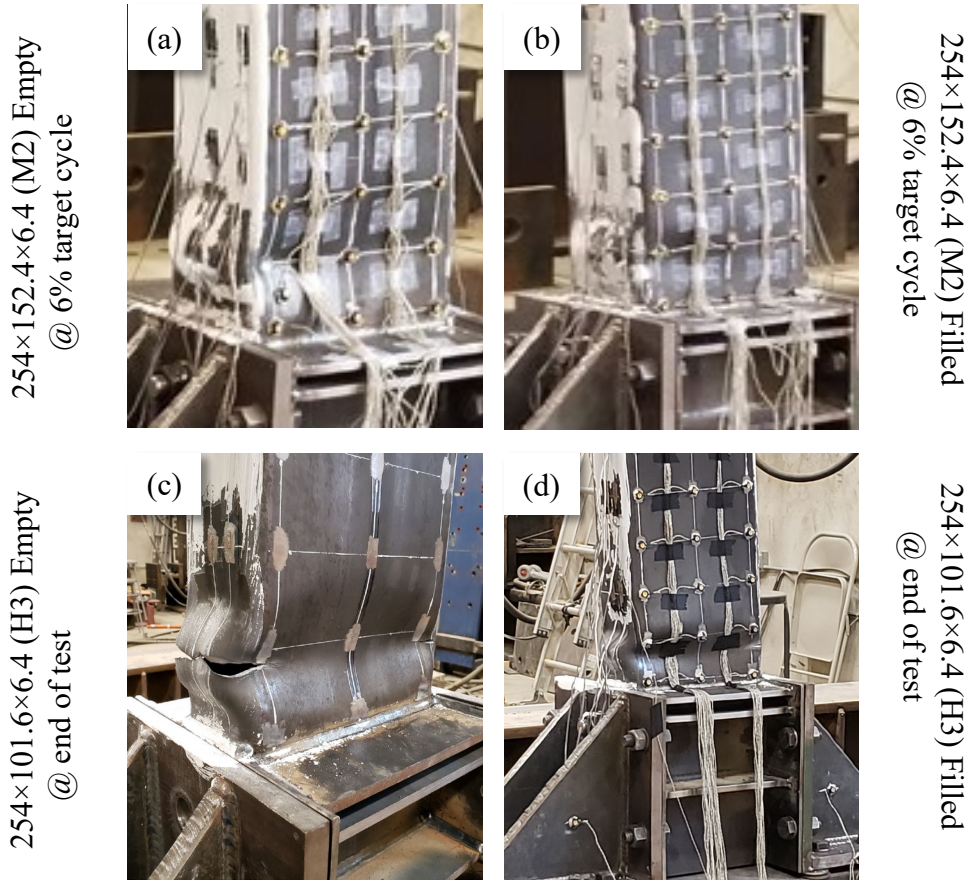

Figure III.6. Empty (a & c) and filled (b & d) comparison of the buckled shape of sections M2 and H3 at the 6% target cycle and end of testing.

Table III.3. Points of interest during testing and their corresponding rotation at first occurrence.

Section ID	Empty || Filled [rad.]			
	Buckling	Degradation at 4% Drift	Striation	Degradation Difference
H1	0.045 || 0.050	–	0.079 || –	–
H2	–	–	–	–
M1	0.030 || 0.036	16.0% || 7.4%	0.066 || 0.079	-53.8%
L1	0.032 || 0.031	24.8% || 3.4%	0.069 || –	-86.3%
H3	0.033 || 0.035	13.0% || 4.1%	0.060 || 0.075	-68.5%
M2	0.028 || 0.030	31.4% || 12.0%	0.062 || 0.076	-61.8%
L2	0.024 || 0.031	38.6% || 11.7%	0.063 || 0.061	-69.7%

Energy dissipation capacity

The performance improvements seen by incorporating the foam-fill are also accompanied by an increase in energy dissipation capacity. This capacity is determined by calculating the area enclosed by the load-displacement hysteresis curve. When the HSS walls buckle inward the foam crushes, helping dissipate some energy. Additionally, the foam-fill provides a stabilizing force against local buckling which helps to delay its onset and reduce the magnitude of the deformation. This allows the beam member to retain more of its strength, leading to better overall hysteretic performance and is a major contributing factor to the increase in energy dissipation capacity that is observed. Every foam-filled beam section exhibited an increase in energy dissipation capacity except for section H2, which is to be expected given that H2 did not sustain any local buckling. The difference in energy dissipation between the empty and foam-filled sections is very small prior to the onset of local buckling. At higher drifts and once buckling starts to occur the foam-filled sections start to exhibit larger amounts of energy dissipation (Fig. III.7). While the point at which the foam-filled section begins to distinctively outperform its empty counterpart varies from section to section, every foam-filled beam shows an overall increase in energy dissipation by the 4% drift ratio mark. At this drift level, the available data suggests that sections with low ductility experience a higher increase in energy dissipation capacity than those with moderate ductility. Sections that meet the highly ductile criteria benefit the least. For example, by the end of the 4% drift cycles the foam-filled sections M1, M2 and L1 exhibit a 6.1%, 14.6% and 28.8% increase in cumulative energy dissipation compared to their empty counterparts, respectively. In the case of section H2 there is no discernable improvement. It is important to note that more test data is needed to determine if the observed trend is maintained throughout a much wider range of sections with varying sizes and

local slenderness ratios. Regardless, these results suggest the addition of the foam-fill can enhance the HSS beam's hysteretic behavior by increasing its energy dissipation capacity with continued cycling.

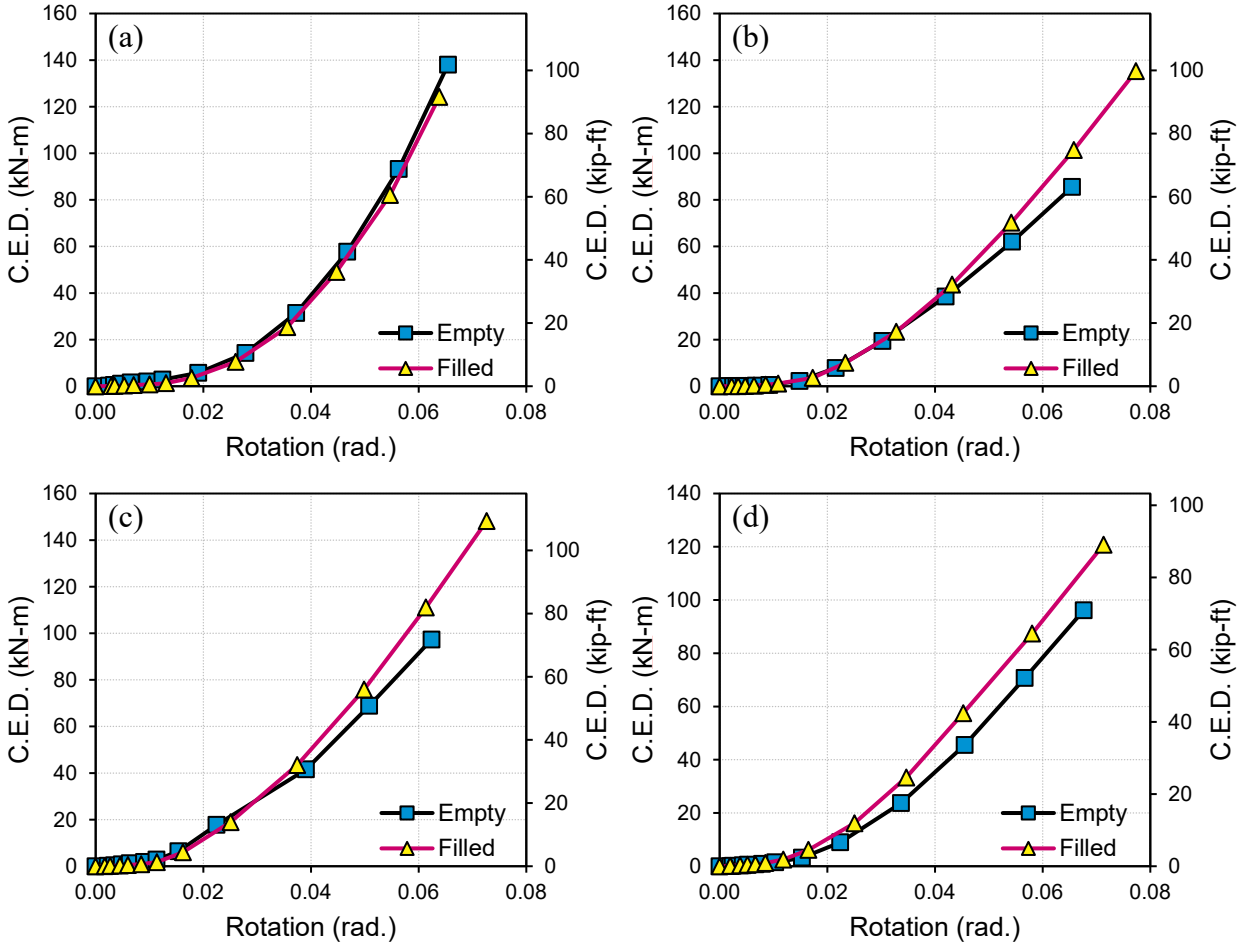

Figure III.7. Cumulative energy dissipation (C.E.D.) capacity at the end of each cycle magnitude for empty and filled HSS sections (a) H2, (b) M1, (c) M2, and (d) L1.

Strain

Strain data provides insight into how the addition of the foam-fill influences the stress distribution along the beam and how this affects cyclic performance. The extent of the deformation in the plastic hinge region has a significant influence on the magnitude of the strains along the rest of the beam member. In the case of the empty beams, a noticeable drop in strain is

recorded away from the plastic hinge region once local buckling occurs (Fig. III.8). As the plastic hinge region undergoes significant deformation a large portion of the strains become concentrated in this area, lowering the amount of strain, and therefore stress, in the rest of the beam member. This reduction in stress along the beam essentially lowers its participation in the load bearing process, which results in the loss of moment capacity.

As shown previously, incorporating the foam-fill manages to reduce the extent of the deformation due to local buckling. Reducing the strain concentrations in the plastic hinge region results in larger strains along the rest of the beam when compared to their empty counterparts. This allows the foam-filled beam to retain more of its moment capacity despite experiencing local buckling. In the examples shown in Fig. III.8 the strain just below the end of the foam-fill exhibited a 16.8% (Fig. III.8a) and 143% (Fig. III.8c) increase at 4% drift for specimens H3 and M2, respectively, when incorporating the foam. In the case of specimen L2 a 47.6% increase in the strain just below the end of the foam-fill was recorded at 4% drift and for specimen H2 only a 7.1% increase. The low percent increase in the case of specimen H2 is expected due to the empty specimen H2 not experiencing any local buckling or capacity degradation. Overall, the available strain data suggests highly ductile sections stand to benefit the least from the application of the foam-fill, while moderately ductile sections can benefit the most and sections with low ductility stand somewhere in between.

A visual inspection of the beams after testing confirms that using a foam length of 1.5 times the theoretical plastic hinge length managed to ensure the foam was present throughout the areas that experienced local buckling. It did not, however, ensure that the foam would be present in any region that experienced yielding, as shown in Fig. III.8d. While this investigation does not study the differences between having the foam present throughout every region that experienced

yielding, it does suggest that having the foam in the local buckling region is enough to make a noticeable difference in the beam's cyclic behavior. Another observation concerns the strain distribution along the cross-section of the beams. As expected, in most cases the strain gages in the same horizontal row report very similar strain values. This is not the case when significant buckling occurs near the strain gages. In these cases, the buckled shape determines how the strain profile looks.

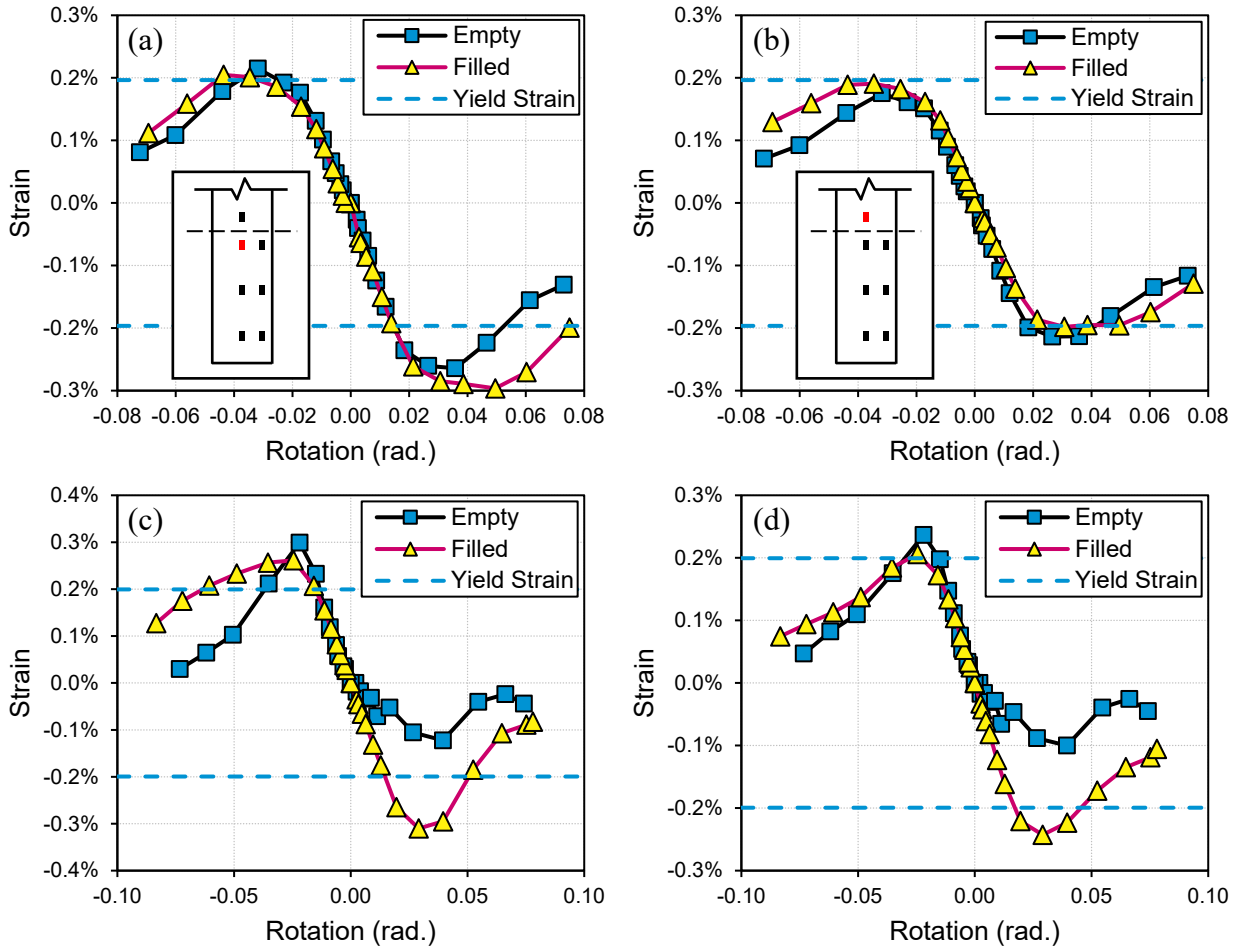

Figure III.8. Empty and filled strain backbone curves for flange centerline strain gages (a & c) below and (b & d) above the end of the foam-fill in beam specimens (a & b) H3 and (c & d) M2.

Ductility Rating for Foam-Filled HSS

While incorporating the foam-fill can improve the cyclic behavior of HSS beams, ultimately the main goal of this approach is to decrease the stringent local slenderness requirements that are necessary to ensure proper ductility. Doing so will increase the number of HSS sizes that can be utilized for IMFs and SMFs, potentially allowing designers to make more frequent use of tubular sections as beam members. The criteria that are used in this study to determine if a section meets a certain ductility rating is being able to maintain at least 80% of its maximum moment capacity at the 2% and 4% drift ratio for moderate and high ductility ratings, respectively. All seven empty beam tests conducted did not exhibit any moment capacity degradation when 2% drift was first reached, suggesting that all seven sections meet the moderately ductile criteria. For this reason, the benefits of the foam-fill are better observed at the 4% drift ratio.

Experimental test results from Fadden and McCormick (2012) provide a frame of reference in regards to the performance of empty HSS beams that can be used to contextualize the change in behavior of these sections on a broader scale when incorporating the foam-fill. Fig. III.9 presents a contour plot that shows the moment capacity degradation of empty HSS beams at 4% drift in relation to their local slenderness ratios. Six of the tested sections are plotted over the contours using their nominal *b/t* and *h/t* ratios. Section H2 was not added because its local slenderness ratios are outside the range of data presented in the contour plot. Indicated next to each data point are both the empty (E) and foam-filled (F) beam's moment capacity degradation at 4% drift from Table III.3. A visual comparison confirms that the results from the empty beam tests align well with previous test data. If the degradation of the foam-filled beams is considered, these would significantly affect the contour lines, shifting them upwards. These results indicate that sections L1, M2, and L2 now meet the highly ductile criteria when filled with the

polyurethane foam. Given more test data, creating a version of the contour plot for foam-filled HSS beams can lead to establishing less stringent local slenderness limits for these sections.

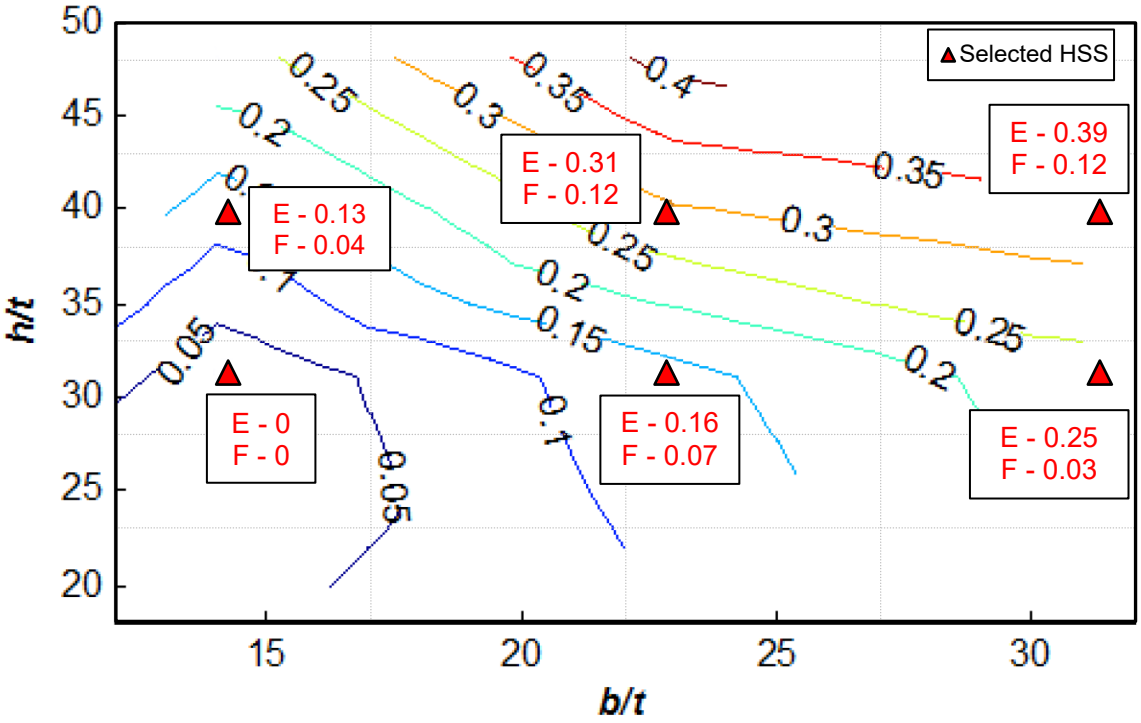

Figure III.9. Moment capacity degradation in decimal percent at 4% drift. Overlapped are the tested beam sections in this study with their corresponding moment capacity degradation percentages for both the tested empty (E) and foam-filled (F) versions. Contour plot created with experimental empty HSS beam data from Fadden and McCormick (2012) with their permission.

Conclusions

Seven pairs of empty and polyurethane foam-filled HSS beams are tested under fully symmetric cyclic loading to examine the potential performance benefits from incorporating a foam-fill. The objective of this approach is not only to improve the behavior of HSS beams under cyclic loading, but also to lessen the stringent local slenderness requirements necessary for these sections to be able to provide the appropriate ductility for IMFs and SMFs. By doing so, a larger number of HSS would be available for use in building design, allowing more engineers to make use of their beneficial properties such as good bending strength, excellent torsion

resistance, and pleasing aesthetics. The metrics by which the effects of the foam-fill are measured include its ability to mitigate moment capacity degradation with continued cycling, ability to delay and reduce the extent of local buckling and fracture, effect on energy dissipation capacity, and ability to meet the ductility requirements for IMFs and SMFs. Additionally, strain data along the flange of the section is used to provide insight into how the foam-fill affects the stress distribution along the beam. The key results of this study are summarized as follows:

1. The addition of the foam-fill has a minimal effect on the maximum moment capacity of the HSS beams. Due to the large differences in material strength and stiffness between the polyurethane foam and the steel, the foam only plays a supportive role providing stability and additional energy dissipation capacity to the HSS walls once they begin to undergo large deformations. For this reason, the elastic behavior of the section is not affected. In the case of a section that does not experience any buckling, the foam-fill also does not noticeable influence its behavior.
2. The foam-fill manages to delay the onset of local buckling in all but one of the tested beams and in every case reduces the extent of deformation in the plastic hinge region. This behavior results in an overall reduction in moment capacity degradation with continued cycling that generally delays, and in some cases prevents, the onset of fracture.
3. The degree to which the foam-fill affects the behavior of each beam varies depending on the local slenderness ratios of each section. Beam sections that meet the highly ductile criteria can potentially benefit from the foam-fill if they still experience some amount of local buckling. The moderately ductile sections experience less moment capacity degradation and delayed fracture initiation with the foam-fill. In the case of the sections that do not meet the moderately ductile local slenderness criteria, the beam with the

highest local slenderness ratios (b/t of 29.5, h/t of 37.7) did not experience a delay in fracture initiation even though capacity degradation was reduced at earlier cycles. These results suggest there are limits to the local slenderness values above which the effectiveness of the foam-fill is reduced.

4. The foam-fill increases the beam's energy dissipation capacity and reduces the strain concentrations in the plastic hinge region once local buckling occurs. By mitigating the effects of local buckling in this manner, the stress in the beam flanges outside of the local buckling region does not drop as significantly as in the empty beams. This phenomenon allows the parts of the beam that have not suffered local buckling to maintain their participation in the load resisting process and effectively results in less moment capacity degradation with continued cycling.
5. The strain data shows that the foam-fill does not need to be present along every region that experiences yielding to be able to have a positive impact on the beam's behavior. If the foam is present in any area that experiences local buckling it can help mitigate its effects.
6. The addition of the foam-fill manages to change the ductility rating of three of the tested beam sections. The criteria for highly and moderately ductile sections is maintaining 80% of its maximum moment capacity out to 2% and 4% drift, respectively. Based on these criteria, three of the empty beam sections meet the moderately ductile requirements and the remaining four can be considered highly ductile. Once the foam-fill is introduced, the three moderately ductile sections were able to maintain at least 80% of their capacity at 4% drift, indicating that they now meet the highly ductile requirements. These results suggest that incorporating a polyurethane foam-fill in the voids of HSS beams is a

feasible approach to having less stringent local slenderness requirements for these sections and increasing the amount of section sizes that can meet moderately and highly ductile requirements.

CHAPTER IV

A Parametric Study of Urethane Foam-Filled HSS Beams

Introduction

The previous chapter explored the potential benefits of incorporating a polyurethane-based foam-fill in the voids of HSS beam members. Experimental testing showed that the foam-fill can have a significant impact on the beam's cyclic behavior by mitigating the effects of local buckling. The addition of the foam-fill results in a reduction of the extent of deformation in the plastic hinge region and therefore the foam-filled beams experience less moment capacity degradation with continued cycling when compared to an un-filled HSS beam. Given these results, the concept of incorporating a urethane foam-fill was shown to be a feasible approach to improving the cyclic performance of HSS beams in seismic structural applications. In some cases the performance improvements were significant enough to allow the foam-filled HSS to be classified as a highly ductile section, while the empty version of the HSS did not meet these requirements.

While the experimental results showed promise for this approach, the testing suite was small and comprised of only seven pairs of empty and foam-filled HSS beams. A much larger data set is needed to better understand the extent of the influence of the foam-fill on HSS beams across a wide variety of local slenderness ratios and section sizes. To this end, a large-scale computational parametric study that explores the differences in behavior between 52 pairs of empty and foam-filled HSS beams is undertaken. The results and data from the experimental

tests are used to inform the development of detailed finite element (FE) models in Abaqus (Simulia 2017). Similar performance metrics as those considered in analyzing the experimental tests are used to assess the potential benefits of incorporating the urethane foam-fill in HSS beams, including moment capacity degradation with continued cycling and ability to meet moderately and highly ductile member criteria.

Development of the Finite Element Model

General details

The FE model replicates the experimental setup presented in Chapter 3 and uses symmetry to decrease computation time (Fig. IV.1). The half model is constructed by considering only half of the cross-section on the full length of the beam. With this approach the force data obtained from the simulations can be multiplied by two to obtain the force acting on a complete section. A mesh size of 6.35 mm (0.25 in.) is used from the fixed end of the beam up to 1.5 times the theoretical plastic hinge length. The plastic hinge length is calculated by using Eq. III.1. The rest of the beam has a 25.4 mm mesh size. The corner mesh size is adjusted for every section so that it contains at least 4 elements along the arc. The value used for the corner radius is two times the design wall thickness of the section. Reference points are placed at both ends of the beam at what would be the middle of the cross section if it was a full model and multi-point beam constraints are used to connect the elements at the beam ends to the corresponding reference point. With this configuration, the boundary conditions and loading protocol are applied to the beam member through the reference points. The loading protocol that is used is the same fully reversed, symmetric protocol as in the experimental tests (Fig. III.3b). An elastic spring boundary condition at the fixed end is used during calibration and validation of the FE model to account for the rigid body rotation that occurs in the experimental tests. This boundary condition is later

changed to fully fixed for the parametric study. The rotational stiffness of the elastic rotational spring used for calibration purposes is 14,688 kN-m/rad. (10833 kip-ft/rad.), a value that was determined through an iterative process to match the observed rotational stiffness in the experimental test. Additional boundary conditions are applied to the cut edges and faces of the HSS beam and foam which restrict out of plane movement of these elements. These boundary conditions are necessary to ensure proper out of plane symmetry in the half model.

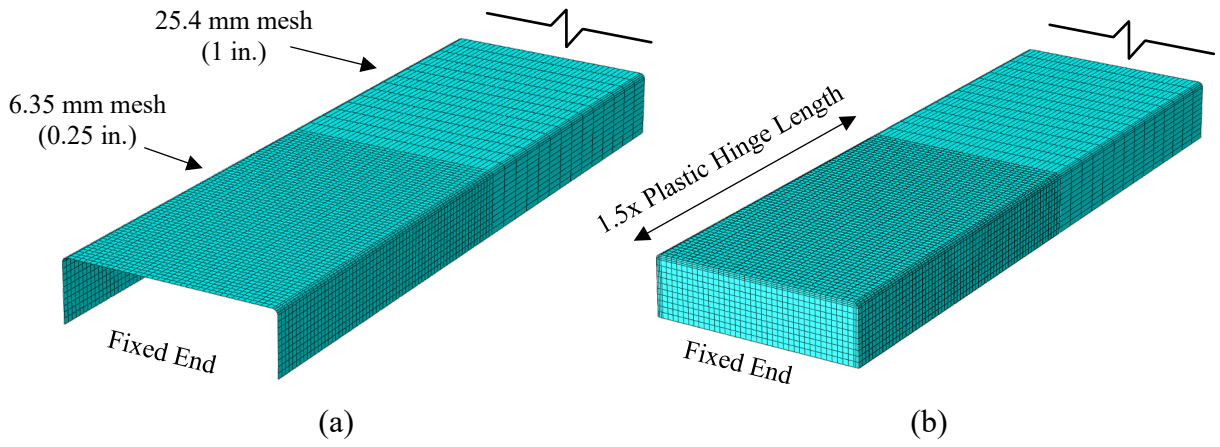

Figure IV.1. (a) Empty and (b) foam-filled FE half models.

S4H shell elements are used for the HSS walls and C3D8R solid elements are used for the urethane foam-fill. A penalty contact interaction with a static friction coefficient of 0.3 is applied between the outer foam surfaces and the inner HSS walls. This interaction property prevents the foam and steel elements from passing through each other and is a good representation of the experimental results which confirmed minimal bond between the two materials. An initial imperfection is also applied to both the HSS beam and the foam-fill given that the foam would take the shape of the inner walls of the HSS beam, including this initial imperfection. The imperfection is in the shape of the first two buckling modes of the HSS (Fig. IV.2) with a magnitude of half of the maximum allowable imperfection prescribed by the American Society

for Testing and Materials for cold-formed tubular shapes (ASTM 2018). The first two buckling modes are of equal shape and magnitude but primarily act on opposite sides of the HSS member; both are combined to form the shape of the imperfection across the entire section. The magnitude of the applied imperfection corresponds to half of 1% of the large flat dimension of the HSS. Changing the magnitude of the imperfection mostly affects the maximum moment capacity of the beam (i.e., maximum moment capacity decreases as the imperfection magnitude increases) and has little to no influence on the capacity degradation after the onset of buckling. The magnitude value was chosen after conducting a parametric study that showed good agreement between the FE model and all the experimentally tested sections. Fracture is not considered in the models because it typically occurs after the 6% drift level, well above the 2% and 4% drift ratios that intermediate (IMFs) and special moment frames (SMFs) are expected to sustain, respectively.

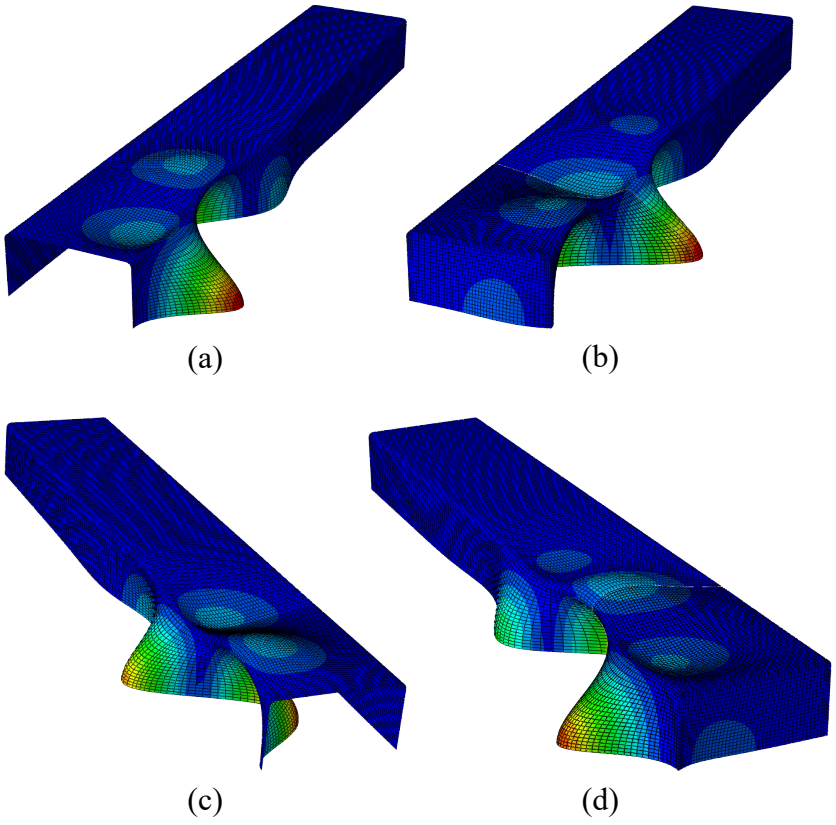

Figure IV.2. Example of the (a & b) first and (c & d) second buckling modes for the (a & c) empty and (b & d) foam-filled HSS 304.8×304.8×12.7 (HSS 12×12×1/2) beam.

Model calibration and validation

The experimental data for empty and foam-filled HSS beams from Chapter 3 is used to inform the development of the FE models. The calibration process begins with the empty beam section. When the foam-fill is added, no other changes are made to the model to ensure any differences in behavior are solely due to the presence of the foam. The steel beam is partitioned into flat and corner regions so that different material properties can be applied to both. This approach takes into consideration the effects of cold working that typically result in the HSS corners exhibiting a higher yield strength, but lower ductility than the flat regions. A more in-depth discussion on this topic is available in Fadden and McCormick (2014a).

The material model used for the steel is a combined kinematic and isotropic hardening law. Steel coupons are fashioned from unused portions of each experimentally tested HSS beam and tested under monotonic tension. The data from these coupon tests is used to obtain the kinematic hardening parameters by following the procedure detailed in Maximov et al. (2008). This procedure uses a plastic stress-strain half-cycle curve to obtain the material constants C and γ, where C is the initial kinematic hardening modulus and γ is the rate at which the kinematic modulus decreases as the equivalent plastic deformation increases. The isotropic hardening parameters Q_∞ and b are determined through an iterative approach by comparing the FE model behavior to the experimental data. Q_∞ is the maximum change in the size of the yield surface and b is the rate at which the size of the yield surface changes as the plastic strain increases. Table IV.1 contains the material parameters that are used for the HSS models.

Table IV.1. Material properties used in the HSS beam finite element model.

HSS Region	Elastic Modulus (GPa | ksi)	Yield Strength (MPa | ksi)	Isotropic Hardening Parameters		Kinematic Hardening Parameters	
			Q_∞ (MPa | ksi)	b	C (MPa | ksi)	γ
Flats	195 | 28329	393 | 57	96.5 | 14	6	3423 | 497	26.3
Corners	202 | 29244	497 | 72.1	46.2 | 6.7	6	14220 | 2062	295

The material properties of the foam-fill are simulated with a crushable foam material model. This model uses an isotropic hardening law. Values of one and zero are used for the compression yield stress ratio and plastic Poisson's ratio, respectively. Additional foam hardening data past the yield point is obtained from experimental foam cube tests (see Chapter III). Since the strength of the foam-fill can vary significantly, the foam properties are selected to represent an average strength and behavior of the foam (Fig. IV.3). These material properties are obtained through an iterative process in which the experimental data is compared to an FE simulation of the compression tests of the foam cubes.

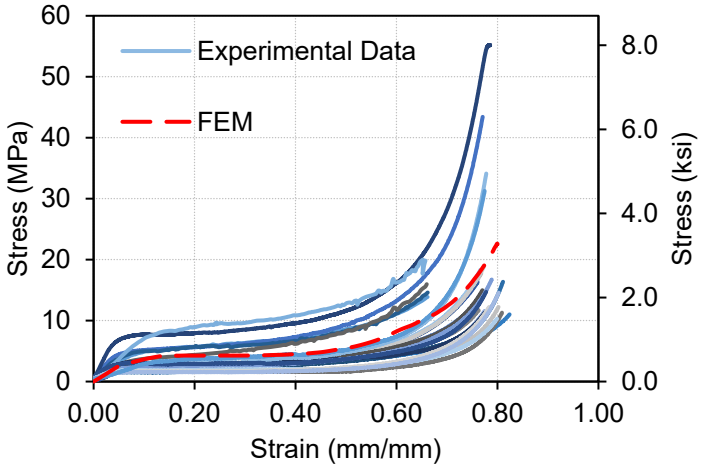

Figure IV.3. Stress-strain behavior comparison between the experimental and FE simulation of the monotonic compression foam cube tests. Loading rate: 0.254 mm/s.

The FE model is initially calibrated to the behavior of the HSS 254×152.4×6.4 (HSS 10×6×1/4) beam and validated using the data from other experimentally tested sections. Fig. IV.4 shows the calibration of the model is adequate as it can accurately simulate the moment-rotation behavior and the cumulative energy dissipation for both empty and foam-filled HSS beam sections. In the case of the empty HSS beam (Fig. IV.4a), there is a noticeable difference between the moment capacities of the FE and the experimental results after 6% drift. This difference can be attributed to the fact that the FE model does not consider fracture, which had already initiated at this point during the experimental test. Fracture is not incorporated into the model because it only occurs at large drift levels that are beyond which intermediate and special moment frames are designed. The same large difference between the experimental and simulated results does not occur in the case of the foam-filled HSS beams (Fig. IV.4b). In the experimental test, incorporating the foam-fill mitigates the moment capacity degradation by reducing the degree of local buckling, thus leading to a delay of the onset of fracture. For this reason, the

foam-filled HSS beam FE model is capable of higher accuracy than the empty model out to larger drift levels.

The FE model is further validated by using the same properties and modeling approach to simulate other experimentally tested HSS beam sections. Similar accuracy to HSS used to calibrate the model is observed when other HSS sizes are simulated (Fig. IV.5) showing that the modeling approach can reliably provide an accurate representation of the cyclic behavior of empty and foam-filled HSS beam sections. In the case of the empty HSS beams, the average difference in moment capacity between the experimental and simulated results at the first cycle to the 2% and 4% drift ratio is 5.4% and 7.1%, respectively; in the case of the filled beams, it is 5.6% and 6.7%, respectively. An additional parameter of comparison is the progression of secant stiffness with continued cycling. From Fig. IV.6, the model can also adequately simulate the degradation in stiffness throughout the loading protocol that occurs as a consequence of yielding and buckling.

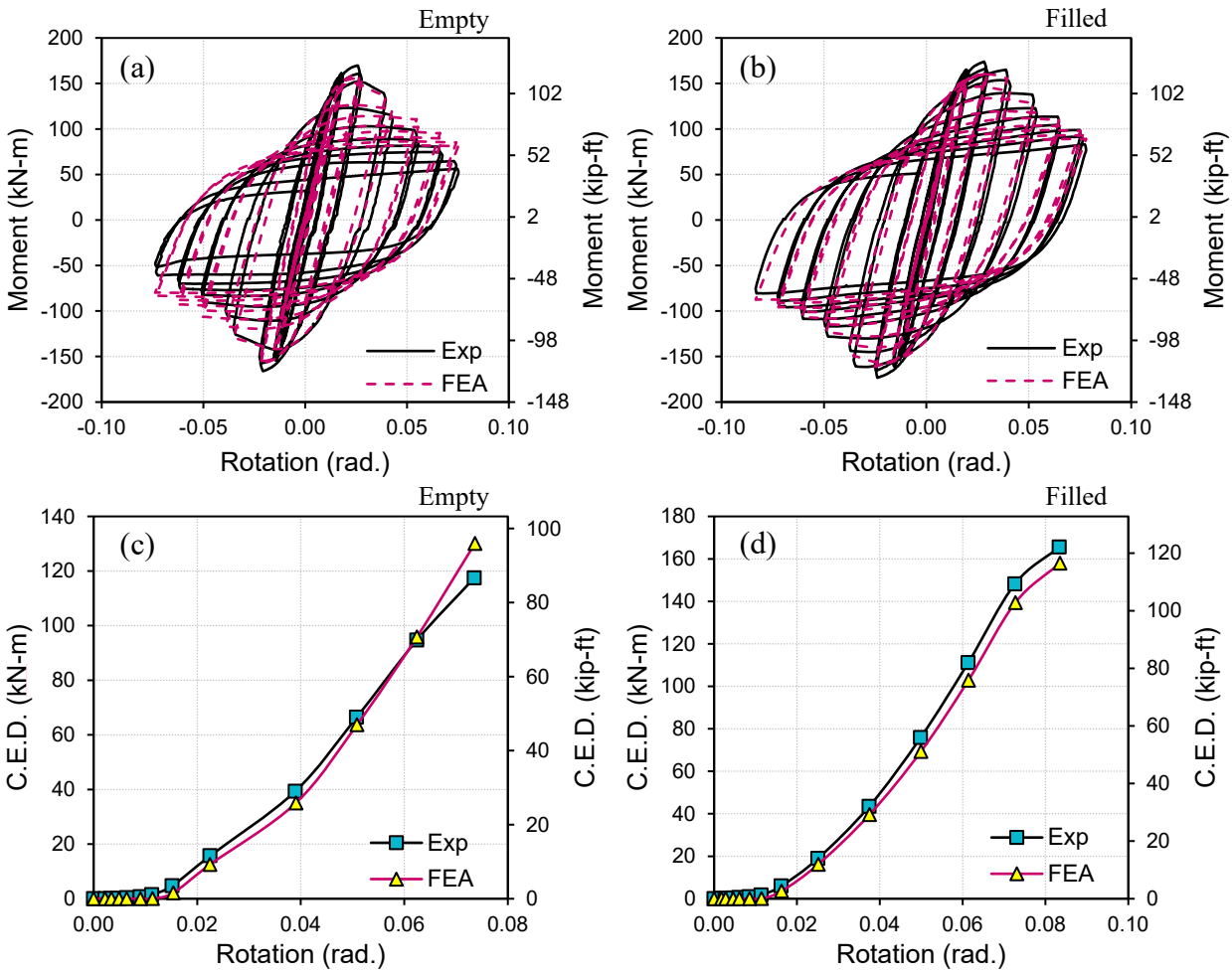

Figure IV.4. Moment capacity and cumulative energy dissipation versus rotation comparisons between the experimental data and the FE simulation for (a & c) empty and (b & c) foam-filled HSS 254×152.4×6.4 (HSS 10×6×1/4).

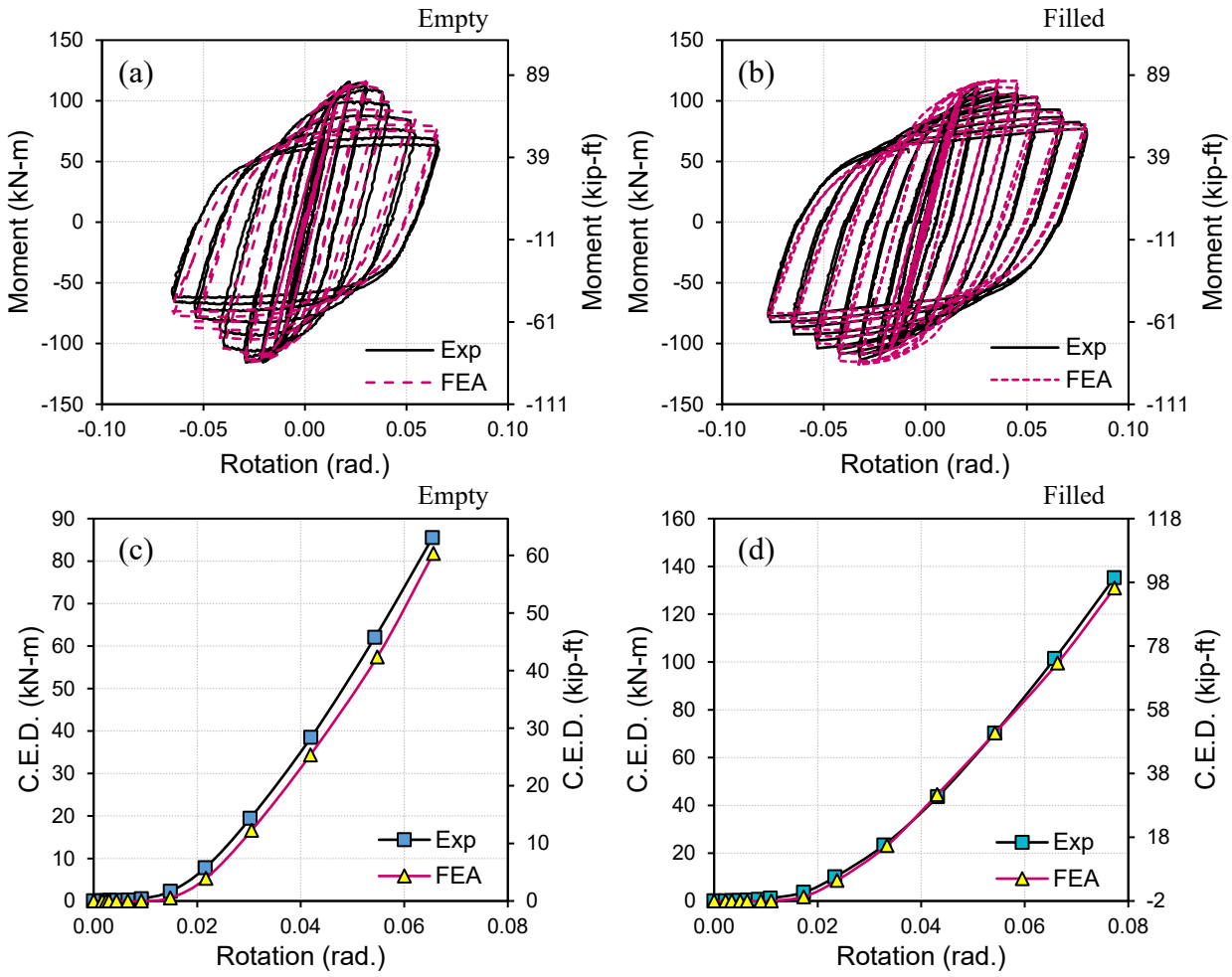

Figure IV.5. Moment capacity and cumulative energy dissipation versus rotation comparisons between the experimental data and the FE simulation for (a & c) empty and (b & c) foam-filled HSS 203.2×152.4×6.4 (HSS 8×6×1/4).

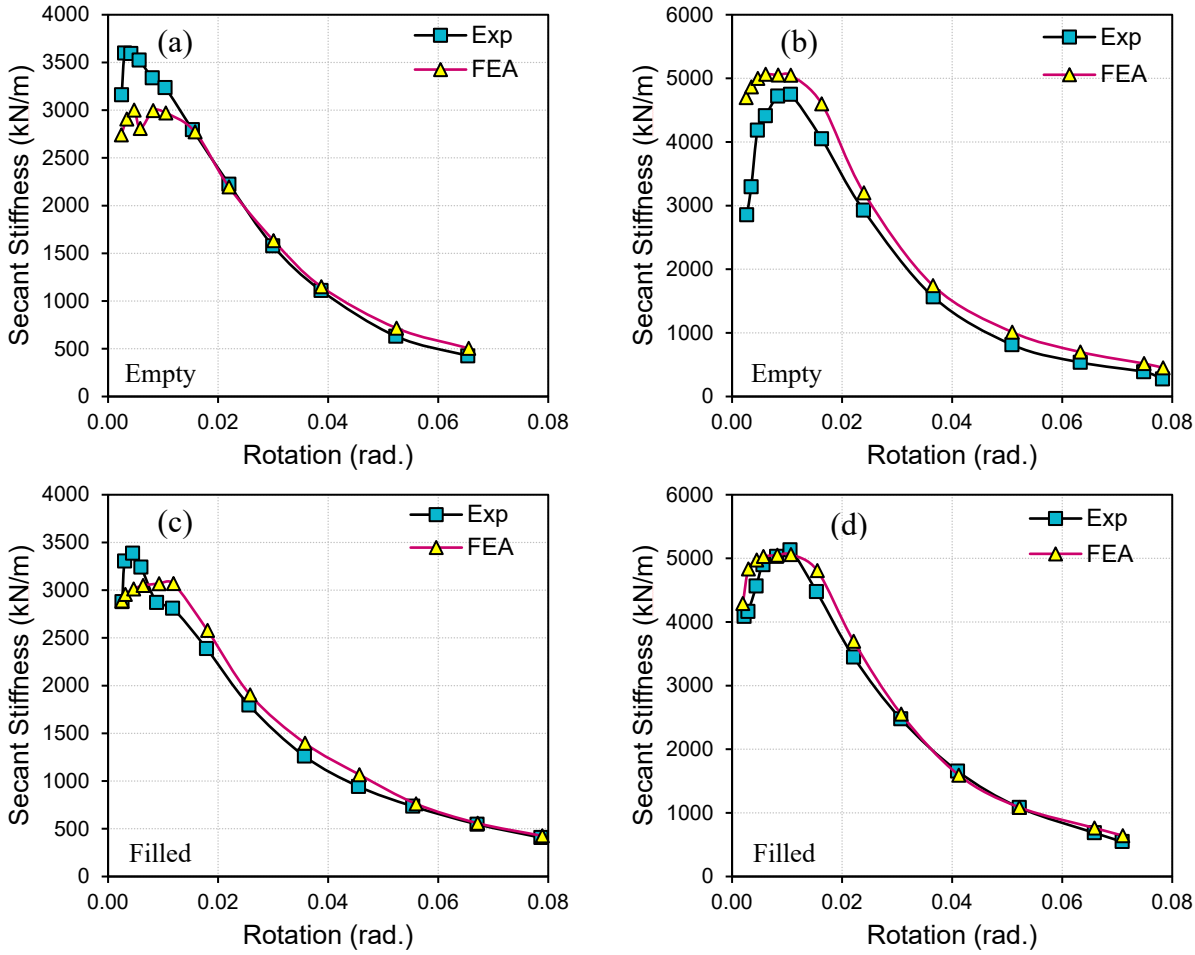

Figure IV.6. Secant stiffness comparisons between the experimental data and the FE simulation for empty and foam-filled (a & c) HSS 203.2×152.4×6.4 (HSS 8×6×1/4) and (b & d) HSS 254×203.2×6.4 (HSS 10×8×1/4).

Parametric Study

Scope of the parametric study

The limited sample size of the experimental tests in Chapter 3 is significantly expanded through a detailed FE parametric study. The experimental data consists of seven HSS beams that span nominal *b/t* and *h/t* ratios of 8.46 to 31.3 and 19.9 to 39.9, respectively. The FE parametric study includes a total of 52 pairs of empty and urethane foam-filled HSS beams (Fig. IV.7). The *b/t* and *h/t* ratios in the parametric study cover values of 8.46 to 31.5 and 14.2 to 57.1,

respectively. The FE parametric study also allows for the exploration of the effects of the foam-fill on much larger sections that could not be tested experimentally due to limitations of the test equipment. The largest section that was physically tested was the HSS 254×203.2×6.4 (HSS 10×8×1/4) while the FE study includes section sizes up to the HSS508×304.8×15.9 (HSS20×12×5/8). The parametric study consists of 16 sections that meet the AISC highly ductile *b/t* limit, 26 sections that meet the moderately ductile limit, and 10 sections that are considered as having low ductility given their *b/t* ratios are larger than the moderately ductile limit. The ductility rating is determined by comparing the nominal *b/t* ratio of each section to the *b/t* limits for each classification. These limits are calculated with Eqs. IV.1 and IV.2 using the measured elastic modulus (E) and expected yield strength (R_yF_y) of the HSS flats.

$$\left(\frac{b}{t}\right)_{hd} = 0.65\sqrt{\frac{E}{R_yF_y}} \qquad \text{(Eq. IV.1)}$$

$$\left(\frac{b}{t}\right)_{md} = 1.18\sqrt{\frac{E}{R_yF_y}} \qquad \text{(Eq. IV.2)}$$

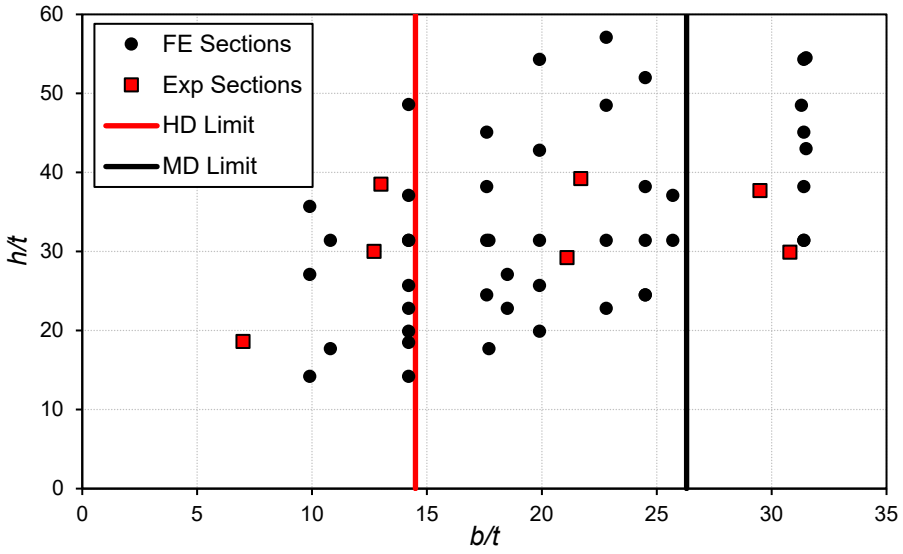

Figure IV.7. Plot of all HSS sizes included in the parametric study with respect to their local slenderness ratios. AISC ductility limits calculated using nominal geometric properties and measured material properties are also depicted.

Effect of the foam-fill on moment capacity degradation

Incorporating the urethane foam-fill improved the performance of the HSS beams by reducing the moment capacity degradation across the 52 pairs of sections considered. On average, at the 2% drift cycle the empty HSS exhibited 3.9% (σ = 7.3%) moment capacity degradation as opposed to 1.6% (σ = 4.7%) for the foam-filled HSS beams. At the 4% drift cycle, the average moment degradation was 18.3% (σ = 14.6%) and 11.5% (σ = 13.3%) for the empty and foam-filled HSS beams, respectively. The degree to which the foam-fill mitigates the effects of local buckling depends on the local slenderness ratios of each HSS. Figs. IV.8 and IV.9 plot each HSS's moment capacity degradation at 2% and 4% drift, respectively, against their *b/t* and *h/t* ratios. A linear regression of the data shows there is a positive correlation between the moment degradation and the local slenderness ratios, as expected. Data points associated with the experimentally tested sections are not added in Fig. IV.8 because none of these sections experienced moment capacity degradation at the 2% drift level as discussed in Chapter 3.

The slope, y-intercept, and R^2 values of each linear regression are provided in Table IV.2. For both plots in Fig. IV.8 incorporating the foam-fill results in a reduction of the slope of the linear regression, suggesting that the foam-fill reduces the impact of the local slenderness ratios on the section's moment capacity degradation. The slopes from the linear regressions also indicate that at 2% drift the value of *h/t* is slightly more impactful than the value of *b/t* when considering how much moment capacity degradation the HSS beam experiences. At this drift, the slope of the linear regression lines with respect to *h/t* are 8.3% and 23.8% larger than those for *b/t* for the empty and foam-filled HSS beams, respectively. At 4% drift the opposite is observed with the slope of the linear regression lines with respect to *b/t* being 21.0% and 7.5% larger than those for *h/t* in the case of the empty and foam-filled HSS beams, respectively. Further, at both 2% and 4% drift the linear regression lines with respect to *h/t* have significantly larger R^2 values than the *b/t* regression lines, suggesting that there is more correlation between the moment capacity degradation and the *h/t* value than there is with the *b/t* ratio. Incorporating the urethane foam-fill also has the effect of reducing the R^2 value in every instance. This result is expected as the addition of the foam-fill decreases the amount of local buckling and reduces the moment degradation associated with each section. Overall, these results suggest that both local slenderness ratios (*b/t* and *h/t*) influence the performance of the HSS beams, and the foam-fill reduces the effect these ratios have on the amount of moment capacity degradation that each HSS beam is expected to experience.

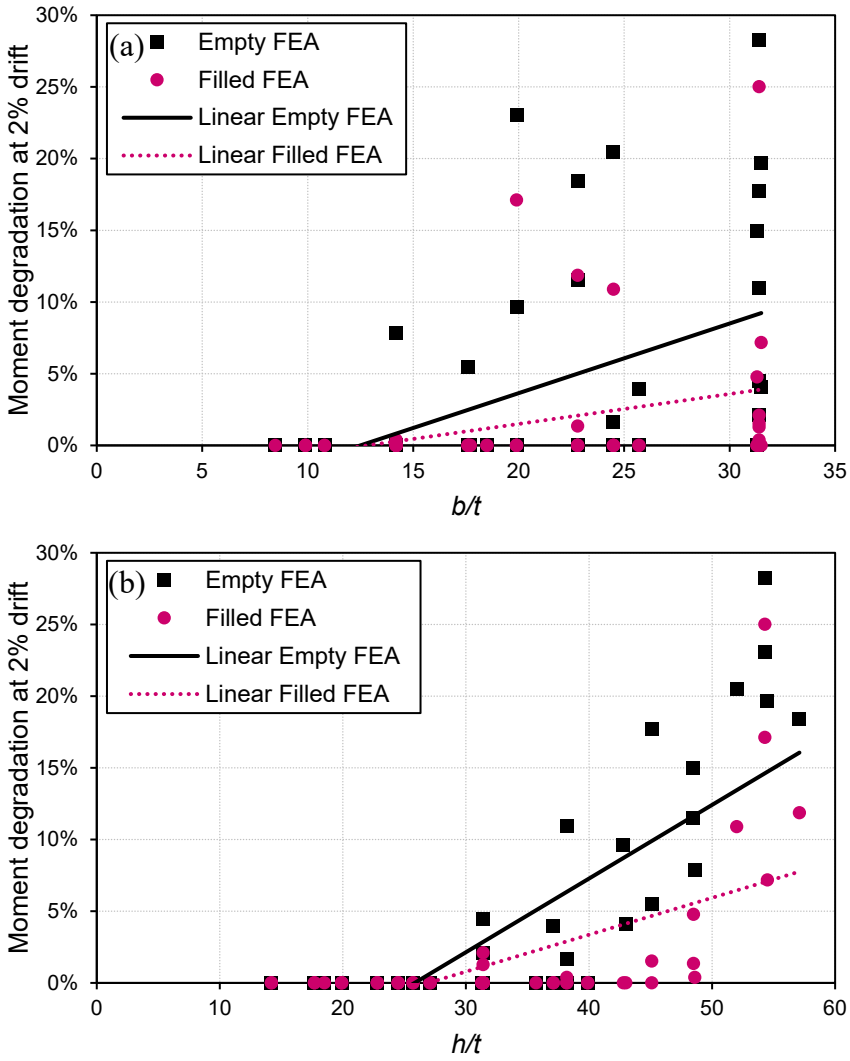

Figure IV.8. Moment capacity degradation at 2% drift for the empty and foam-filled HSS beams with respect to their (a) *b/t* and (b) *h/t* local slenderness ratios.

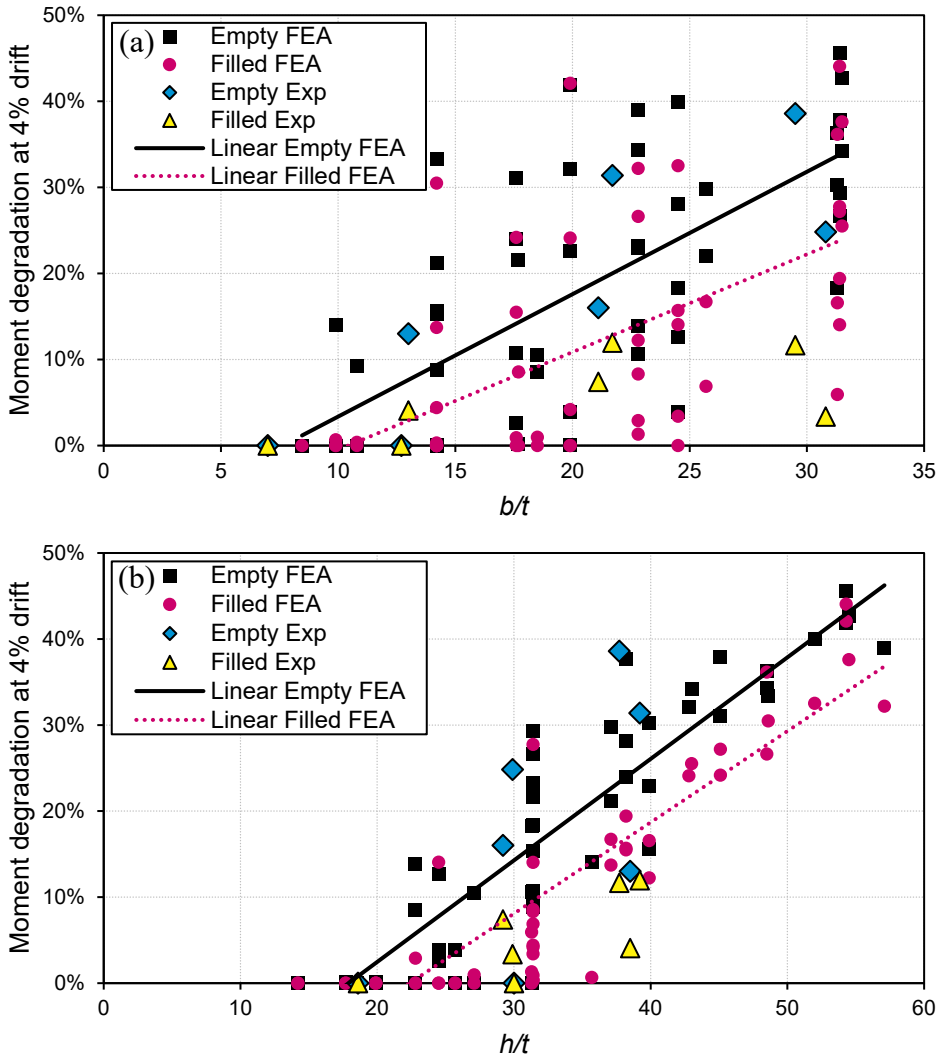

Figure IV.9. Moment capacity degradation at 4% drift of empty and foam-filled HSS beams with respect to their (a) *b/t* and (b) *h/t* local slenderness ratios.

Table IV.2. Values for the linear regression plots between moment capacity degradation and the local slenderness ratios.

Drift	Local Slenderness	Slope		Y-Intercept		R^2	
		Empty	Filled	Empty	Filled	Empty	Filled
2%	*b/t*	0.0048	0.0021	-0.0601	-0.0268	0.2139	0.0959
	h/t	0.0052	0.0026	-0.1338	-0.0694	0.6402	0.3751
4%	*b/t*	0.0144	0.0114	-0.1131	-0.1185	0.4727	0.3526
	h/t	0.0119	0.0106	-0.2129	-0.2373	0.8344	0.7922

Ductility classification of empty and foam-filled HSS

The current ductility criteria for a connection in an IMF (moderate ductility) or an SMF (high ductility) requires the beam to maintain at least 80% of its maximum moment capacity at 2% and 4% drift, respectively (AISC 2016a). To ensure that an HSS beam meets the appropriate ductility criteria, the AISC Seismic Provisions (2016a) places limits on the *b/t* ratio of the section in order to classify it as moderately or highly ductile. The current limits for a highly and moderately ductile HSS beam member can be calculated using Eqs. IV.1 and IV.2, respectively. Using the measured material properties of the HSS flats provided in Table IV.1, the highly and moderately ductile *b/t* limits are 14.5 and 26.3, respectively.

Comparing the ductility requirement of the beam based on the seismic connection qualification requirements for IMF and SMF to the ductility rating obtained through the *b/t* limits provides insight into the adequacy of the local slenderness limits and how these might be influenced by incorporating the urethane foam-fill into HSS beams. As mentioned previously, in the case of the empty HSS, 16 of the studied section sizes meet the high ductility *b/t* limit, 26 of the studied section sizes meet the moderate ductility limit, and 10 of the studied section sizes have larger *b/t* ratios than the moderate ductility limit. By comparison based on the cyclic performance of the beams and the connection prequalification criteria, the FE data suggests 27 of the empty sections meet the high ductility requirement, 22 of the empty section sizes meet the moderate ductility requirement, and 3 of the empty section sizes do not meet the moderate ductility criterium. These results suggest that the current local slenderness limits for empty HSS members used as beams may be conservative. In the case of the foam-filled HSS beams, based on their cyclic performance of the beams and the connection prequalification criteria, the results suggest that 39 of the studied section sizes meet the high ductility requirement, 12 of the studied

section sizes meet the moderate ductility requirement, and only 1 studied section size does not meet the moderate ductility criterium. With the addition of the foam-fill 12 HSS sizes that, when empty, only satisfy the moderate ductility requirement, are now able to maintain 80% of their moment capacity up to 4% drift, changing their ductility rating from moderate to high. Similarly, 2 empty HSS beams that did not meet the moderate ductility requirements were able to do so with the addition of the foam-fill. These results suggest that incorporating a urethane foam-fill in the voids of HSS beam members is a feasible way to increase the number of HSS that can be used in IMFs and SMFs.

Local slenderness limits for empty and foam-filled HSS

Notably, the current AISC Seismic Provisions (2016a) for HSS used as beam members only establish *b/t* limits and do not consider the section's *h/t* ratio. Given the fact that the data presented thus far has shown both the *b/t* and *h/t* ratios to influence the section's cyclic performance, ductility classifications for HSS beam members need to consider both local slenderness ratios, accordingly. The relationship between HSS local slenderness ratios and their moment capacity degradation is explored through contour plots. Fig. IV.10 shows moment capacity degradation contour plots for the empty and foam-filled HSS beams at 2% and 4% drift. These plots are created with a locally weighted smoothing linear regression algorithm. The contour lines represent the moment capacity degradation in decimal percentage and how it relates to the HSS local slenderness ratio. The black circles represent every section that is included in the study. A visual inspection of the contour plots suggests that the *h/t* ratio has a more significant impact on the moment capacity degradation of HSS beams than the *b/t* ratio since the slope of the contour lines is closer to horizontal than vertical. Additionally, comparing the empty and foam-filled plots shows how the presence of the urethane foam-fill shifts the

contour lines upwards, representing a reduction in moment capacity degradation at larger slenderness ratios.

The plots presented in Fig. IV.10 allow an engineer to determine whether an empty or foam-filled HSS beam meets the moderate or high ductility requirements by entering the plot with the section's local slenderness values. However, the current procedure for determining the ductility rating of an HSS beam is based on using an equation to calculate the *b/t* limit as opposed to the graphical approach provided by the contour plots. For this reason, a simplified version of the contour plots is proposed to be more in line with the current approach for determining ductility ratings. Fig. IV.11 shows contour plots created by using a linear polynomial fit and includes the current AISC *b/t* limit as a vertical red line for comparison. This linear simplification results in a loss of accuracy for the plots at the 2% drift ratio (Figs. IV.11a and IV.11c). At this drift ratio, the adjusted R^2 value for the empty and foam-filled HSS is reduced from 0.8721 to 0.6311 and from 0.7229 to 0.3496, respectively, when the linear fit is considered. However, at the 4% drift ratio the loss in accuracy is minimal with the empty and foam-filled adjusted R^2 values going from 0.9295 to 0.9020 and from 0.9172 to 0.8148, respectively. For this reason, the focus of the following analysis will be on the results at the 4% drift ratio which correspond to the highly ductile limit. A graphical approach using Figs. IV.10a and IV.10c is more appropriate to determine whether an HSS beam would meet the moderate ductility requirements.

From the linear contours presented in Fig. IV.11 equations that relate the moment capacity degradation to the HSS local slenderness ratios can be established in the form of Eq. IV.3. The values for *C1*, *C2*, and *C3* for each case are presented in Table IV.3. Comparing the values for *C1* and *C2* (which multiply the *b/t* and *h/t* ratios, respectively) suggests that the value of *h/t* has a larger influence on the moment capacity degradation since the value for *C2* is larger than that for

C1. Further, the addition of the foam-fill has a more significant effect on *C1*. For example, the value for *C1* is reduced by 40.9% when the foam-fill is incorporated. By contrast, *C2* is only reduced by 4.9% when compared to the values for the empty HSS beams.

$$Deg.@X\%\ drift = C1\left(\frac{b}{t}\right) + C2\left(\frac{h}{t}\right) + C3 \qquad \text{(Eq. IV.3)}$$

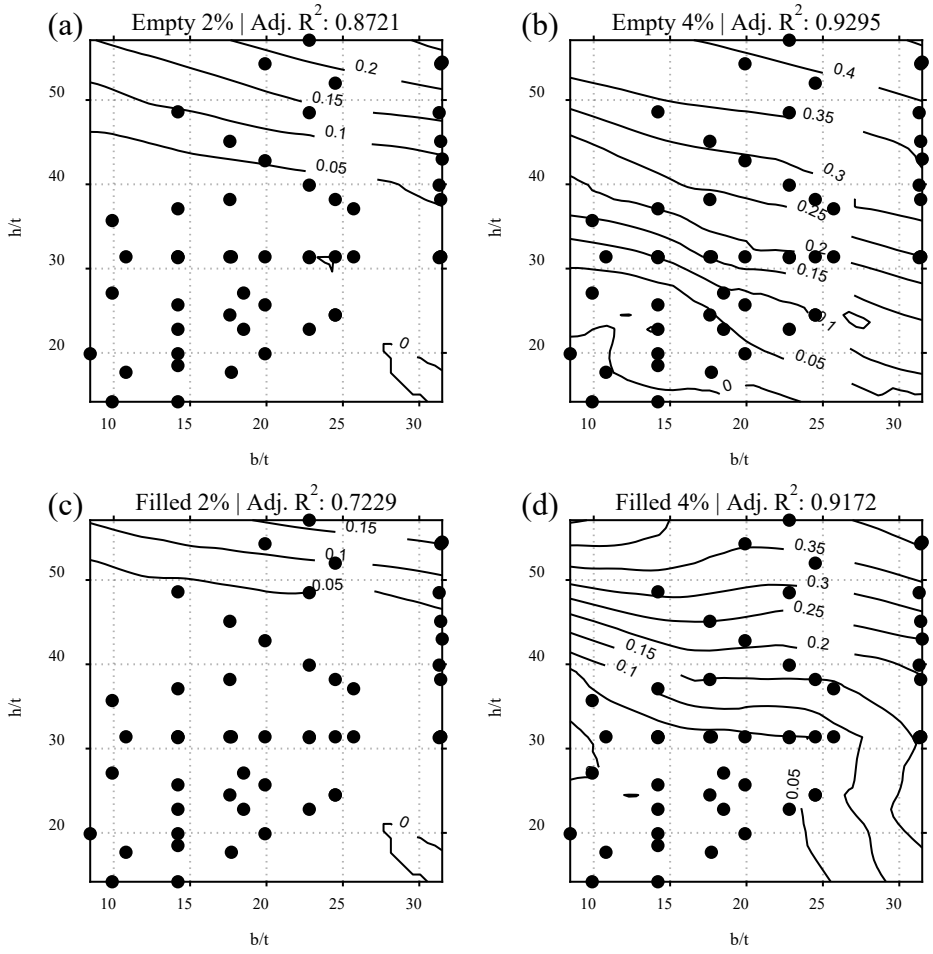

Figure IV.10. Contour plots of moment capacity degradation for (a & b) empty and (c & d) foam-filled HSS beam sections at the (a & c) 2% and (b & d) 4% drift ratio.

The high ductility limit can be determined from Eq. IV.3 by substituting 0.2 (moment capacity degradation) on the left side of the equation and solving for *b/t* or *h/t*. Solving for these

variables and reformatting gives the following equations for the high ductility local slenderness limits:

$$\lambda_{hd,b/t} = A1\sqrt{\frac{E}{R_y F_y}} + B1\left(\frac{h}{t}\right) \quad \text{(Eq. IV.4)}$$

$$\lambda_{hd,h/t} = A2\sqrt{\frac{E}{R_y F_y}} + B2\left(\frac{b}{t}\right) \quad \text{(Eq. IV.5)}$$

where the values for *A1*, *A2*, *B1*, and *B2* are provided for each case in Table IV.4.

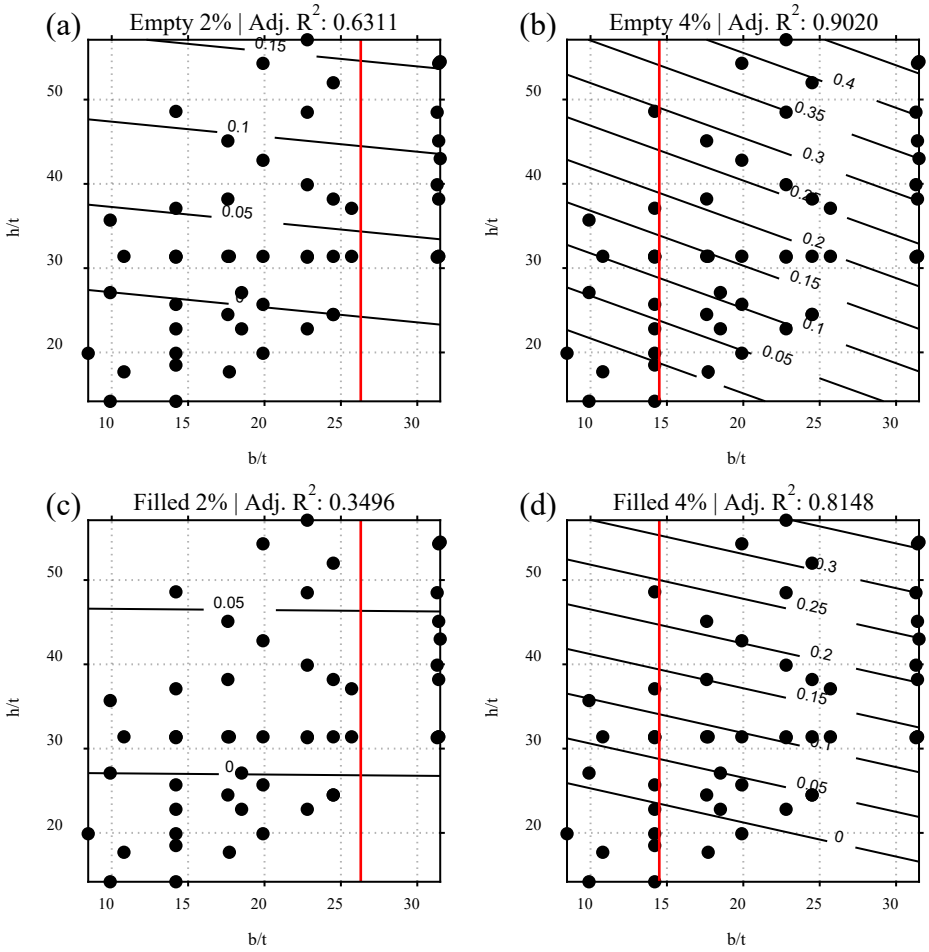

Figure IV.11. Linear contour plots of moment capacity degradation for (a & b) empty and (c & d) foam-filled HSS beam sections at the (a & c) 2% and (b & d) 4% drift ratio. The vertical red line represents the current AISC moderate and high ductility limits.

Eqs. IV.4 and IV.5 can then be used to determine whether an empty HSS beam member would meet the high ductility criteria and if not, whether incorporating the foam-fill would improve its performance enough to be classified as a highly ductile section. An HSS 254.0×203.2×7.9 (HSS 10×8×5/16) (ASTM Gr. B) is used here to demonstrate how to use the proposed equations. This section's nominal local slenderness values are 24.5 and 31.4 for its *b/t* and *h/t* ratios, respectively. Corresponding R_y and F_y values are 1.4 and 317 MPa (46 ksi), respectively. In the case of the empty HSS beam section, entering Eq. IV.5 with the *b/t* value of 24.5 results in an *h/t* limit of 30.1 to be able to be classified as a high ductility section. Given that the section has a larger *h/t* ratio, it does not meet the highly ductile requirements. Following the same procedure, but using the constants for a foam-filled section results in an *h/t* limit of 38.2, indicating that the section can now meet the high ductility moment capacity degradation criterium if the urethane foam-fill is incorporated. As a comparison, using the current AISC ductility limits (Eqs. IV.1 and IV.2) results in a moderate and high ductility *b/t* limit of 25.0 and 13.8 for ASTM Gr. B steel with nominal material properties. With these limits, an HSS 254.0×203.2×7.9 (HSS 10×8×5/16) would be classified as a moderately ductile section.

Table IV.3. Summary of the regression values for the equations established from the moment capacity degradation linear contour plots. Drift ratio: 4%.

HSS	C1	C2	C3
Empty	0.00646	0.00990	-0.27895
Filled	0.00381	0.00942	-0.27630

Table IV.4. Summary of high ductility limit equation constants. Drift ratio: 4%.

HSS	A1	B1	A2	B2
Empty	3.3279	-1.5337	2.1698	-0.6520
Filled	5.6041	-2.4709	2.2680	-0.4047

Conclusions

A computational parametric study is conducted of 52 pairs of empty and urethane foam-filled HSS beams to explore the feasibility of improving the cyclic behavior of these sections by incorporating a foam-fill in the voids of HSS. The study includes a wide variety of HSS sizes with *b/t* and *h/t* ratios that cover values of 8.46 to 31.5 and 14.2 to 57.1, respectively. Previous experimental data is utilized to inform the development of a FE model which is used to expand the available data with regards to the performance of urethane foam-filled HSS beams. The much larger set of data is used to determine the influence of a section's local slenderness ratios on its ability to meet current AISC ductility criteria, which requires beams to maintain 80% of its maximum moment capacity at the 2% and 4% drift ratio to be classified as moderately or highly ductile, respectively, and how incorporating a foam-fill affects this ductility rating. A summary of the findings is presented as follows:

1. To ensure that HSS beams meet the performance criteria to be classified as moderately or highly ductility sections the current AISC standards establish corresponding limits to the section's *b/t* ratio. Notably, the current ductility limits for HSS beams do not consider the effect of the section's *h/t* limit on its ability to meet the ductility requirements for IMFs and SMFs. While the current limits tend to be conservative, they are not capable of accurately predicting the cyclic performance of HSS beams. As an example, take the empty sections HSS 304.8×152.4×6.4 (HSS 12×6×1/4), HSS 254.0×152.4×6.4 (HSS 10×6×1/4), and HSS 203.2×152.4×6.4 (HSS 8×6×1/4) which have the same nominal *b/t* ratio of 22.8 and varying *h/t* ratios of 48.5, 39.9, and 31.3, respectively. While all three of these sections would be classified as moderately ductile under the current limits, they all exhibit significantly different cyclic performance. From the FE results, at the 2% drift

ratio the first section experiences 11.5% moment capacity degradation while the others do not experience any degradation. At 4% drift, they experience 34.3%, 22.9%, and 10.6% moment capacity degradation, respectively. From these results the HSS 203.2×152.4×6.4 (HSS 8×6×1/4) meets the high ductility criterium of maintaining at least 80% moment capacity at the 4% drift ratio, but would still be considered a moderately ductile section based on its *b/t* ratio due to the current limits. Based on the current AISC *b/t* limits, the 52 sections included in the FE study would include 16 that meet the high ductility limit, 26 that meet the moderate ductility limit, and 10 that have larger *b/t* ratios than the moderate ductility limit. By comparison, using the FE data and moment capacity degradation at the 4% and 2% drift ratios, the ratings change to having 27 sections that meet the high ductility requirement, 22 that meet the moderate ductility requirement, and 3 that do not meet the moderate ductility criterium.

2. Incorporating a urethane foam-fill in the voids of HSS beams reduces the amount of moment capacity degradation that HSS beams experience. On average, at the 2% drift ratio the empty and foam-filled beams experienced 3.9% and 1.6% moment capacity degradation, respectively. At the 4% drift ratio the empty beams experienced 18.3% moment capacity degradation, while the foam-filled HSS experienced 11.5%. The amount of moment capacity degradation that an HSS beam experiences is influenced by both of its local slenderness ratios (*b/t* and *h/t*), but the addition of the foam-fill reduces the impact of larger local slenderness values.
3. The addition of the urethane foam-fill can significantly improve the cyclic behavior of an HSS beam, enough to change its ductility rating in certain cases. Based on their cyclic performance the 52 foam-filled HSS would include 39 sections that meet the high

ductility requirement, 12 that meet the moderate ductility requirement, and 1 that does not meet the moderate ductility criterium. Comparatively, in the case of the empty HSS these numbers would be 27, 22, and 3, respectively. These results suggest that incorporating a urethane foam-fill is a feasible approach to increase the number of HSS that can be used as beams in IMFs and SMFs.

4. The influence of HSS local slenderness ratios and its moment capacity degradation at 2% and 4% drift is explored through contour plots. A visual inspection of the contours suggests that while both the *b/t* and *h/t* ratios influence the behavior of the beams, the *h/t* ratio has a larger effect on the section's moment capacity degradation. A comparison of the contour lines between empty and foam-filled sections shows the contours being shifted upwards once the foam-fill is introduced, showing that sections with the same slenderness ratio experience reduced moment capacity degradation when compared to their empty versions. An engineer can enter these plots with the HSS's local slenderness ratios to graphically determine whether it would meet the moderate or high ductility performance requirements for use as a beam section in a seismic moment frame.
5. An alternative linear fit is presented that allows for determining an equation to more easily calculate whether an HSS beam (empty or foam-filled) meets a certain ductility rating. The loss in accuracy of the contour lines due to the linear fit is significant in the case of the plots for moment capacity degradation at 2% drift (corresponding to the moderate ductility limit). For this reason, equations were only developed for the high ductility limit given that in this case the linear contour lines are in good agreement with the original contours. A graphical approach using the original contour lines is more appropriate to determine whether a section meets the moderate ductility limit.

6. The equations developed for the empty and foam-filled HSS beams consider the section's *b/t* and *h/t* ratios to reflect the results from the FE study. A comparison of the factors that multiply the corresponding local slenderness ratios shows that the *h/t* ratio has a larger influence on the behavior of the section given that it is multiplied by a larger number. Further, the addition of the foam-fill has the effect of reducing the factor that multiplies the *b/t* ratio by 40.9%, while only reducing the factor that multiplies the *h/t* ratio by 4.9%. These results suggest that incorporating the urethane foam-fill improves the cyclic behavior of HSS beams largely by reducing the influence that the *b/t* ratio has on the section's performance.

CHAPTER V

Finite Element Analysis of HSS-Based Seismic Collar Connections under Cyclic Loads

Introduction

Hollow structural sections (HSS) or tubes can provide beneficial properties for seismic applications but are often overlooked in favor of wide flange sections in seismic moment frame systems because of the added difficulty in connecting them due to their closed shape. The benefits of HSS members can be attributed to their high strength to weight ratio (limited seismic weight), excellent torsional resistance (reduced lateral bracing requirements and less interaction between global and local limit states), and smooth surfaces (architecturally pleasing and potential for modular construction applications). To fully take advantage of these properties in low-rise tube-based seismic moment frame systems, moment resisting connections need to be developed and understood to ensure that stable and ductile behavior is obtained under large cyclic loads, while also addressing ease of fabrication/construction and the economy of the connection.

The 1994 Northridge (United States) and 1995 Hyogoken-Nanbu (Japan) earthquakes led to an extensive study and reevaluation of seismic moment frame systems (Nakashima et al. 1998). As a result, current design methodologies for steel moment frames require the majority of the inelastic behavior to occur at the ends of the beam member or at the base of the column, which represents the fuse in the system (AISC 2016a). All other elements of the seismic moment frame are expected to remain elastic. As a result, most seismic provisions regarding moment frame systems focus on detailing requirements to ensure a stable and ductile behavior given this desired

mechanism. For a tube-based seismic moment frame to then be classified as an intermediate (IMF) or special (SMF) moment frame the HSS beam member must be able to undergo large inelastic deformations while maintaining 80 percent of the plastic moment capacity of the beam out to interstory drift levels of 2% or 4%, respectively (AISC 2016a). The connection plays a key role in ensuring that these requirements can be met.

The viability of HSS-to-HSS moment connections was originally shown in studies of Vierendeel truss systems (Jubb and Redwood 1966). Korol et al. (1977) further showed that when the connecting tubes have unequal widths in T-connections, reinforcement of the connection through chord flange stiffeners, haunches, or truncated pyramids is necessary in order to avoid transferring forces directly to the flexible face of an HSS member. Similarly, seismic moment frame connections between wide-flange beams and HSS columns often utilize internal and external diaphragms to transfer loads directly to the stiffer sidewalls of the HSS columns rather than through the flexible face (Kamba and Tabuchi 1995; Kurobane et al. 2004). Fadden and McCormick (2014b) and Fadden et al. (2015) used a similar concept to show that HSS-to-HSS or tube-based moment connections are viable for application in seismic moment frame systems provided the connection is reinforced with either a through-plate or external diaphragm plate. These tube-based connections allow for the full advantages of the HSS members to be realized, but may be limited in application due to the need for the reinforcing plates which adds to the complexity and cost of the connections.

Two exterior tube-based collar connection configurations were previously studied to assess their suitability for seismic applications and determine their performance under large cyclic deformations (Wei and McCormick 2017, Wei 2017). Collar connections were chosen to address the need to develop HSS-to-HSS seismic moment connections that do not require extensive field

welding associated with previously studied through-plate or external diaphragm plate connections (Fadden and McCormick 2014b, Fadden et al. 2015). The full-scale tests of the HSS-based collar connections examined the connections' hysteretic behavior, the influence of beam endplate stiffeners on connection performance, and the flow of forces through the connection (Wei and McCormick 2017, Wei 2017). The findings of these tests suggest that HSS-based collar connections can provide adequate stability and ductility to meet the SMF requirements of the AISC Seismic Provisions (2016a), i.e., maintain 80% of the plastic moment capacity of the beam to a story drift angle of 0.04 rad.

To further explore the concept of the HSS-based collar connection and further refine its design, a finite element model of the connection is created and calibrated to the experimental results. This high-fidelity model is used to explore the influence of the beam endplate thickness and the weld configuration on the connection's performance to obtain valuable insight into optimizing its design for seismic loads. The finite element parametric study demonstrates that further improvements in weld configurations can lead to a more efficient and economical connection. Overall, the results suggest the viability of HSS-based collar connections in low-rise seismic moment frame systems.

HSS-Based Collar Connection

Concept

Although previous studies have shown that HSS-based connections are viable under seismic loads with the use of through-plates or external diaphragm plates (Fadden et al. 2015), these connections require a significant amount of welding in the field including complete joint penetration (CJP) welds that can be costly, time consuming and prone to poor quality depending on the environmental conditions and access to the connection. The HSS-based collar connection

aims to limit field welding and improve construction efficiency. A schematic view of the collar connection is provided in Fig. V.1 where the column is a square HSS and the beam is a rectangular HSS.

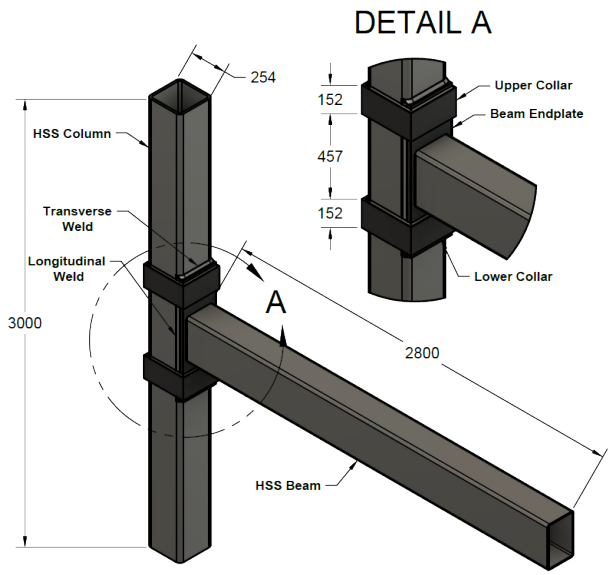

Figure V.1. Schematic of the HSS-based collar connection. (Units: mm)

One means of improving weld quality control and reducing cost is by welding the endplate to the beam and welding the collars together in the shop. The assembly procedure is shown in Fig. V.2. To improve construction speed, the lower collar also is shop welded to the column, leaving a gap between the column face and collar where the beam endplate can be inserted in the field. Once the column is erected in the field, the HSS beam with the endplate already attached is lowered into the gap between the lower collar and column face. The upper collar can then be slipped onto the top of the column and lowered in place to secure the top of the beam endplate to the column. Fillet welds are then used to secure the collar to the beam endplate and RHS column. As a result of the previous shop welding, only filled welds or partial groove welds are needed in the field to attach the HSS beam to the HSS column. A complete description of the welds required throughout the connection is presented in Fig. V.3. Proper tolerances in the design and

construction process are needed to ensure the endplate fits correctly between the collar and column face. Proper sizing of the connection elements is critical to avoid undesirable behavior, such as brittle weld failure or excessive localized deformation outside the HSS beam. The desired mechanism requires the majority of deformation to occur in the HSS beam member with contributions to the inelastic deformation from the collar or beam endplate to ensure a stable and predictable hysteretic behavior typical of seismic moment frame systems.

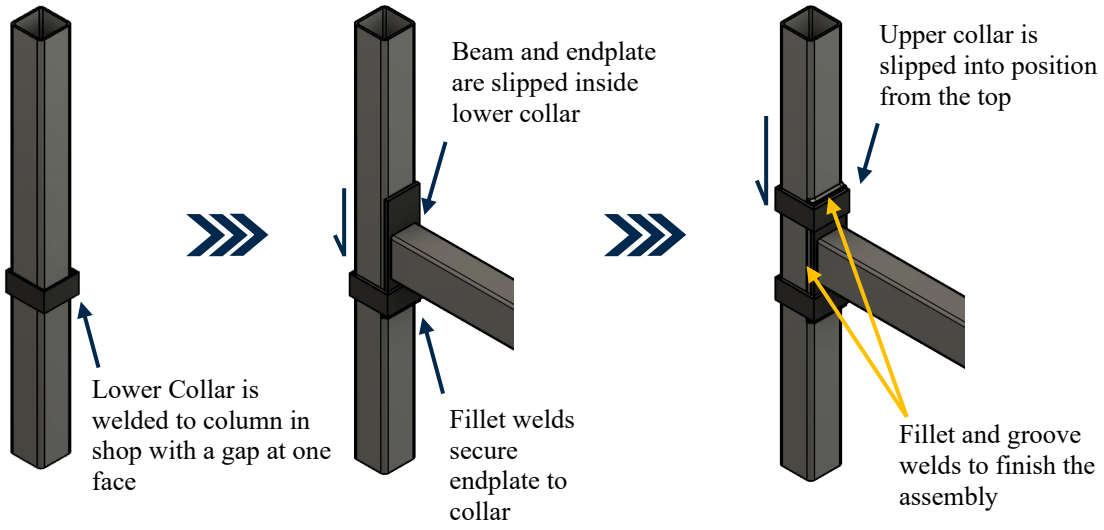

Figure V.2. Collar connection field assembly procedure.

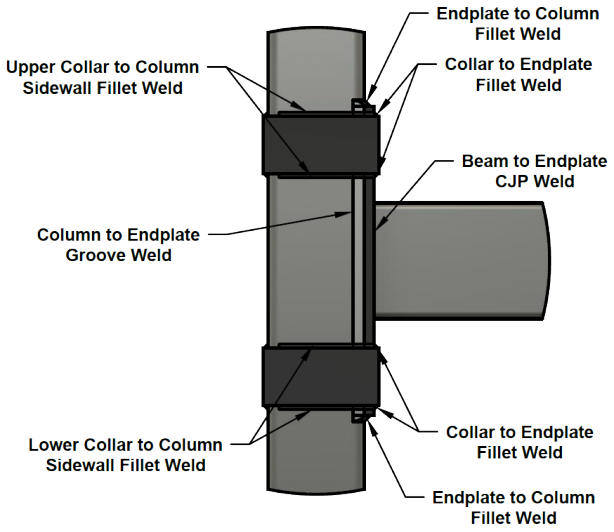

Figure V.3. Required welds for the HSS-based collar connection without beam endplate stiffeners.

Configuration

Details of the two previously tested HSS-based collar connections are provided below (Wei and McCormick 2017, Wei 2017) in order to provide details necessary to develop the finite element model to further explore the HSS-based collar connections design and provide the data necessary to calibrate and validate the finite element model. Further details in regards to these tests can be found in Wei and McCormick (2017) and Wei (2017). The two connections, one with beam endplate stiffeners and one without beam endplate stiffeners, were developed to represent an exterior seismic moment connection in a low-rise steel moment frame with 3.7 m (146 in.) floor heights and 6.4 m (252 in.) bay widths. The connection subassembly had a column length of 3.7 m (146 in.), which represented the distance between the inflection points of adjacent floors. The beam length spanned half the bay width, 3.2 m (126 in.), measured from the column centerline to the centerline of the applied load at the end of the beam. This length represented the inflection point along the beam under lateral load. A picture of each of the

connections is shown in Fig. V.4 where the connection subassembly is rotated 90 degrees so that the beam extends vertically, and the column is horizontal.

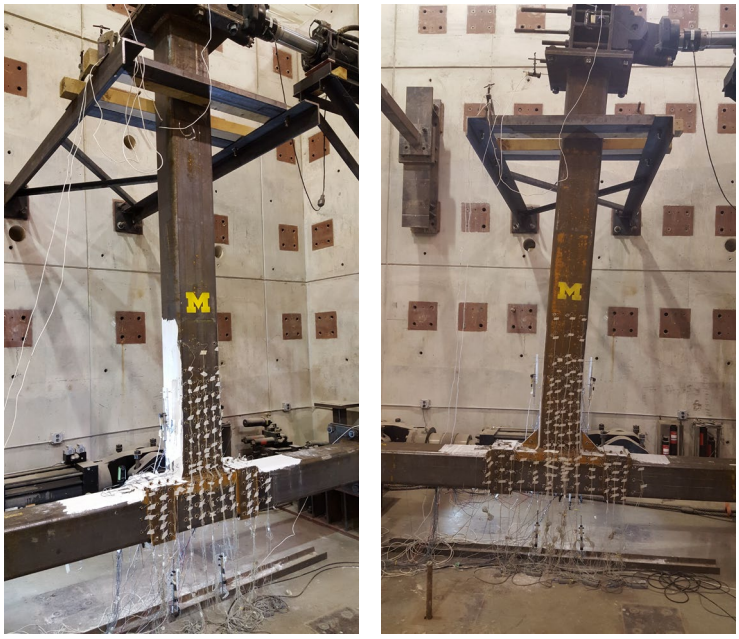

(a) (b)

Figure V.4. Tube-based collar connection experimental test setup (a) without and (b) with beam endplate stiffeners.

Details of both connection configurations, with the stiffened beam endplate and without stiffeners, are shown in Fig. V.5. An HSS 254×254×15.9 (HSS 10x10x5/8) column (ASTM A1085) was utilized for both connections which had nominal width-thickness, b/t, and depth-thickness, h/t, ratios of 13.0. The column size was chosen because it met the highly ductile seismic compactness criteria specified by the AISC Seismic Provisions (2016a), which was 14.0 assuming an elastic modulus of 200 GPa (29,000 ksi), a yield strength of 345 MPa (50 ksi), and a ratio of expected to nominal yield strength of 1.25. Highly ductile columns are required for SMF, while moderately ductile columns are allowed for IMF systems (AISC 2016a). The b/t and h/t values also were measured (Table V.1) and found to still meet the highly ductile requirements

with values less than 1.5% above of the nominal specified value. Other measured values, including the yield strength, F_y, and plastic section modulus, Z_{meas} also are provided in Table V.1. The yield strength was based on the average yield strength from coupon specimens taken from the flats of the HSS member used as the column.

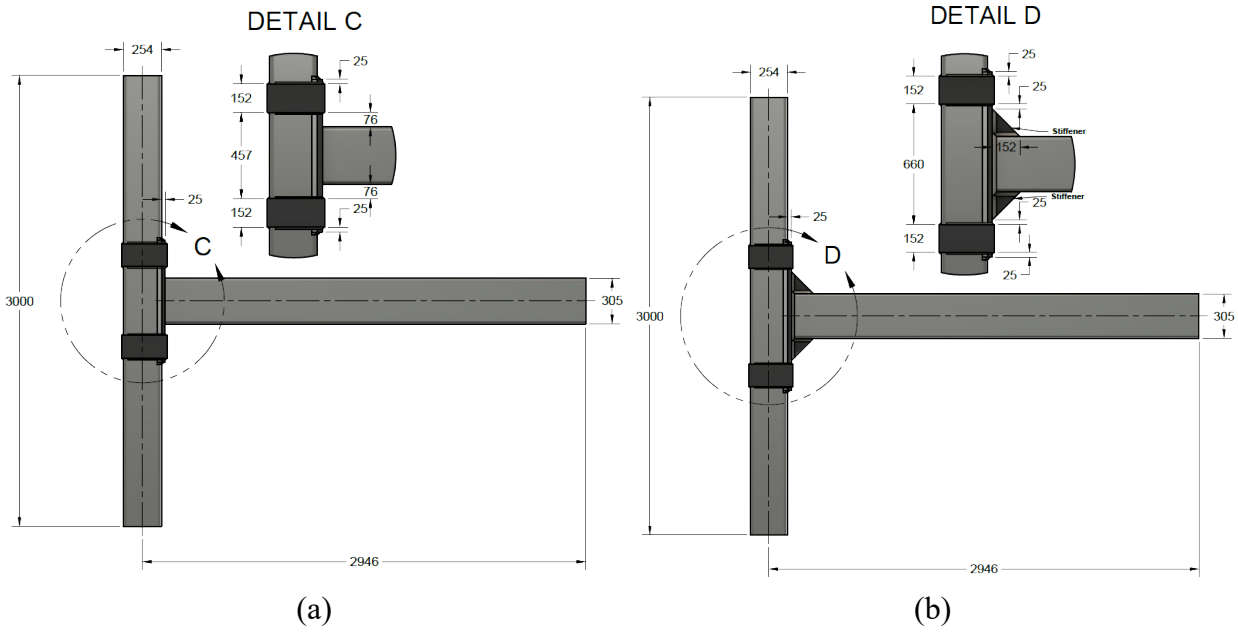

Figure V.5. Elevation view of the tube-based collar connection (a) without and (b) with beam endplate stiffeners. (Units: mm)

Given that the beam member represented the "fuse" or energy dissipating element in the moment frame, it was important that the beam met the highly ductile member criteria so as to avoid local buckling prior to reaching the plastic moment capacity of the beam and to maintain 80% of the plastic moment capacity out to drift levels of either 0.04 rad. or 0.02 rad. for SMF and IMF, respectively (AISC 2016a). An HSS 304.8×203.2×9.5 (HSS 12×8×3/8) (ASTM A500 Gr. B/C) was used for the beam member whose nominal local slenderness ratios met the SMF ductility criteria for HSS in bending based on the findings of Fadden and McCormick (2012) and the results presented in Chapter IV of this document. The measured b/t and h/t were

approximately 15.6% below the nominal values further suggesting their ability to resist local buckling. The yield strength for the HSS beam is based on the average yield strength from coupon specimens taken from the flats of the HSS member used for the beam.

Table V.1. Measured section properties of the HSS members (metric).

HSS	Nominal			Measured				
	b/t	h/t	$Z_{x,nom}\times10^3$ (mm^3)	$(b/t)_{meas}$	$(h/t)_{meas}$	$F_{y,meas}$ (MPa)	$Z_{x,meas}\times10^3$ (mm^3)	$M_{p,meas}$ (kN-m)
304.8×203.2×9.5	19.9	31.4	869	17.2	27.2	395	911	360
254.0×254.0×15.9	13.0	13.0	1200	12.8	13.2	418	1198	508

Table V.1a. Measured section properties of the HSS members (US customary units).

HSS	Nominal			Measured				
	b/t	h/t	$Z_{x,nom}\times10^3$ (in^3)	$(b/t)_{meas}$	$(h/t)_{meas}$	$F_{y,meas}$ (ksi)	$Z_{x,meas}\times10^3$ (in^3)	$M_{p,meas}$ (kip-ft)
12×8×3/8	19.9	31.4	53.0	17.2	27.2	57.3	55.6	266
10×10×5/8	13.0	13.0	73.2	12.8	13.2	60.6	73.1	375

The beam width to column width ratio, β, often controls how the load is transferred through HSS connections due to the fact that the beam member attaches to the flexible face of the column. For the HSS-based collar connection, β is 0.8 suggesting that column face deformation might occur. However, for this connection, the width of the endplate, which was equal to the width of the column, allowed forces to flow from the beam to the stiffer column sidewalls either through the base plate directly or through the collars. As a result, minimal deformation of the column face was seen.

The collar, endplate and stiffeners were made of ASTM A36 steel. The actual material properties of these plates were not measured as these components are designed to remain elastic. The collars were constructed by welding together four 12.7 mm (0.5 in.) thick plates to make a hollow rectangle with inner and outer dimensions of 254 mm (10 in.) by 279 mm (11 in.) and 279 mm (11 in.) by 305 mm (12 in.), respectively. The depth of each collar was 152 mm (6 in.).

The collars were connected to the HSS column and the 25 mm (1 in.) thick endplate by 10 mm (3/8 in.) fillet welds around both ends of the collar. The collars were positioned to allow the beam endplate to extend 25 mm (1 in.) past them to provide room for a transverse fillet weld between the collar and endplate. A 16 mm (1/4 in.) transverse fillet weld also connected the end of the endplate to the column face.

In the connection without stiffeners, the endplate had a length of 813 mm (32 in.), which left 76 mm (3 in.) of separation between the beam face and each collar. The beam was connected to the endplate using a prequalified CJP groove weld, as specified in AWS D1.1 (2010). For the connection with the stiffened endplate, a 1016 mm (40 in.) long endplate was used and two 19 mm (0.75 in.) thick triangular stiffener plates with 152 mm (6 in.) legs were placed between the endplate and HSS beam flange. The use of the stiffeners allowed for greater control over the load path through the connection. Instead of a CJP weld, 24 mm (1 in.) fillet welds were adopted to connect the HSS beam to the stiffeners and beam endplate. In order to carry the shear in the connection, a groove weld, filled flush, was specified between the beam endplate and column corners over the full length of the endplate. The selection of collar and endplate dimensions was based on the findings of a previous finite element study conducted by Fadden et al. (2015).

Finite Element Study

The experimental tests of the two collar connections showed the viability of the connection configuration in terms of its ability to meet IMF and SMF requirements and form a stable plastic hinge in the beam member (Wei and McCormick 2017, Wei 2017). However, further analysis of the connection is needed in order to explore the influence of the weld details and beam endplate thickness. The weld configuration is explored in order to determine if further economy can be saved through reduced welding demands in the field. The influence of the beam endplate

thickness is considered given that deformation of the beam endplate contributed to some of the plastic rotation in the experimental collar connection without stiffeners. Utilizing a thinner endplate may provide for a more balanced connection in regards to contributions to the inelastic behavior or a thicker endplate may provide an alternative to using beam endplate stiffeners. Since the experimental results do not show a significant difference between the global connection behavior of the collar connection without and with beam endplate stiffeners, the un-stiffened variant of the connection is the focus of the finite element analyses. The material models and overall modeling approach are calibrated based on the experimental findings (Wei and McCormick 2017, Wei 2017) for the collar connection without stiffeners and then validated against the experimental results (Wei and McCormick 2017, Wei 2017) for the collar connection with stiffeners.

Finite element model

To further study the cyclic behavior of the collar connections, a finite element model is developed that considers the location of different welds throughout the connection, as well as contact interactions between the beam, collars, and column. These interactions are key to understanding the flow of forces through the collar connection, as it is expected that a significant portion of the loads are transferred through bearing on the column, as well as tension on the collars. Fracture and crack propagation are not included in the finite element model, but the possibility of fracture in the plates or welds is assessed by considering the stresses these experience. The models are developed in Abaqus CAE (version 2017) and are a complete representation of the experimentally tested connections (Fig. V.6). The fillet and groove welds are explicitly accounted for in the model and tie constraints are applied between each weld face and its corresponding bonded surface in the collar connection. This approach aims to simulate

the actual load path present in the connection. The CJP weld between the beam and endplate of the unstiffened subassembly is the only weld not simulated with this approach, instead a tie constraint is applied directly between the corresponding elements at the end of the HSS beam and the surface of the endplate.

Steel on steel contact properties are specified to account for interactions between the various parts in the collar connection. Tangential and normal behavior are described respectively by a penalty contact interaction with the friction coefficient taken as 0.5 and hard contact with allowance for separation. Surface to surface contact interactions are applied between the beam endplate and inner collar region, beam endplate and outer column face, and inner collar region and outer column faces. The applied interactions ensure proper contact occurs and prevent element pass through between the various components of the connection.

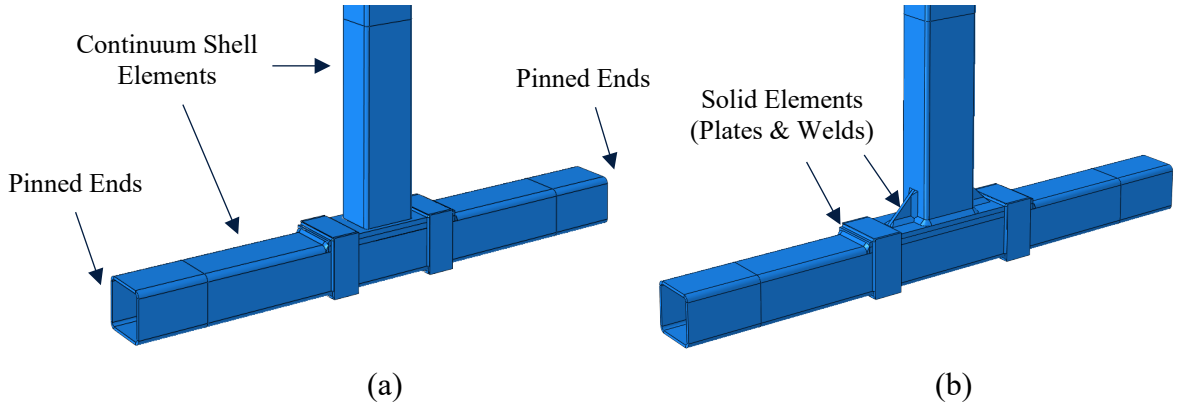

Figure V.6. Finite element model of the collar connection (a) without and (b) with beam endplate stiffeners.

The HSS beam and column are modeled with SC8R elements (8-node quadrilateral general purpose continuum shells, reduced integration with hourglass control, and finite membrane strains) with only one element used through the thickness of the wall. C3D8R (8-node linear brick with reduced integration and hourglass control) and C3D6 (6-node linear triangular prism)

elements are used to model the welds and plates that make up the other elements of the collar connection. The mesh consists of a combination of 12.7 mm (0.5 in.) and 19.1 mm (0.75 in.) element sizes for the denser and coarser mesh densities, respectively, which provides good computational efficiency and accuracy. The denser mesh region extends out approximately 1020 mm (40 in.) from the base of the beam and 1120 mm (44 in.) in both directions from the center of the column towards its ends in order to better capture the stress fields where significant inelastic deformation is expected. The boundary conditions differ slightly from the experimental setup. Consistent with the experimental test, both column ends are pinned to a reference point located 330 mm (13 in.) away from each end. Unlike the experimental test, the beam displacements are applied directly at the end of the beam, whereas they are applied 279 mm (11 in.) further away in the experimental tests due to the finite size of the hydraulic actuator clevis and connection. As a result, the applied displacements for the loading protocol are slightly different for the finite element study to ensure that the same rotation levels are obtained during cycling.

In order to accurately capture local buckling within the connection, namely in the HSS beam, an eigenvalue buckling analysis is first conducted to obtain the most probable shape of the local buckle within the connection. A combination of the resulting first two buckled mode shapes is chosen as the initial member imperfection. These two modes are equal in magnitude, opposite in direction and primarily act on opposing faces of the HSS beam. An imperfection magnitude of 0.01 times the smaller HSS dimension is applied, which maintains a reasonable level of initial imperfection that meets the manufacturing tolerances for HSS members (ASTM 2018). The directions of the mode shapes are adjusted to match the experimentally observed buckled shape.

An isotropic hardening model based on uniaxial strain hardening data is used to replicate the behavior of both the welds and the plates. Recorded yield and tensile stress values are 570 MPa (82.7 ksi) and 698 MPa (101 ksi) for the weld material, and 318 MPa (46.1 ksi) and 555 MPa (80.5 ksi) for the plate material, respectively, based on tensile coupon tests. The measured Young's modulus is 196 GPa (28,427 ksi) for the welds and 208 GPa (30,168 ksi) for the plates. Combined nonlinear kinematic and isotropic hardening material parameters are used to model the behavior of the HSS beam and column (Table V.2). The kinematic parameters are obtained from fitting tensile coupon test data to a kinematic law which determines the back stress tensor by considering an initial kinematic hardening modulus C, and the rate γ at which it decreases with increasing plastic deformation. Q_∞ represents the maximum change in the yield surface size and b defines the rate at which it changes (Maximov et al. 2008). The resulting kinematic parameters from multiple coupon tests are averaged to obtain those used in the finite element study. Isotropic parameters are obtained through an iterative approach by comparing the resulting moment-rotation behavior of the finite element model to the experimental results and making adjustments until the behavior is comparable. The flats and corners of the HSS members are partitioned and separate material properties are applied to each to account for the effects of cold-working during the manufacturing of the HSS members. These effects result in the corners of the HSS exhibiting a higher yield stress, but lower ductility, when compared to the flats of the member. Further discussion on the influence of cold-working on the material properties around the perimeter of an HSS can be found in Fadden and McCormick (2014a). The corner material is applied up to a distance of two times the wall thickness from the outside edge of the HSS.

Table V.2. Kinematic and Isotropic Hardening Parameters used for the finite element model.

HSS Region	Young's Modulus (GPa | ksi)	F_y (MPa | ksi)	Kinematic Hardening Parameters		Isotropic Hardening Parameters	
			C (MPa | ksi)	γ	Q_∞ (MPa | ksi)	b
Beam Corners	209 | 30255	518 | 75.1	13045 | 1892	216	97.4 | 14.1	10
Beam Flats	201 | 29120	395 | 57.3	4343 | 630	33.9	212 | 30.7	10
Column Corners	234 | 33953	570 | 82.6	9973 | 1447	275	71.7 | 10.4	10
Column Flats	192 | 27914	418 | 60.6	1167 | 169	11.1	150 | 21.7	10

Model calibration and validation

To ensure the accuracy of the finite element model, the behavior of the model is compared to the experimental results for the collar connection without stiffeners, to which it was calibrated, and for the collar connection with beam endplate stiffeners. The comparison of the hysteretic behavior is shown in Fig. V.7. The finite element model is able to capture the behavior that was seen during the experimental test, particularly during the early cycles. Overall, the finite element models are able to accurately capture the moment capacity for a given cycle, initial stiffness, deformation behavior (local buckling), and degradation of the moment capacity with continued cycling. At rotations of 0.04 rad., the difference in the maximum moment resistance between the experimental and computational curves is below 5% for both connections. This difference increases with an increase in rotation, but remains reasonable and on the conservative side. As rotation levels increase to 0.06 rad., the finite element model under predicts the capacity by an average of 14.9% and 12.7% for the collar connection without and with beam endplate stiffeners, respectively. Although fracture is not considered in the model, the difference in predicted capacity stays under 8.0% during the first two cycles to 0.08 rad. for both connections. The maximum normalized moment capacities are also similar, 1.25 and 1.28 for the experimental compared to 1.27 and 1.32 for the computational model of the unstiffened and stiffened

connections, respectively. The difference in moment capacity at 0.04 rad. is small enough to give a good level of certainty when determining whether the finite element models meet the requirements for SMF systems.

The secant stiffness and energy dissipation obtained from the finite element models also is compared to the experimental findings to ensure that the models can accurately capture the degradation of the stiffness of the connections and energy dissipated through inelastic deformation. For the collar connection without beam endplate stiffeners, the finite element model accurately predicts the initial stiffness of the connection and the secant stiffness at 0.04 rad. is within 10.0%. At the 0.06 rad. rotation, the model is less stiff than the experimental connection by approximately 12.1%. For the case of the collar connection with beam endplate stiffeners, which is used for validation of the finite element model, the model over predicts the elastic stiffness by 9.6% and the secant stiffness at 0.04 rad. by 16.2%. Although these values are larger than that observed for the collar connection without stiffeners that was used for calibration purposes, the results indicate the finite element model is capable of capturing the overall system deterioration over large interstory drift cycles.

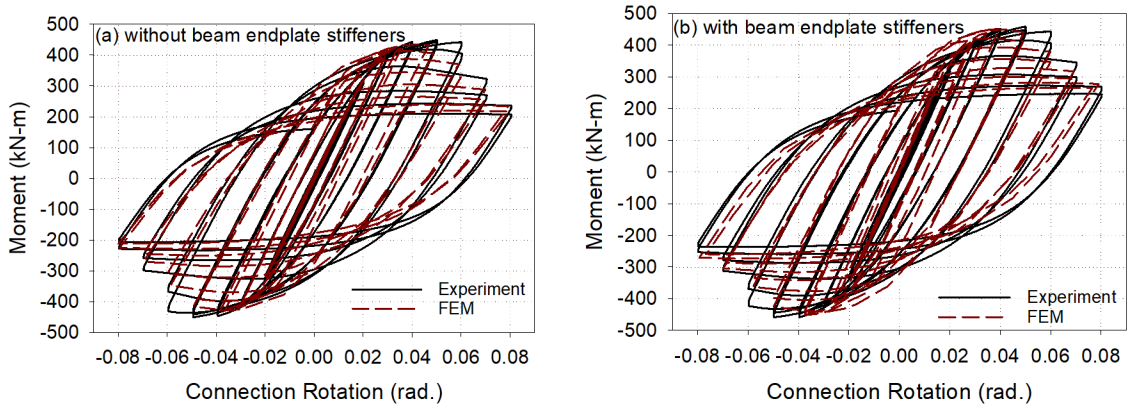

Figure V.7. Comparison of the moment-rotation hysteresis for the experimental and finite element model of the tube-based connection (a) without beam endplate stiffeners and (b) with beam endplate stiffeners.

A similar consistency between the results from the finite element model and experimental tests is found when evaluating the cumulative energy dissipation. For the collar connection without stiffeners, the cumulative energy dissipation for a given cycle obtained from the finite element model remains within 11% of the experimental results. Even better results are found for the collar connection with beam endplate stiffeners where the largest difference between the finite element model and experimental results at the end of a given cycle level is 4.5%. These results are expected as the hysteretic behavior and deformation modes obtained from the finite element models compare well with the experimental findings presented previously.

Parametric study

A total of 18 different variations of the collar connection without beam endplate stiffeners are considered and defined in Table V.3. Three different beam endplate thicknesses are studied, 19.05 mm (0.75 in.), 25.4 mm (1 in.), and 31.75 mm (1.25 in.), in order to evaluate the role it plays in determining the deformation mechanism for the connection. Since the experimentally tested collar connection without stiffeners shows some inelastic deformation of the beam endplate, both a thinner and thicker plate are utilized to try to optimize the behavior and potentially promote a more balanced connection behavior rather than having almost all of the inelastic behavior occurring in the beam member.

Table V.3. Finite element model parametric study variations.

Model	Transverse Weld Length (mm | in.)	Longitudinal Weld Length (mm | in.)	Endplate Thickness (mm | in.)
FL_FT_1	254 | 10	813 | 32	25.4 | 1
HL_FT_1	254 | 10	406 | 16	25.4 | 1
NL_FT_1	254 | 10	0	25.4 | 1
FL_NT_1	0	813 | 32	25.4 | 1
HL_NT_1	0	406 | 16	25.4 | 1
NL_NT_1	0	0	25.4 | 1
FL_FT_2	254 | 10	813 | 32	19.05 | 0.75
HL_FT_2	254 | 10	406 | 16	19.05 | 0.75
NL_FT_2	254 | 10	0	19.05 | 0.75
FL_NT_2	0	813 | 32	19.05 | 0.75
HL_NT_2	0	406 | 16	19.05 | 0.75
NL_NT_2	0	0	19.05 | 0.75
FL_FT_3	254 | 10	813 | 32	31.75 | 1.25
HL_FT_3	254 | 10	406 | 16	31.75 | 1.25
NL_FT_3	254 | 10	0	31.75 | 1.25
FL_NT_3	0	813 | 32	31.75 | 1.25
HL_NT_3	0	406 | 16	31.75 | 1.25
NL_NT_3	0	0	31.75 | 1.25

The welds provide another opportunity to optimize and economize the connection. The different types of weld configurations that are considered are presented in Fig. V.8. Since very little influence from the shear forces are observed in the experimental tests, the length of the groove weld between the endplate and HSS column corners (referred to as the longitudinal weld) is varied between a full-length weld spanning the length of the endplate (same as the tested collar connections), a half-length weld spanning 229 mm (9 in.) (centered along the beam endplate), and no longitudinal weld. A reduction of the length of this groove weld or the removal of the requirement for this weld can lead to substantial savings given the amount of weld material required to be deposited. The use of a transverse weld connecting the end of the beam endplate to the HSS column face also is considered. In the experimental tests this transverse weld is present, but there is potentially limited force transfer through this weld given that the collars are instead

expected to take a majority of the load in this region through tension. As a result, the need for this weld is explored in order to determine if the collars can be better engaged and utilized within the connection design. All of the connections in the parametric study utilized the finite element model that is calibrated and validated against the experimental tests. They undergo the same loading protocol that is used for the experimental tests.

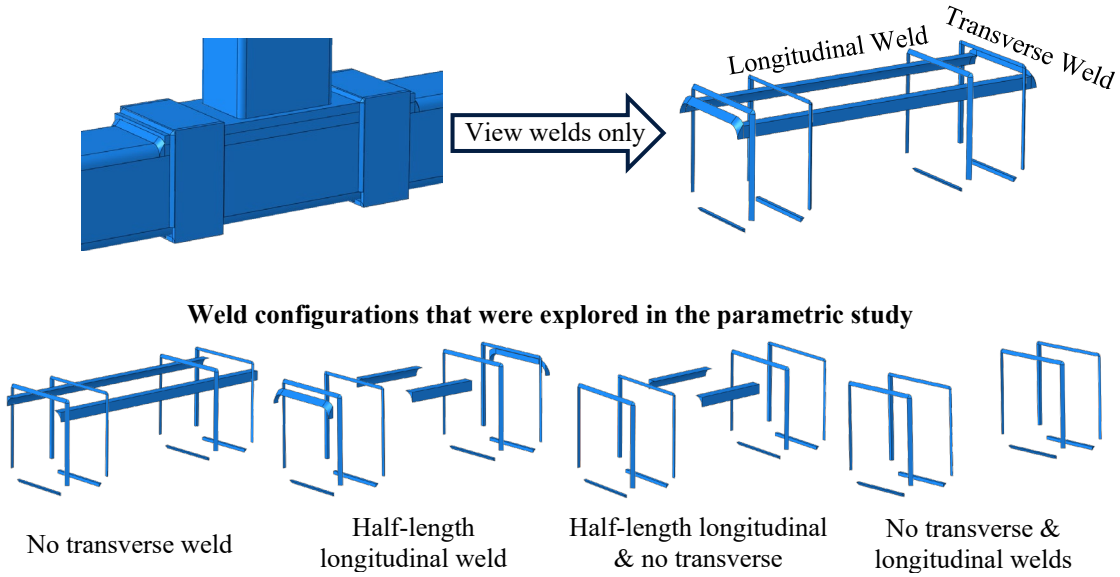

Figure V.8. Different weld configurations that are considered in the parametric study.

Influence of the longitudinal groove weld

All six models that feature a full-length longitudinal weld provide a similar hysteretic behavior to the experimentally tested connections, regardless of the endplate thickness and transverse weld configuration. Although having the full-length weld leads to good hysteretic behavior, the finite element model indicates that most of the components making up the collar connection are not being fully utilized in transferring the loads through the connection. Comparing the stress distribution in connection FL_FT_1 with a full-length longitudinal weld and connection HL_FT_1 with a half-length longitudinal weld, where both connections have an endplate thickness of 25.4 mm (1 in.) and feature a transverse weld (Fig. V.9), the collar

connection with the half-length longitudinal weld better utilizes the connection components including the collars, beam endplate and panel zone to sustain the applied loads. This distribution results in a more desirable connection performance, in which the collars are actively participating in resisting the load. The influence of this distribution is apparent in a comparison of the hysteretic behavior for connections with different longitudinal weld configurations (Fig. V.10). The half-length longitudinal weld cases exhibit 10%, 8.6%, and 4.3% less moment capacity degradation on average by the second 0.06 rad. cycle for endplate thicknesses of 19.05 mm (0.75 in.), 25.4 mm (1 in.), and 31.75 mm (1.25 in.), respectively. All cases that have either a full or half-length weld do not experience any moment degradation by the first or second 0.04 rad. cycle as the maximum moment capacity of the subassembly is usually reached around the 0.05 rad cycle, consistent with the experimental results. Thus, these cases also meet the requirements for SMF.

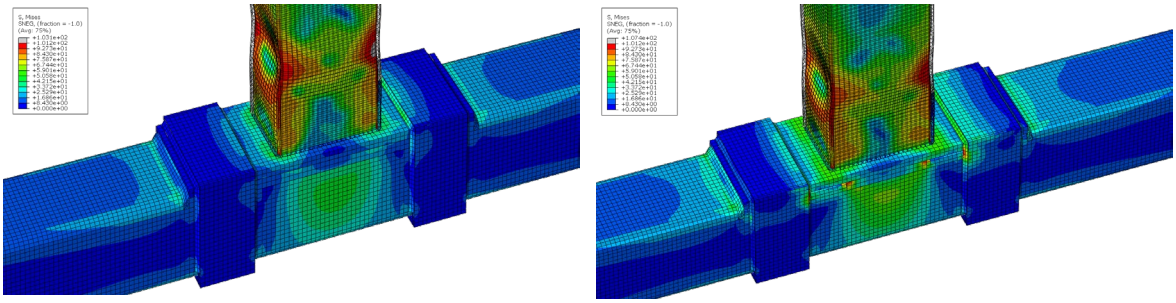

(a) (b)

Figure V.9. Mises stress distribution for the unstiffened tube-based collar connection model with a (a) full-length and (b) half-length longitudinal weld.

Reducing the length of the longitudinal weld to half also has the effect of increasing the overall stresses present in the endplate, panel zone, and weld. The higher stresses observed in the endplate and panel zone are not enough to cause concerns of excessive yielding in these parts. For all of the half-length cases, the maximum stresses at the ends of the longitudinal weld reach

the tensile strength of the material during the 0.04 or 0.05 rad. cycles. These stresses are taken from the integration points at the ends of the weld. Due to the nature of the applied material model, the recorded stresses never exceed the specified tensile strength as it assumes a perfectly plastic response at higher strains. As the rotation levels continue to increase, the stress values are continually capped at the tensile strength. These results indicate the possibility of fracture initiation and propagation through the weld, which can lead to an undesirable failure mode.

In spite of the high stresses generated at the end of the welds, the findings show that greater connection performance can be achieved through optimization of the groove weld connection between the beam endplate and HSS column corners. However, the longitudinal weld is an integral part of the connection, which is emphasized by the results from the finite element models that did not include the longitudinal weld (Fig. V.11). For these cases, the elastic stiffness of the connection decreases and the plastic moment capacity of the connection typically is not achieved suggesting that they will not meet IMF and SMF requirements. Further, the majority of deformation occurs in other connection elements beside the beam leading to an undesirable deformation mechanism. Even in the case of the 31.75 mm (1.25 in.) thick endplate, which reaches a normalized moment capacity greater than unity after 0.07 rad., the connection exhibits excessive distortion, particularly in the endplate and collar elements. As a result, omission of the longitudinal weld is not recommended, and further comparisons focus on those models that either include a full-length or half-length longitudinal weld.

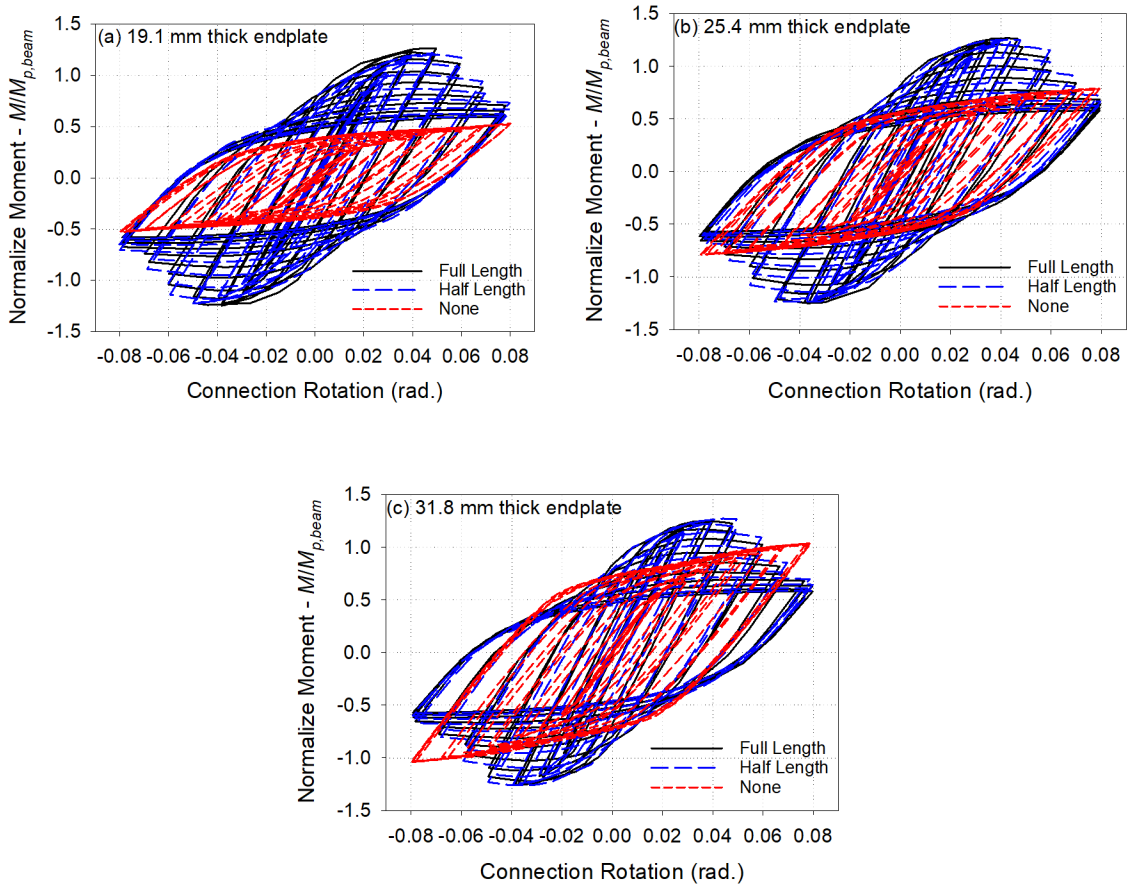

Figure V.10. Hysteretic behavior for the finite element models of the tube-based collar connection with a transverse weld and varying longitudinal weld lengths for beam endplate thicknesses of (a) 19.05 mm (0.75 in.), (b) 25.4 mm (1 in.), and (c) 31.75 mm (1.25 in.).

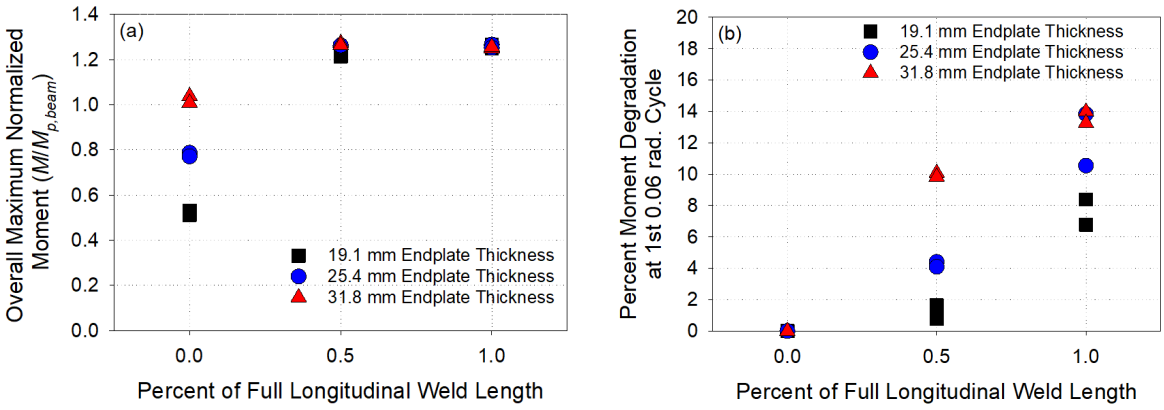

Figure V.11. Influence of the length of the longitudinal groove weld on the (a) overall maximum moment capacity and the (b) moment capacity degradation at 6% drift.

Influence of the transverse fillet weld

The global hysteretic behavior of the connection is not significantly affected by the presence or absence of the transverse weld (Fig. V.12). All of the connections reach a normalized moment capacity higher than 1.2 around the 0.05 rad. cycles and the average percent difference in plastic moment capacity between the connections is 0.6%. At the first 0.04 rad. cycle, the average percent difference in moment capacity between the connections with and without a transverse weld is around 2.1% for an endplate thickness of 19.05 mm (0.75 in.). For the same endplate thickness, at the first 0.06 rad. cycle the connections that have a transverse weld and feature a full or half-length longitudinal weld exhibit 8.4% and 1.6% moment capacity degradation, respectively. Comparing these results to their counterparts without a transverse weld, these exhibit 6.8% and 0.8% degradation, respectively. Similar differences are observed across all rotation levels and endplate thicknesses for cases that feature a full or half-length longitudinal weld. The difference between the connections with and without transverse welds tends to decrease as the endplate thickness increases. This decrease is due to the increased stiffness of the thicker endplates and loads being transferred to the collar in regions closer to the beam-column connection, opposite to the location of the transverse weld. These results suggest the ability to remove this weld in future collar connection designs.

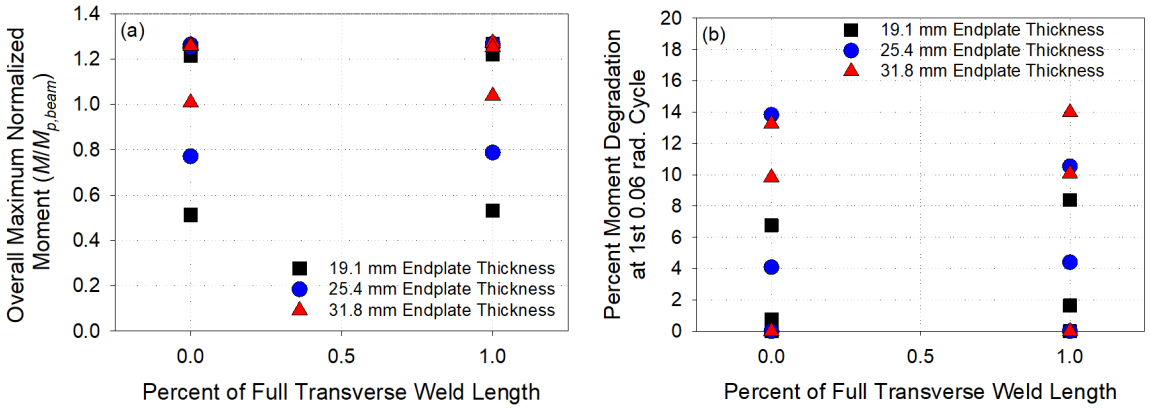

Figure V.12. Influence of the presence of the transverse weld on the (a) overall maximum moment capacity and the (b) moment capacity degradation at 6% drift.

Influence of endplate thickness

For the connections that feature a full-length longitudinal weld, increasing or decreasing the endplate thickness compared to the experimental results shows negligible differences in the overall connection performance (Fig. V.13). As previously discussed, this result is mainly due to elements that make up the connection not being well engaged during loading as a result of most of the load being transferred through the longitudinal weld. The effects of varying the endplate thickness are more noticeable in the connections that feature a half-length longitudinal weld. The stiffness at low rotation levels, when the behavior is predominantly elastic, for the subassemblies that feature a full-length longitudinal weld is higher than the ones with a half-length weld. On average, this difference is around 11.9%, 9.2% and 8.3% for an endplate thickness of 19.05 mm (0.75 in.), 25.4 mm (1 in.), and 31.75 mm (1.25 in.), respectively. This finding shows that increasing the endplate thickness can help compensate for the loss of stiffness due to a shorter length longitudinal weld.

The plastic moment capacity of the connection increases slightly with increasing endplate thickness in cases with a half-length longitudinal weld, about 3.6% when going from a 19.05 mm

(0.75 in.) to a 31.75 mm (1.25 in.) thick endplate. Moment capacity degradation is also influenced by the endplate thickness. As the endplate thickness is increased, the moment degradation in the connection also tends to increase. Overall, the connections that feature a 19.05 mm (0.75 in.) thick endplate exhibit the lowest moment degradation percentages out of all the models, regardless of weld configuration. These results suggest that although employing a thicker endplate can result in an increased maximum moment capacity of the connection, having a thinner endplate is more beneficial when it comes to retaining the strength of the connection when subjected to higher drifts.

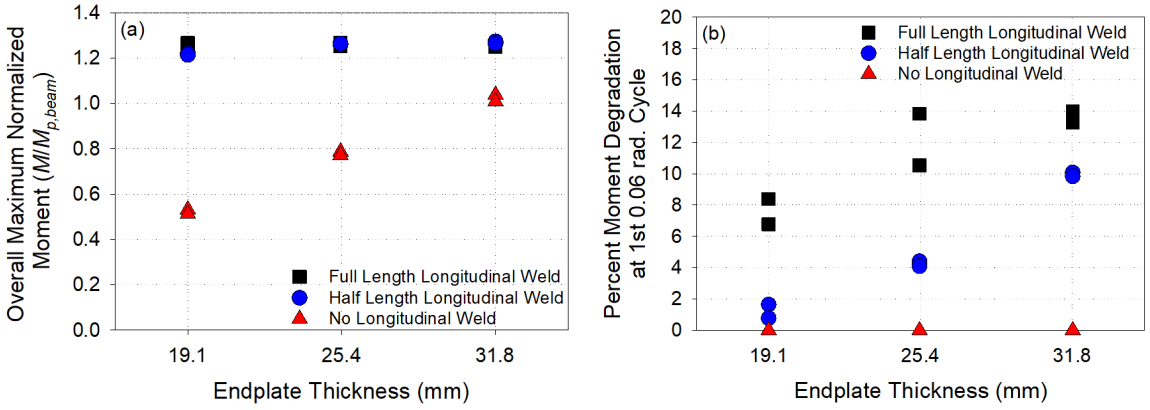

Figure V.13. Influence of the thickness of the beam endplate on the (a) overall maximum moment capacity and the (b) moment capacity degradation at 6% drift.

Conclusions

A finite element model of an advanced HSS-based seismic collar connection is developed to explore potential performance and economy improvements that can increase the practical viability of such a connection. The validated finite element model is then used to conduct a parametric study featuring 18 configurations. The parameters of interest include beam endplate thickness, length of the longitudinal groove weld between the beam endplate and HSS column, and the presence of the transverse fillet weld at the end of the beam endplate between the

endplate and HSS column. The performance of the connection is examined in terms of maximum moment capacity, moment capacity degradation, ability to form a desirable mechanism in which the beam acts as a "fuse," ability to efficiently engage every component of the connection and ability to meet the current SMF ductility requirements. A summary of the findings is presented as follows:

1. The longitudinal groove weld that connects the beam endplate to the HSS column is a necessary weld for the collar connection to develop an appropriate mechanism. Removing this weld results in most of the plastic deformation occurring in the beam endplate, which does not allow the connection to develop a stable plastic hinge in the beam member or reach the beam's maximum moment capacity.
2. All of the models that featured a full-length or half-length longitudinal groove weld did not exhibit any moment capacity degradation during the 4% drift cycles and were able to form a stable plastic hinge in the beam member, away from the column face. The maximum moment capacity of the connection was typically reached during the 5% drift cycles and moment capacity degradation was first observed during the 6% cycles. These results suggest that the HSS-based collar connection is capable of meeting the current ductility requirements to be utilized in the design of SMFs.
3. Reducing the length of the longitudinal groove weld from full to half results in an overall more efficient connection with better cyclic performance, suggesting that less field welding is not only an option, but may also improve the connection's behavior. In the cases that include a full-length longitudinal weld the stress distribution in the model shows that other connection elements such as the collars and beam endplate are minimally engaged in the load resisting process. For this reason, changing the thickness

of the endplate has little to no effect on the overall behavior of the connection when a full-length longitudinal weld is considered. By contrast, the models that feature a half-length longitudinal weld exhibit a more desirable stress distribution where the collars, beam endplate, and panel zone are active load resisting components, resulting in less moment capacity degradation. These improvements come at the expense of increasing the stresses in the longitudinal weld length. While fracture is not considered in the finite element model, this increase in stress needs to be further studied to determine an appropriate weld length.

4. The presence of the transverse weld that connects the end of the beam endplate to the HSS column has minimal effect on the overall behavior of the collar connection, suggesting that further economy and field welding time can be saved by removing it.
5. The thickness of the beam endplate influences the performance of the collar connection in the models that feature a half-length longitudinal groove weld. Increasing the thickness has the effects of increasing the connection's elastic stiffness and maximum moment capacity, while also resulting in a higher moment capacity degradation at large drifts. Considering the three different beam endplate thickness values included in this study, these results suggest that the thinner endplate is better for retaining the strength of the connection during cyclic loading.

CHAPTER VI

Summary and Conclusions

Summary

Recent investigations into the behavior of deep, slender wide flange columns in seismic moment frames have raised concerns regarding their performance when subjected to high axial loads and bending moments. These investigations have identified a previously unrecognized interaction between the local and global failure modes that can result in a deep, slender wide flange column not delivering the expected plastic rotation and axial load capacity. While this behavior calls for more research, it is also worth seeking alternative solutions outside of utilizing wide flange sections. Due to their beneficial properties, hollow structural sections (HSS) can provide an alternative to wide flange sections when trying to improve the seismic behavior of steel moment frames. The empty voids of these sections can be utilized by filling them with energy dissipating materials to limit the occurrence of local buckling and further increase the performance of these sections. Currently, HSS are not commonly used in seismic moment frames due to stringent local slenderness requirements and a lack of a non-proprietary, pre-qualified seismic moment connection between HSS beams and columns. With this in mind, the main goal of this research is to improve the seismic performance of steel moment frames through the assessment of deep, slender wide flange columns and advanced alternatives, focusing on the potential benefits of HSS members and non-traditional materials.

A preliminary computational study of full-scale, deep and slender wide flange cruciform specimens and a subsequent experimental investigation of a half-scale version of these subassemblies is undertaken to study their behavior under combined axial and lateral load while in the presence of other framing elements such as beams and connections (Chapter II). Three identical cruciform subassemblies are experimentally tested with the same axial load level and varying lateral loading protocols which include a symmetric cyclic protocol (progression of fully reversed drifts) and a cyclic ratcheting protocol (collapse-consistent progression of drifts that includes ratcheting behavior). The performance metrics used to assess the behavior of the cruciform subassemblies include moment capacity degradation with continued cycling, column axial shortening, interactions between the local and global instabilities, and ability to meet SMF ductility requirements.

An experimental investigation (Chapter III) and subsequent computational study (Chapter IV) are undertaken to explore the potential benefits to the cyclic performance of HSS beam members by incorporating a polyurethane foam-fill in their voids. Seven pairs of empty and foam-filled sections are tested experimentally under a symmetric cyclic lateral loading protocol to determine the influence of the polyurethane foam-fill across a variety of local slenderness ratios. The data obtained from these tests also serves to calibrate and validate a finite element model of the beams. This model is then used to expand the available dataset by running a parametric study of 52 pairs of empty and foam-filled HSS beams. The urethane foam's ability to mitigate the effects of local buckling is assessed through performance metrics such as maximum moment capacity, moment capacity degradation with continued cycling, and ability to meet the moderate and high ductility criteria. The data obtained from this parametric study is used to develop local slenderness limits for both empty and foam-filled HSS beams based on the

moderate and high ductility performance criteria of maintaining 80% of its maximum moment capacity at 2% and 4% drift, respectively (AISC 2016a).

The final portion of this study is a computational investigation with the goal of improving the efficiency of an innovative HSS-based collar connection. A finite element model of the connection is calibrated and validated using data from previous experimental tests. This model is utilized to conduct a parametric study where different weld configurations and beam endplate thicknesses are used for the collar connection. This parametric study provides insight into the load path in the connection and how it changes with varying weld configurations. The results from this parametric study are used to determine if further economy can be saved in the design and construction of the HSS-based collar connection, while still meeting the high ductility requirements.

Major Findings

- Experimental testing of half-scale wide flange cruciform specimens shows that changing the lateral loading protocol has a dramatic effect on the behavior of the subassemblies, mainly pertaining to the performance of the column section. The cyclic ratcheting (CR) loading protocol results in a significantly less demanding protocol when compared to the symmetric cyclic (SC) protocol which consists of a progression of fully reversed drifts. The CR progression only puts one of the column flanges in compression, limiting the degree of local buckling. This difference in behavior is seen by comparing the cyclic performance of the experimentally tested specimens W2 and W3. Specimen W2 was tested under the SC protocol and was not able to meet the high ductility performance requirements. By contrast, specimen W3 was subjected to the CR protocol and was comfortably able to meet the high ductility criteria. These results suggest that while

employing the SC protocol can be a conservative approach, it is important to also consider other loading protocols which may not be as overly demanding and result in exaggerated poor behavior. The computational study of the full-scale subassemblies also found similar results.

- The buckling behavior observed in the experimentally tested cruciform specimens show signs of an interaction between the global and local instabilities in the column. Every subassembly developed local buckling in the column web and flanges near the base. The presence of local buckling facilitates the onset of global buckling. Once global buckling also occurs, this increases the degree of flange local buckling towards the direction that the global buckling shape takes. With the current design standards, the propensity for global and local instabilities is evaluated separately according to a column's geometric ratios. The results of this experimental study suggests there is a need to consider how the local and global instabilities interact with each other as these interactions have the potential to significantly affect the expected seismic performance of a column section.
- Experimental testing of seven pairs of empty and foam-filled HSS beams shows that incorporating a polyurethane foam in the voids of HSS is a feasible approach to improving the cyclic performance of these sections. The urethane foam-fill manages to delay the onset of local buckling in all but one of the tested beams and in every case reduces the extent of deformation in the plastic hinge region. An overall reduction in moment capacity degradation with continued cycling is observed that generally delays, and in some cases prevents, the onset of fracture.
- The effectiveness of the urethane foam-fill in mitigating the effects of local buckling varies depending on the local slenderness ratios of each section. Beam sections that meet

the highly ductile criteria can potentially benefit from the foam-fill if they still experience some amount of local buckling at larger rotation cycles. The moderately ductile sections experience less moment capacity degradation and delayed fracture initiation as a result of the presence of the foam. As an example of the sections that do not meet the moderately ductile local slenderness criteria, the HSS 254×203.2×6.4 (HSS 10×8×1/4) beam (section with the highest local slenderness ratios that was experimentally tested) did not experience a delay in fracture initiation even though capacity degradation was significantly reduced at earlier cycles. These results suggest that there are limits to how large the local slenderness ratios can be for the urethane foam to be effective.

- The current AISC ductility limits for empty HSS beams, while conservative, are not capable of accurately predicting the cyclic performance of HSS beams. This finding is partly due to the fact that the current limits do not consider the effect of the section's *h/t* ratio on its ability to meet the ductility requirements for IMFs and SMFs. Results from a computational study of 52 empty HSS beams suggest that both the *b/t* and *h/t* ratios should be considered when determining local slenderness limits for the various ductility ratings. It is worth noting that the data also suggests that while both the *b/t* and *h/t* ratios influence the behavior of the beams, the *h/t* ratio has a larger effect on the section's moment capacity degradation under increasing cyclic rotations.
- Based on both the experimental and computational studies, the addition of the urethane foam-fill can significantly improve the cyclic behavior of an HSS beam, enough to change its ductility rating in certain instances. In the case of the experimental study, three of the empty beam sections meet the moderately ductile *b/t* limit. With the addition of the urethane foam-fill these sections are able to meet the highly ductile performance

requirement of maintaining at least 80% of its maximum moment capacity out to a 4% drift cycle. In the case of the computational study (which included 52 pairs of HSS), the ductility ratings of the empty HSS beams based on their cyclic performance include 27 sections that meet the high ductility requirements, 22 that meet the moderate ductility requirements, and 3 that do not meet the moderate ductility criterium. When the urethane foam-fill is added, these numbers change to 39, 12, and 1, respectively. These results suggest that incorporating a urethane foam-fill is a feasible approach to increase the number of HSS that can be used in IMFs and SMFs.

- Computational studies of an advanced HSS-based collar connection show that while it is a viable seismic moment connection, there are many changes that can be made to improve its economy, ease of construction, and overall performance. The amount of field welding required can be reduced significantly by eliminating certain welds that have minimal effect on the overall behavior of the connection. The length of other necessary welds can also be reduced without negatively affecting the connection's performance. In addition to making changes to the welds, the thickness of the beam endplate can also be modified to improve the moment capacity retention of the connection during cyclic rotations.

Recommendations for Future Research

Further investigations are suggested to expand on the conclusions developed in this dissertation. The recommendations for future research are the following:

- Given that this study only conducted three experimental tests on deep, slender wide flange column subassemblies, a larger body of data is needed to establish limitations on the local and global slenderness ratios to ensure adequate ductility is obtained. It is

suggested that the slenderness requirements consider the interaction between the local and global instabilities that is observed in the experimental tests. Further comparison of subassembly tests with member level tests are also needed.

- The preliminary finite element study of the cruciform subassemblies showed that an HSS column can potentially perform better than a comparable wide flange section under combined axial and lateral load. Similar experimental subassembly tests as with the wide flange columns should be conducted, but with an HSS column section to explore the potential benefits of incorporating these sections in a seismic moment frame.
- The polyurethane foam material used in this study to fill the voids of HSS beams was shown to be effective in mitigating the effects of local buckling and improving cyclic performance. Regardless, the material characterization of this foam showed a great deal of variability in its mechanical properties depending on how the compounds that make the foam were mixed. It is suggested that a study be conducted to determine a standardized mixing procedure to ensure adequate mechanical properties are obtained from the urethane foam.
- While this dissertation focused on the polyurethane foam material as a means to improve the cyclic performance of HSS beams, it is suggested that other types of materials with different mechanical properties be investigated. Given the potential differences in mechanical properties, this study could lead to finding multiple feasible fill materials at different price ranges and different levels of effectiveness depending on the type of loads that the structural members are expected to experience.
- While some progress has been made in this dissertation regarding improving the economy and efficiency of the tube-based collar connection, further optimizations can be

made to its design. Further research is needed into the connection's welds to determine an optimal weld configuration that balances adequate seismic performance with cost and ease of construction.

BIBLIOGRAPHY

AISC. 2005. *Seismic Provisions for Structural Steel Buildings*, ANSI/AISC 341-05. Chicago, Illinois: AISC.

AISC. 2016a. *Seismic Provisions for Structural Steel Buildings*, ANSI/AISC 341-16. Chicago, Illinois: AISC.

AISC. 2016b. *Prequalified Connections for Special and Intermediate Steel Moment Frames for Seismic Applications*, ANSI/AISC 358-16. Chicago, Illinois: AISC.

Ammons, M., Shimada, H., McCormick, J., Kurata, M. 2021. "Experimental Investigation of Foam-Filled CHS Braces under Cyclic Loading." *J. Struct. Eng.* 147(5), 04021044. https://doi.org/10.1061/(ASCE)ST.1943-541X.0002993

Arasaratnam, P., Sivakumaran, K.S., Tait, M.J. 2011. "True Stress-True Strain Models for Structural Steel Elements." *ISRN Civ. Eng.* 2011, 656401. https://doi.org/10.5402/2011/656401

ASCE. 2005. *Minimum Design Loads for Buildings and Other Structures*, ASCE/SEI 7-05. Reston, Virginia.

ASTM International. 2018. *ASTM A500/A500M-18 Standard Specification for Cold-Formed Welded and Seamless Carbon Steel Structural Tubing in Rounds and Shapes*, ASTM International. West Conshohocken, Pennsylvania.

AWS. 2010. *Structural Welding Code–Steel*, AWS D1.1/D1/1M. Miami, Florida: AWS.

Chi, B., Uang, C-M. 2002. "Cyclic Response and Design Recommendations of Reduced Beam Section Moment Connections with Deep Columns." *J. Struct. Eng.* 128 (4), 464-473. https://doi.org/10.1061/(ASCE)0733-9445(2002)128:4(464)

El Jisr, H., Elkady, A., Lignos, D.G. 2020. "Hysteretic Behavior of Moment-Resisting Frames Considering Slab Restraint and Framing Action." *J. Struct. Eng.* 146(8), 04020145. https://doi.org/10.1061/(ASCE)ST.1943-541X.0002696

Elchalakani, M., Zhao, X.L., Grzebieta, R.H. 2001. "Concrete-filled circular steel tubes subjected to pure bending." *J. Constr. Steel Res.* 57 (11), 1141-1168. https://doi.org/10.1016/S0143-974X(01)00035-9

Elkady, A., Lignos, D. 2015. "Analytical investigation of the cyclic behavior and plastic hinge formation in deep wide-flange steel beam-columns." In *Proc., Bull Earthquake Eng.,* 13, 1097-1118. https://doi.org/10.1007/s10518-014-9640-y

Elkady, A., Lignos, D. 2016. "Dynamic Stability of Deep and Slender Wide-Flange Steel Columns – Full Scale Experiments." In *Proc., Annual Stability Conference,* Orlando, Florida. https://tinyurl.com/menhcuvc

Elkady, A., Lignos, D.G. 2018. "Full-Scale Testing of Deep Wide-Flange Steel Columns under Multiaxis Cyclic Loading: Loading Sequence, Boundary Effects, and Lateral Stability Bracing Force Demands." *J. Struct. Eng.* 144(2), 04017189. https://doi.org/10.1061/(ASCE)ST.1943-541X.0001937

Fadden, M., McCormick, J. 2012. "Cyclic Quasi-Static Testing of Hollow Structural Section Beam Members." *J. Struct. Eng.* 138 (5), 561-570. https://doi.org/10.1061/(ASCE)ST.1943-541X.0000506

Fadden, M., McCormick, J. 2014a. "Finite element model of the cyclic bending behavior of hollow structural sections." *J. Constr. Steel Res.* 94, 64-75. https://doi.org/10.1016/j.jcsr.2013.10.021

Fadden, M., McCormick, J. 2014b. "HSS-to-HSS seismic moment connection performance and design." *J. Constr. Steel Res.* 101, 373-384. https://doi.org/10.1016/j.jcsr.2014.05.022

Fadden, M., Wei D., McCormick J. 2015. "Cyclic Testing of Welded HSS-to-HSS Moment Connections for Seismic Applications." *J. Struct. Eng.* 141 (2), 04014109. https://doi.org/10.1061/(ASCE)ST.1943-541X.0001049

Fadden, M.F. 2013. "Cyclic Bending Behavior of Hollow Structural Sections and their Application in Seismic Moment Frame Systems." Ph.D. dissertation, Ann Arbor, MI: University of Michigan. https://hdl.handle.net/2027.42/97864

FEMA. 2000. *Recommended Seismic Design Criteria for New Steel Moment-Frame Buildings,* FEMA-350. Washington, DC. https://tinyurl.com/zpyzy96j

Fisher, J.M., Kloiber, L.A. 2006. "Design Guide 1: Base Plate and Anchor Rod Design (Second Edition)." AISC. Chicago, Illinois: AISC.

Flores Carreras, C., Alfaro, L., Wei, D., McCormick, J. 2018. "Improvement of the Cyclic Bending Behavior of HSS Members through Foam Fill." In *Proc., Eleventh U.S. National Conference on Earthquake Engineering*, Los Angeles, California. https://tinyurl.com/m2x26aht

Flores Carreras, C., Sediek, O., McCormick, J., El-Tawil, S. 2020. "Evaluation of the Performance of Deep, Slender Columns through the use of Sub-Assemblies." In *Proc., 17th World Conference on Earthquake Engineering*, Sendai, Japan. https://tinyurl.com/4ub8uj9u

Flores Carreras, C.A., McCormick, J.P. 2019. "Relaxing Current Ductility Requirements in Tube-Based Seismic Moment Frames." In *Proc., 17th International Symposium on Tubular Structures*, Singapore. https://tinyurl.com/49k8pbpy

Fogarty, J., El-Tawil, S. 2016. "Collapse Resistance of Steel Columns under Combined Axial and Lateral Loading." *J. Struct. Eng.* 142 (1), 04015091. https://doi.org/10.1061/(ASCE)ST.1943-541X.0001350

Hajjar, J.F. 2000. "Concrete-filled steel tube columns under earthquake loads." *Prog. Struct. Eng. Mater.* 2 (1), 72-81. https://doi.org/10.1002/(SICI)1528-2716(200001/03)2:1%3C72::AID-PSE9%3E3.0.CO;2-E

Jubb, J.E.M., Redwood, R.G. 1966. "Design of Joints to Box Sections." *The Institution of Structural Engineers*, Conference on Industrialized Building and the Structural Engineer. Institute of Structural Engineers, London.

Kamba, T., Tabuchi, M. 1995. "Database for tubular column to beam connections in moment resisting frames." International Institute of Welding Commissions XV, IIW Doc. XV-893-95.

Kircher, C., Deierlein, G., Hooper, J., Krawinkler, H., Mahin, S., Shing, B., Wallace, J. 2010. *Evaluation of the FEMA P-695 Methodology for Quantification of Building Seismic Performance Factors*, Grant/Contract Reports (NISTGCR), National Institute of Standards and Technology, Gaithersburg, MD. https://tinyurl.com/3xnuy6rh

Korol, R.M., El-Zanaty, M., Brady, F.J. 1977. "Unequal width connections of square hollow sections in Vierendeel trusses." *Can. J. Civ. Eng*. 4, 190. https://doi.org/10.1139/l77-024

Kurobane, Y., Packer, J.A., Wardenier, J., Yeomans, N. 2004. "Design guide for structural hollow section column connections." CIDECT series "Construction with Hollow Steel Sections" No. 9, TÜV-Verlag, Köln, Germany.

Lai, Z., Varma, A.H. 2015. "Noncompact and slender circular CFT members: Experimental database, analysis, and design." *J. Constr. Steel Res.* 106, 220–233. https://doi.org/10.1016/j.jcsr.2014.11.005

Lai, Z., Varma, A.H., Zhang, K. 2014. "Noncompact and slender rectangular CDT members: Experimental database, analysis, and design." *J. Constr. Steel Res.* 101, 455–468. https://doi.org/10.1016/j.jcsr.2014.06.004

Lu, Y.Q., Kennedy, D.J.L. 1994. "The flexural behaviour of concrete-filled hollow structural sections." *Can. J. Civ. Eng.* 21, 111–130. https://doi.org/10.1139/l94-011

Maximov, J.T., Duncheva, G.V., Kuzmanov, T.V. 2008. "Modelling of hardening behaviour of cold expanded holes in medium-carbon steel." *J. Constr. Steel Res.* 64, 261-267. https://doi.org/10.1016/j.jcsr.2007.07.005

Nakashima, M., Inoue, K., Tada, M. 1998. "Classification of damage to steel buildings observed in the 1995 Hyogoken-Nanbu earthquake." *Engineering Structures*, 20(4-6), 271-281. https://doi.org/10.1016/S0141-0296(97)00019-9

Prion, H.G.L., Boehme, J. 1994. "Beam-column behaviour of steel tubes filled with high strength concrete." *Can. J. Civ. Eng.* 21, 207–218. https://doi.org/10.1139/l94-024

SAC Steel Project. 2000. "Loading Histories for Seismic Performance Testing of SMRF Components and Assemblies*." Report No. SAC/BD-00/10*.

Sediek, O.A., Wu, T-Y, McCormick, J., El-Tawil, S. 2020. "Collapse Behavior of Hollow Structural Section Columns under Combined Axial and Lateral Loading." *J. Struct. Eng.* 146(6), 04020094. https://doi.org/10.1061/(ASCE)ST.1943-541X.0002637

Sedlacek, G., Dahl, W., Stranghöner, N., Kalinowski, B., Rondal, J. and Boreaeve, Ph. 1998. "Investigation of rotation behavior of hollow section beams." EUR 17994 EN. https://tinyurl.com/5c54euzu

Simulia. 2017. Abaqus/CAE. Dassault Systèmes Simulia Corporation. Johnston, RI, USA.

Uang, C-M, Bruneau, M. 2018. "State-of-the-Art Review on Seismic Design of Steel Structures." *J. Struct. Eng.* 144 (4), 03118002. https://doi.org/10.1061/(ASCE)ST.1943-541X.0001973

Uang, C-M, Ozkula, G., Harris, J. 2015. "Observations from Cyclic Tests on Deep, Slender Wide-Flange Structural Steel Beam-Column Members." In *Proc., Annual Stability Conference*, Nashville, Tennessee. https://tinyurl.com/yf9jcnmh

U.S. Composites, Inc. http://www.uscomposites.com/foam.html

Vulcu, C., Stratan, A., Ciutina, A., Dubina, D. 2017a. "Beam-to-CFT High-Strength Joints with External Diaphragm. I: Design and Experimental Validation." *J. Struct. Eng.* 143(5), 04017001. http://dx.doi.org/10.1061/(ASCE)ST.1943-541X.0001709

Vulcu, C., Stratan, A., Ciutina, A., Dubina, D. 2017b. "Beam-to-CFT High-Strength Joints with External Diaphragm. II: Numerical Simulation of Joint Behavior." *J. Struct. Eng.* 143(5), 04017002. http://dx.doi.org/10.1061/(ASCE)ST.1943-541X.0001693

Wei, D. 2017. "Enhancement of Steel Moment Connections Through Non-Traditional Sections and Materials." Ph.D. dissertation, Ann Arbor, MI: University of Michigan. https://hdl.handle.net/2027.42/137135

Wei, D., Flores Carreras, C.F., McCormick, J.P. 2016. "Improving the Seismic Response of Hollow Structural Sections Using Polymer Foam Fill." In *Proc., 2nd Huixian Int. Forum on Earthquake Engineering for Young Researchers,* Beijing, China. https://tinyurl.com/wpycdzyh

Wei, D., McCormick, J. 2017. “Experimental testing of tube-based seismic collar connections under cyclic loads.” In *Proc., 16th International Symposium for Tubular Structures*, Melbourne, Australia. https://doi.org/10.1201/9781351210843
Wu, T-Y, El-Tawil, S., McCormick, J. 2018a. “Highly Ductile Limits for Deep Steel Columns.” *J. Struct. Eng.* 144 (4), 04018016. https://doi.org/10.1061/(ASCE)ST.1943-541X.0002002

Wu, T-Y, El-Tawil, S., McCormick, J. 2018b. “Seismic Collapse Response of Steel Moment Frames with Deep Columns.” *J. Struct. Eng.* 144 (9), 04018145. https://doi.org/10.1061/(ASCE)ST.1943-541X.0002150

Zargar, S., Medina, R. A., Miranda, E. 2014. “Cyclic Behavior of Deep Steel Columns Subjected to Large Drifts, Rotations, and Axial Loads.” In *Proc., Tenth U.S. National Conference on Earthquake Engineering,* Anchorage, Alaska. https://tinyurl.com/yr4ftrad

Zhou, P., Beeh, E., Kriescher, M., Friedrich, H.E., Kopp, G. 2016. “Experimental comparison of energy absorption characteristics of polyurethane foam-filled magnesium and steel beams in bending.” *Int. J. Impact Eng.* 96, 76–87. https://doi.org/10.1016/j.ijimpeng.2016.02.006